Study on Quantitative Microstructure Analysis by Mathematical Morphology

Study on Quantitative Microstructure Analysis by Mathematical Morphology

数学的形態学手法による定量的ミクロ組織解析に関する研究

徐岩

東北大学工学研究科

平成三十年

Contents

Chapter 1 Introduction

1.1 Background

1.1.1 History of material microstructure analysis

The progress of material science is the basis of progress of human civilization and the material microstructure analysis has been a concerned subject ever since the first usage of optical microscope to metal materials. P. P. Anosove[1] was reported to be the first scientist who applied microscope to study the metal microstructure in 1841. He observed the microstructure of the ancient knives and found that the microstructure in the knives was similar to that of steel. A typical steel microstructure is shown in Fig. 1.1. Afterwards, the microscopic method was widely used to investigate material microstructure in other fields[2, 3]. The correlation between 2 dimensional optical images and 3 dimensional microstructures has been paid attention[4-6]. R. T. Dehoff[7] et al. reported the quantitative microscopy of materials according to the microscopic images achieved by optical microscopes. Material microstructure parameters such as volume fraction, grain size and grain shape are discussed with geometrical probability[8, 9] .

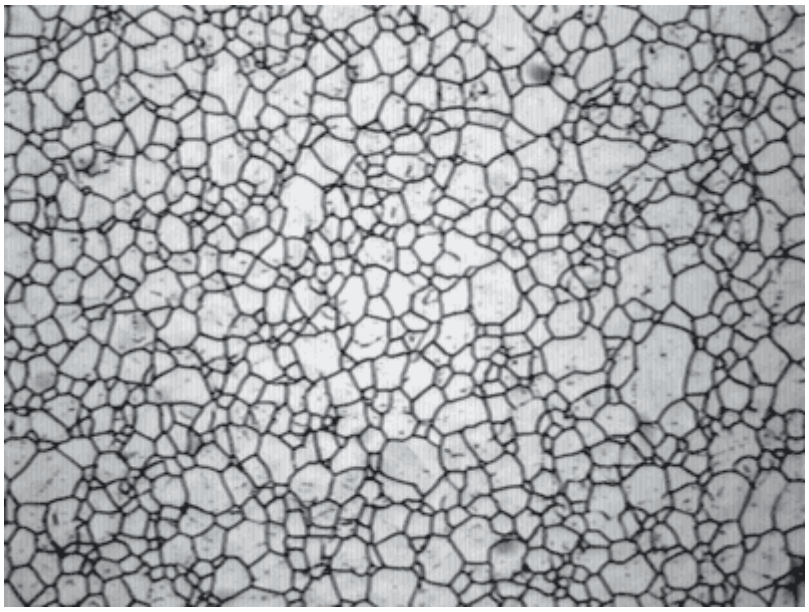

Fig. 1.1 Optical microscopic image of steel[10].

In the recent years, the microstructure analysis method ushered significant progress with the fast development of microscope. Electron back scatter diffraction (EBSD)[11] is a microstructural-crystallographic characterization technique to study crystalline or polycrystalline material. This technique involves the understanding the structure, crystal orientation and phase of materials. Scanning electron microscope(SEM)[12] is a microscope which can achieve the surface topology of a material. In contrast to the 2 dimensional image obtained in the observation using optical microscope, the image obtained with SEM method is a 3 dimensional image. In addition, the resolution of SEM is much finer than that of the optical microscopes. Atomic force microscope (AFM)[13], transmission electron microscope (TEM)[14], scanning tunnel microscope (STM)[15] are also the new techniques to obtain better images than the optical microscope.

Although the microstructure observing techniques have been dramatically improved,

the optical microscopy still plays an essential role in material microstructure analysis. This is because of the convenience, low time cost and low equipment cost of optical microscopy[16]. It is important for the practical industries.

1.1.2 Material microstructure analysis and material property prediction

Material microstructure always has significant influence on the properties. Usually, people pursue desired performance of a material by altering its microstructure. For instance, heterogeneous nucleating agent is mixed into the liquid aluminum alloys to promote the nucleation during the solidification process and thus achieve fine microstructure. Such kind of material is expected to outcome better mechanical performances. It has long been an issue to obtain information from material microstructure so that people can make an evaluation on the subsequent performance of the material.

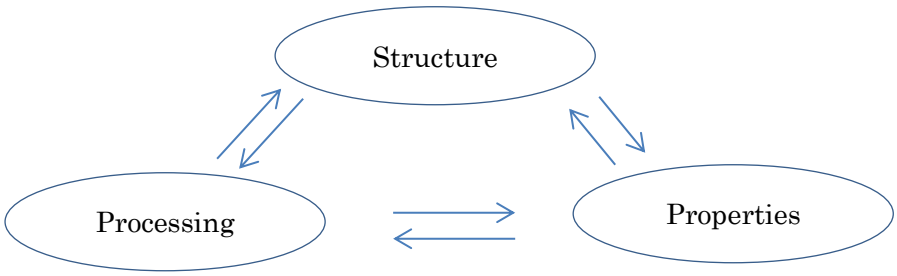

Fig. 1.2 The material science paradigm illustrating the relationship among material structure, processing and properties.

As is illustrated in Fig.1.2, structure determines material properties and the processing can alter the material structures. In material science, there is a hierarchy of structures, such as nuclear structure, atomic structure, molecular structure, crystal

structure, electronic structure, defect structure, microstructure, macrostructure, etc. They each have dramatic correlation to the nuclear properties, chemical properties, electrical and electromagnetic properties, mechanical properties, etc[17]. Microstructure has the correlation to almost all of the properties[18]. Among all the structures, evaluation of microstructure is one of the most key methods to evaluate the possible performances of a material[7, 8].

People sought to evaluate the mechanical performance of a component by analyzing its microstructure. According to the Hall-Petch[19, 20] relation shown in Eq.1.1, the yield stress for a polycrystalline metal material is proportional to its grain size in microstructure[17]. For decades, people have carried out massive research on the appropriate evaluation of material microstructure.

$$\sigma_y = \sigma_0 + kd^{-1/2} \tag{1.1}$$

According to the percolation theory[21], the electrical conductivity of a compound correlated with the volume fraction of the conductive particles in the compound[22-24]. Eq. 1.2 shows the correlation, where ϕ_c is the conductivity of the compound, ϕ_0 is the conductivity of the pure conductive material, p is the volume fraction, p_c is the critical percolation fraction and t is a parameter correlating to material. p_c correlated to the particle aspect ratio[25]. Large particle aspect ratio tells small p_c.

$$\phi_C = \phi_0 \left(p - p_c \right)^t \tag{1.2}$$

In a bi-phase material, such as Al-Si alloys, the mechanical properties have

significant correlation to the dendrite cell size[26]. Carlos H. Cáceres[27] et al. reported that the elongation to fracture of A356-T62 alloy negatively correlated to the dendrite cell size. Fig. 1.3 shows the correlation between the ductility of Al-Si alloy and dendrite cell size.

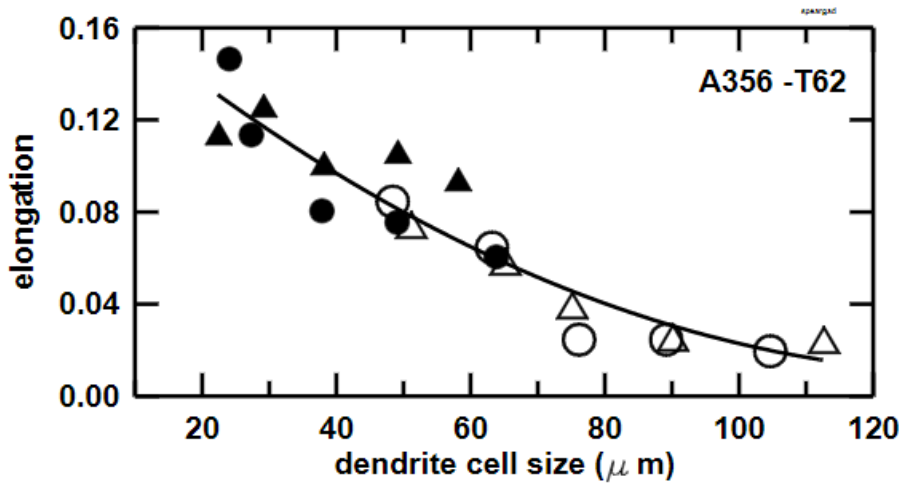

Figure 1.3 Elongation to fracture as a function of the dendrite cell size for alloy A356 (after Spear and Gardner[26]). The different symbols represent different heats in the original data.

1.1.3 Conventional material microstructure analysis methods

Conventional material microstructure analysis involves of volume fraction, grain size, grain shape and grain orientation analysis[7].

1.1.3.1 Manual measurement

Volume fraction is the key parameter to characterize how much percentage of volume the concerned phase takes up in the material. The exact volume fraction should be

evaluated from the 3 dimensional structures. However, it is difficult to achieve the 3 dimensional microstructure of a material. Usually, the volume fraction can be evaluated from area fraction, line intercept fraction or point possibility from a 2-dimensional optical image[7]. For a binary-phase material shown in Fig. 1.4, the volume fraction of α phase (blue pixels) $V_\alpha/V_{\alpha+\beta}$ can be estimated with area fraction $S_\alpha/S_{\alpha+\beta}$. It is depicted in Eq. 1.3, where V is the volume, S is the area and $S_\alpha = S_{\alpha1} + S_{\alpha2} + S_{\alpha3} + S_{\alpha4}$.

$$\frac{V_\alpha}{V_{\alpha+\beta}} = \frac{S_\alpha}{S_{\alpha+\beta}} \tag{1.3}$$

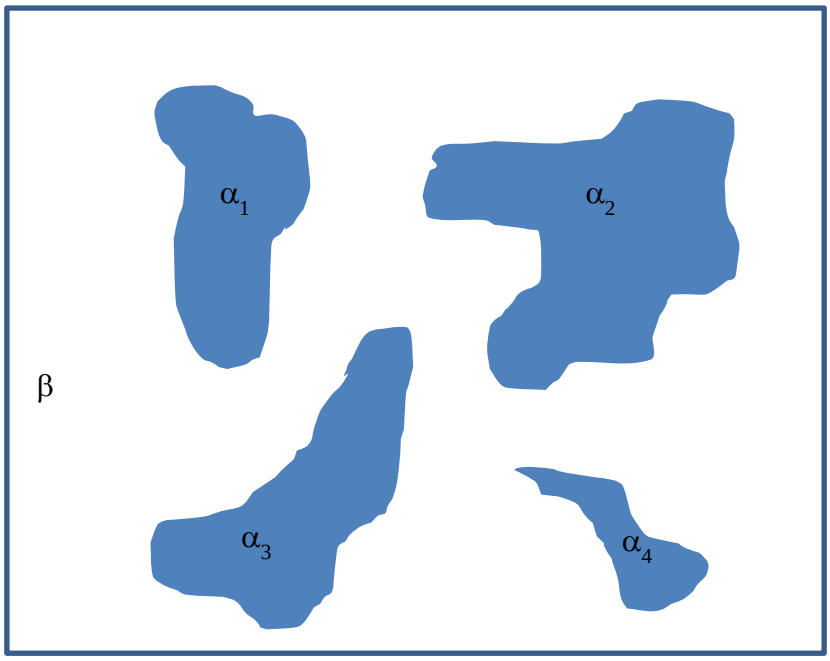

Fig. 1.4 Schematic for the microstructure of a binary-phase material. Blue phase is the concerned phase.

The manual measurement of a grain could be done with digitizing tablet method on an optical image. The number of grid every grain takes up will be counted and be used

to calculate the grain area. Fig. 1.5 illustrates the methodology of grain size measuring with digitizing tablet.

The procedure of grain size measuring with digitizing tablet is tedious and labor-intensive[28]. Many assistive software of microscope provide fit polygon method to approximate the grain area, as shown in Fig. 1.6. In comparison with digitizing tablet method, the fit polygon method reduced the labor-intensity. However, it still calls for high workload.

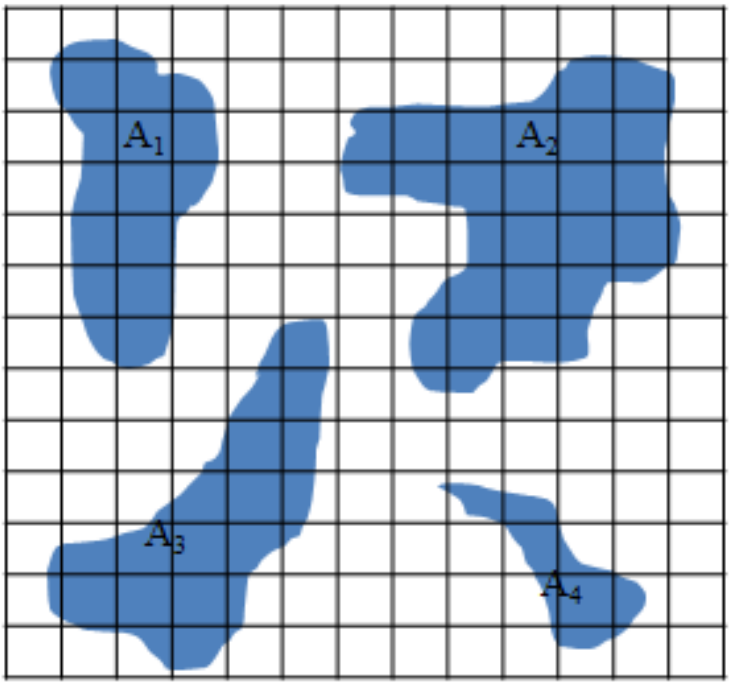

Fig. 1.5 Digitizing tablet to measure grain area.

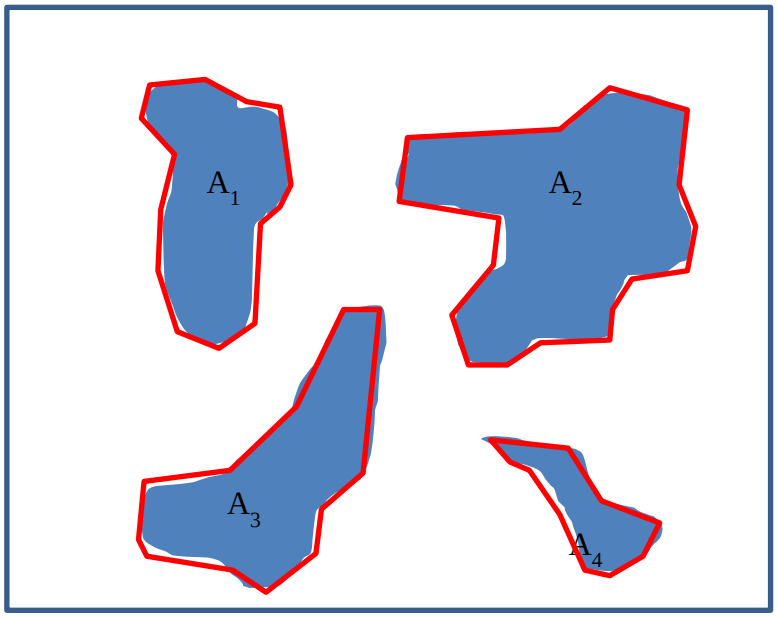

Fig. 1.6 Illustration of fit polygon method to approximate grain size.

The grain size means the area of a grain[28]. Usually, we use the equivalent diameter[29] instead of grain area to characterize grain size in a microstructure. Eq. 1.4 shows how to calculate grain size from grain area, where $d_{equivalent}$ is the equivalent diameter and A is the grain area. As is illustrated in Fig. 1.7, the equivalent diameter is the diameter of a circle with same area to the grain.

$$d_{equivalent} = 2\sqrt{\frac{A}{\pi}} \tag{1.4}$$

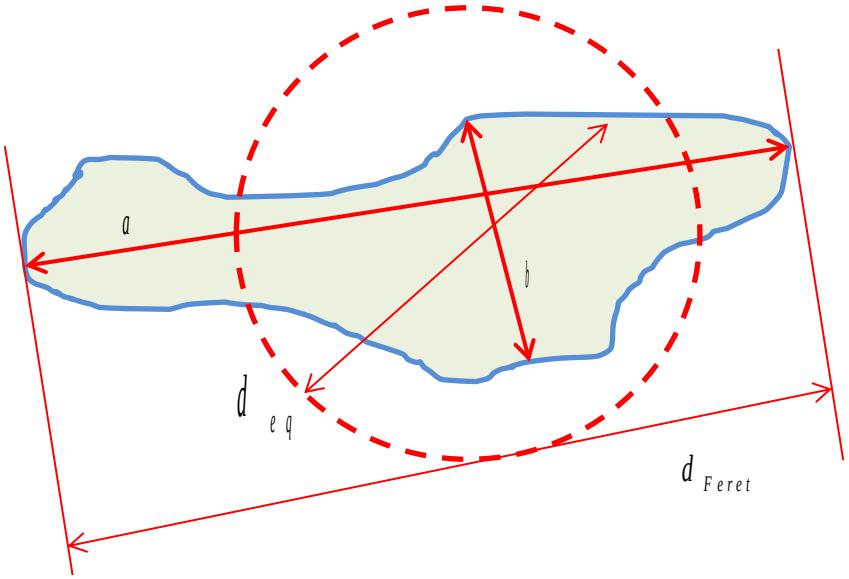

Fig. 1.7 Schematic of parameters characterizing grain size.

Another parameter is Feret diameter[30]. In general, it can be defined as the distance between the two parallel planes restricting the grain perpendicular to a certain direction. An example of Feret diameter has been shown in Fig. 1.7.

Grain or particle shape is essential for evaluating potential performance of a material. Granular morphology in a steel material usually promises better performance than those non-granular ones. In contrast, a ceramic-matrixed compound with long-striped metal particles usually has better electrical conductivity than those with round-like particles. Aspect ratio[31] and shape factor are the two commonly used parameters to characterize particle shape.

Eq. 1.5 shows the equation to calculate aspect ratio. Here, a is the major axis length and b is the minor axis length. a and b are illustrated in Fig. 1.7. Aspect ratio is a parameter to characterize particle elongation rate of particle shape.

$$AR = \frac{a}{b} \tag{1.5}$$

Aspect ratio cannot reflect the shape complexity of a particle. Usually, shape factor is used to do so. It is depicted by Eq. 1.6, where P and A are the perimeter and area of a grain, respectively.

$$f = \sqrt{\frac{P^2}{4\pi A}} \tag{1.6}$$

1.1.3.2 Image processing method

Image processing[7] method is used to improve the efficiency of microstructure evaluation. Fig. 1.7 shows a typical procedure in image processing[32] method. The object in image processing is optical image obtained from samples with optical microscope. In the image pre-processing stage, the image will be processed to eliminate noise or make binary image. Then, the grains will be segmented in the image segmentation procedure. Individual grains will be extracted and the boundaries that cannot be seen on the original image will be re-constructed. Finally, the desired data can be achieved from the segmentation result.

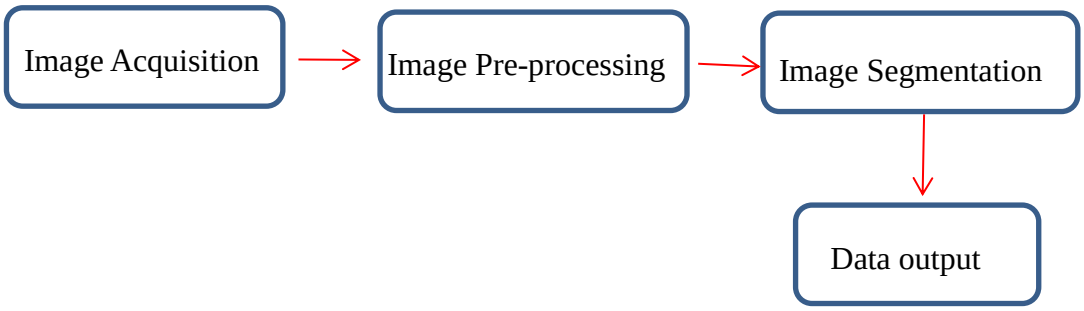

Fig. 1.7 Typical procedures in image processing method.

In the early stage, Image pre-processing and segmentation stages were conducted at the same time. J. Prewitt[33] et al. used binarization method[34] to segment cells from the

neighboring environment. Usually, the two phases has different grayscale values. Fig. 1.8 shows the result of cell segmentation with binarization method. It can be seen that the cells are black pixels and the fluid around them is white. The problem of binarization method is that the congregated grains could not be segmented.

R. T. Dehoff[7] applied clustering analysis[35] to segment congregated grains after binarization. However, the clustering analysis method calls for large computation resources. Fig. 1.9 shows the result of clustering analysis by R. T. Dehoff.

Another grain segmentation method is edge detection[36]. Fig. 1.10 shows an application example of Canny edge detection algorithm on spinal image. Obviously, the edges of different regions have been detected. The problem of this method is that it cannot detect edges for those congregated regions.

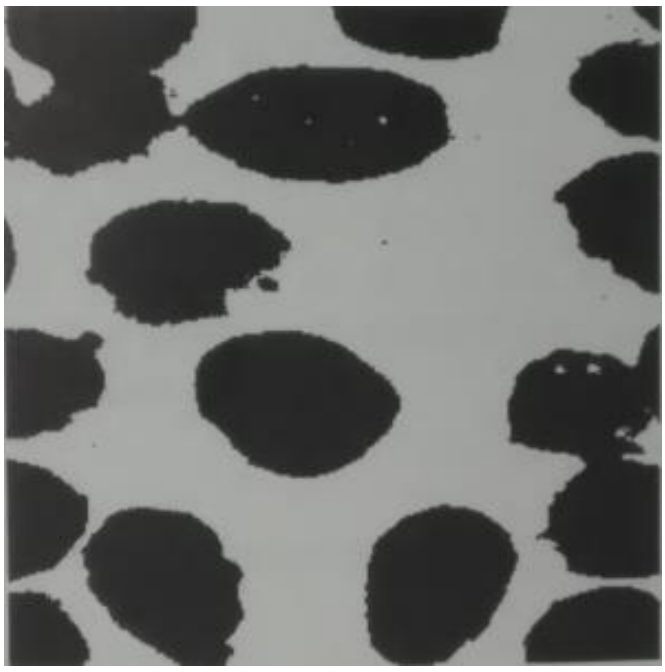

Fig. 1.8 Cell segmentation using binarization method[7, 33].

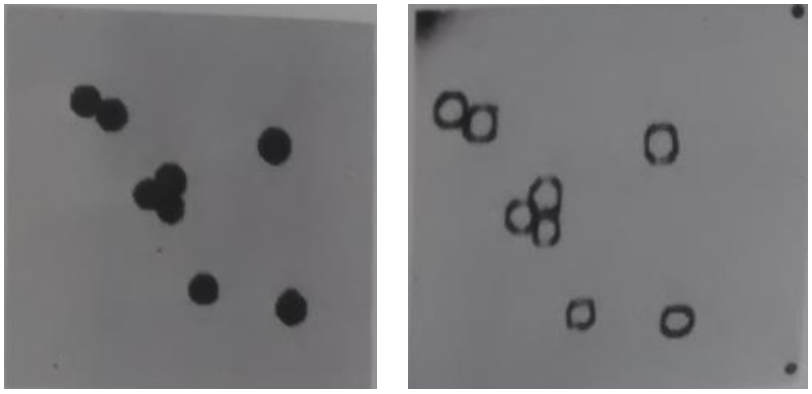

(a) (b)

Fig. 1.9 Grain segmentation with clustering method[7]. a) original and b) segmented image.

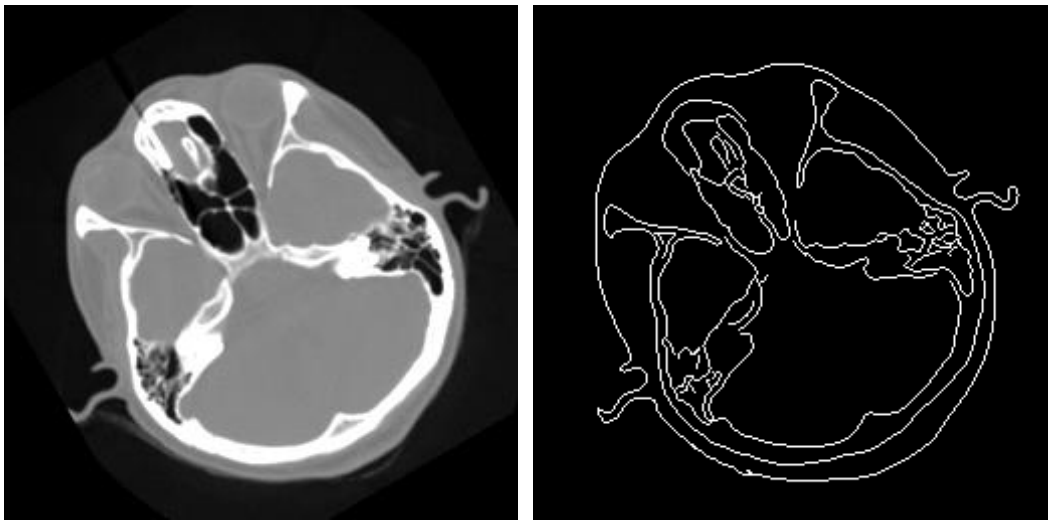

(a) (b)

Fig. 1.10 Image segmentation with edge detection method[36].

1.2 Mathematical morphology

1.2.1 History of mathematical morphology

Mathematical morphology was firstly proposed by J. Serra and G. Matheron[37] in 1960s when they were dealing with research in mining. Porous media are binary in the sense that a point of a porous medium either belongs to a pore or to the matrix surrounding the pores. This led them to introduce a set formalism for analyzing binary images. Mathematical morphology can be defined as a theory for the analysis of spatial structures. It is called morphology because it aims at analyzing the shape and form of the objects. It is mathematical in the sense that the analysis is based on set theory, integral geometry and lattice algebra. Fig. 1.11 illustrates the cross-fertilization between applications, methodologies, theories and algorithms. Mathematical morphology has a wide application in science and engineering. Based on the applications, certain algorithms have been developed to solve the problems. The advance of the algorithms richened the methods and theories in mathematical morphology. Finally, the detailed methods and theory helped to solve different problems in actual applications.

In the early stage of mathematical morphology, the algorithms mainly involved of binary signal processing. In the following decades, the algorithm and theory have been developed to process grayscale images[38]. In the recent years, mathematical morphology algorithms for color images have been developed[39]. P. Soille[40] categorized mathematical morphology applications into mainly three aspects of applications, which are image filtering, image segmentation and image measurement. He defined image filtering in mathematical morphology as performing a wide variety of tasks such as noise reduction, edge detection, compensation for incorrect focusing. Fig. 1.12 shows the application

example of filtering small blobs in a binary image with opening algorithm. Fig. 1.13 shows an example to eliminate the unevenness of light.

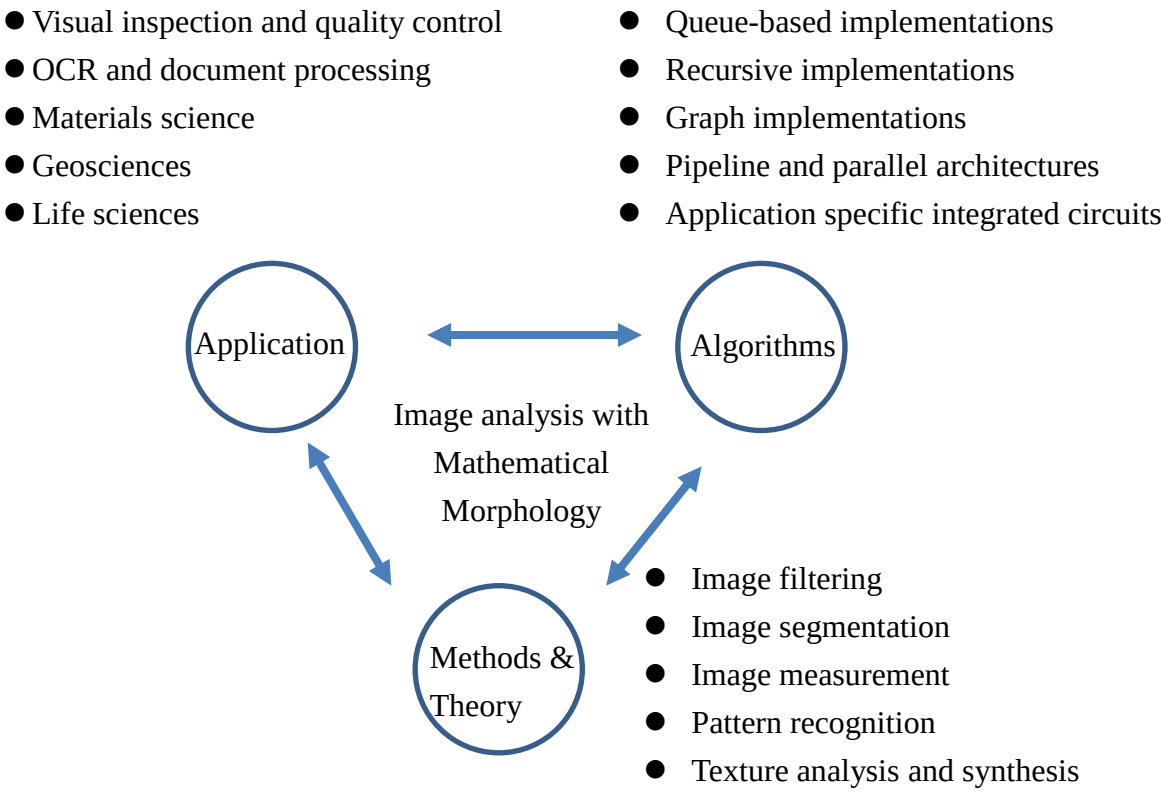

Fig. 1.11 The development of mathematical morphology is characterized by a cross-fertilization between applications, theory & methods, and algorithms[40].

Fig. 1.12 Application of mathematical morphology to filter small blobs in a binary

image.

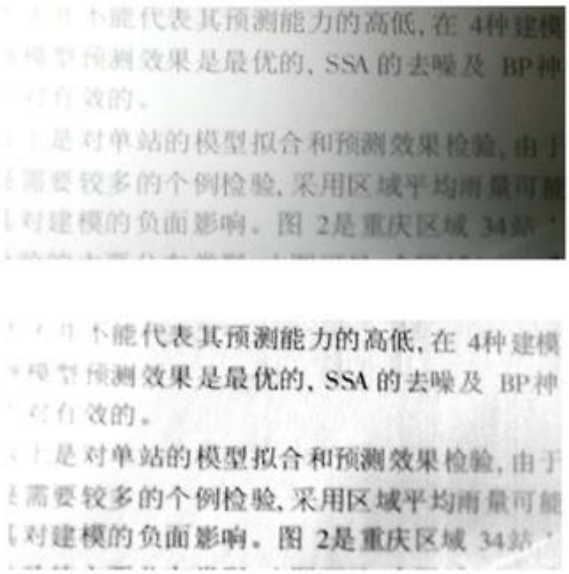

Fig. 1.13 Light unevenness elimination for document[41].

The image segmentation algorithm in mathematical morphology is watershed transformation. It firstly proposed in 1978 by D. Digabel and C. Lantuejoul[42-44]. L. Vincent and P. Soille[45] proposed an immersion model in 1991. In this model, the grayscale image was taken as a relief in which the surface height was equal to the grayscale of in-situ pixel. Water came into the basins from the minimum grayscales. Watershed line were built and when the water from different basins met. Fig. 1.15 shows the application of watershed transformation to spine segmentation.

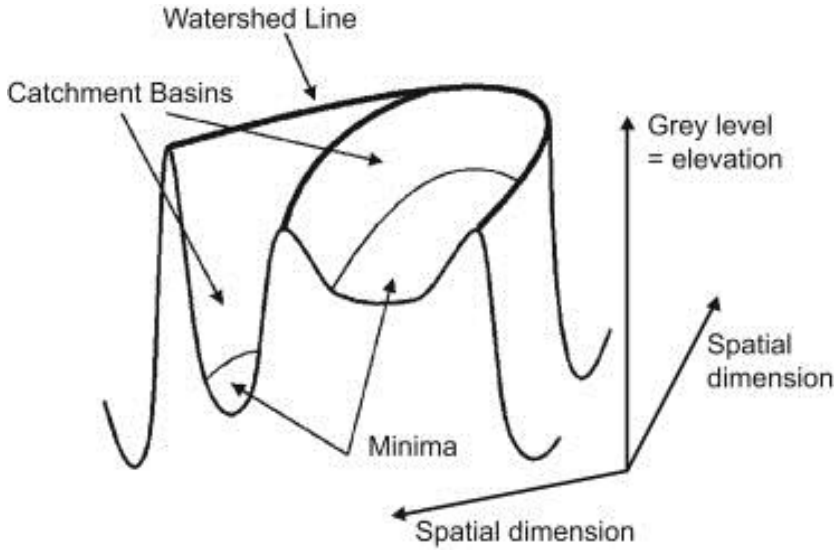

Fig. 1.14 Illustration of immersion model to calculate the watershed lines[46].

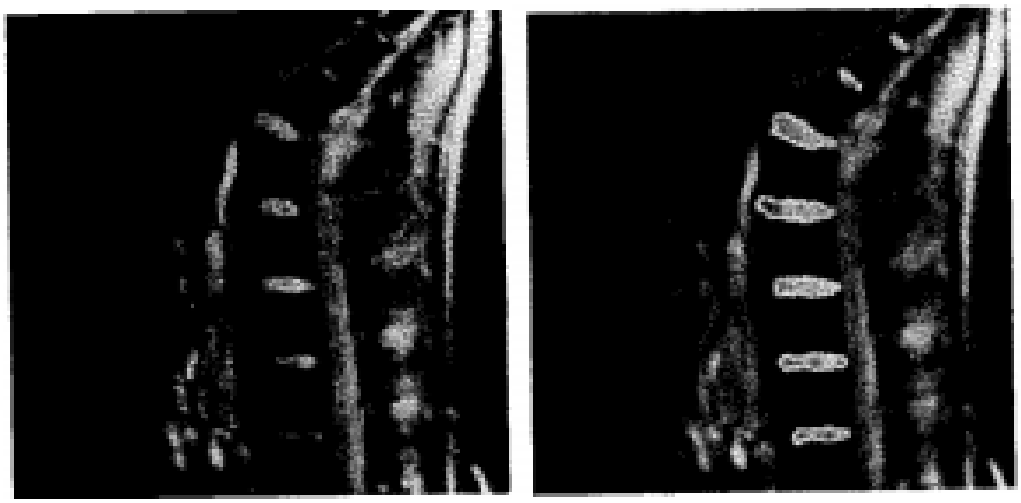

Fig. 1.15 Spine segmentation result with watershed transformation[45].

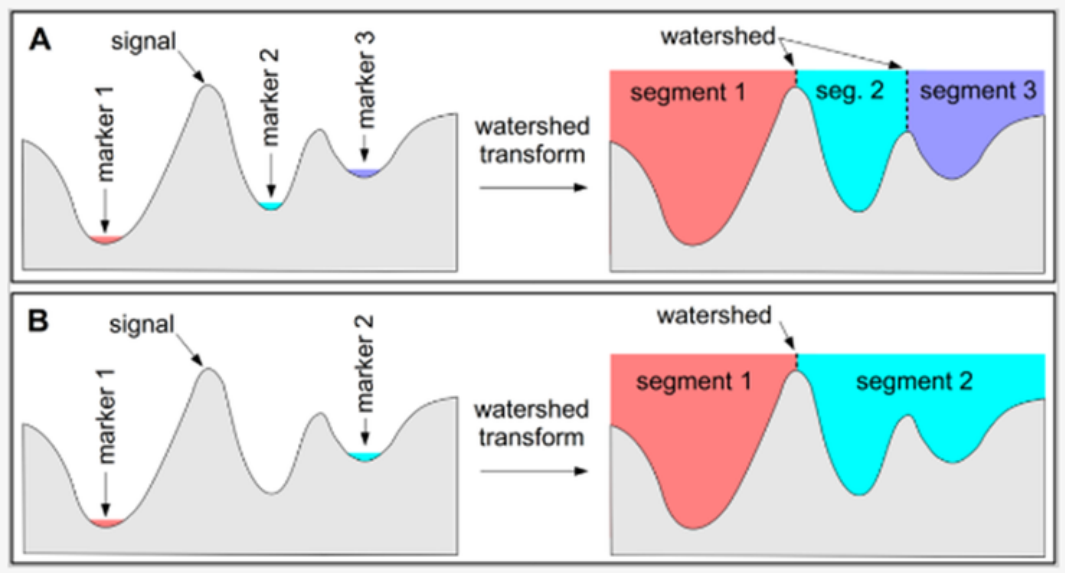

Fig. 1.16 Illustration of marker-controlled watershed.

The immersion model of watershed transformation is prone to generate over-segmentation. Marker-controlled watershed[47] (MCW) transformation is used to solve such a problem. As is depicted in Fig. 1.16, three markers were specified for watershed algorithm in case A. Therefore, the final segmentation result on the right had three parts. When only two markers were given in case B, the number of parts in the final result was two. Therefore, the number of regions achieved from the watershed transformation was decided by the number of markers.

Recently, many attempts have been done to solve complex situations in images. F. J. Chang[48] et al. developed a marker-image preparation method for the segmentation of gravels in sediment images. Fig. 1.17 shows the image segmentation procedure in his method. The original sediment image was processed with certain image techniques and then yielded a marker image shown in Fig. 1.17 (b). The final segmentation result is shown in Fig. 1.17 (c). It shows a good segmentation of gravels. J. Cousty[49] et al. used a

manually drawn markers to segment apple from the background, which is shown in Fig. 1.18. As can be seen in Fig. 1.18 (a), two markers were drawn manually. One is drawn to indicate the apple and the other is used to specify background.

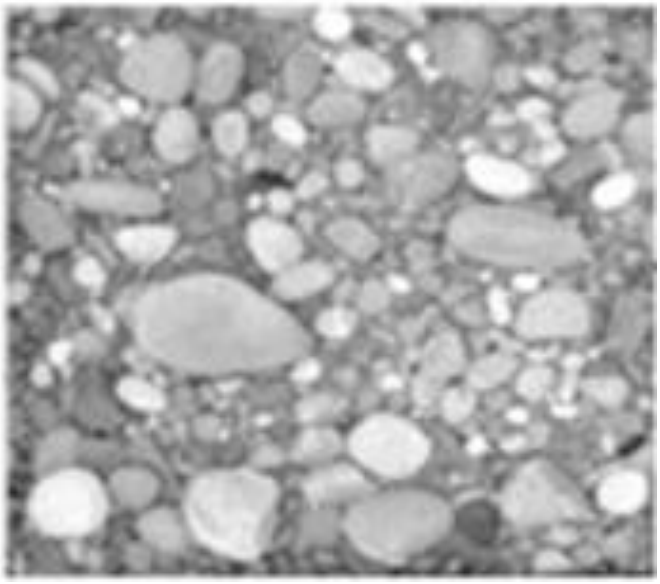

(a) Original gravel image

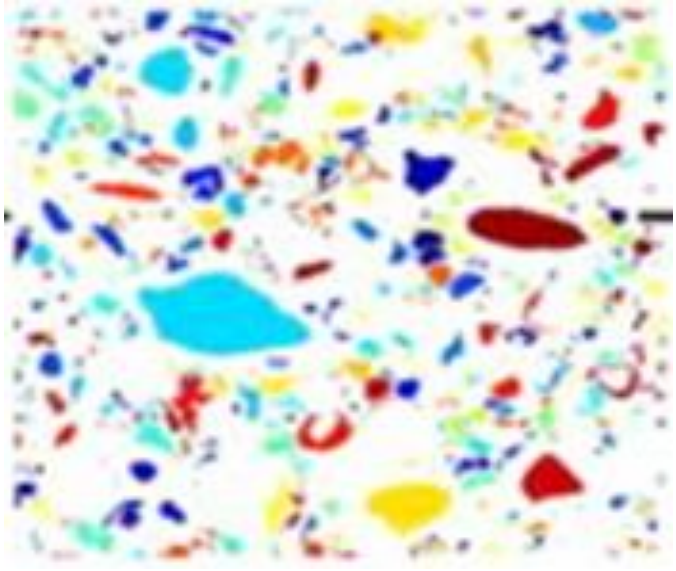

(b) markers prepared for gravels

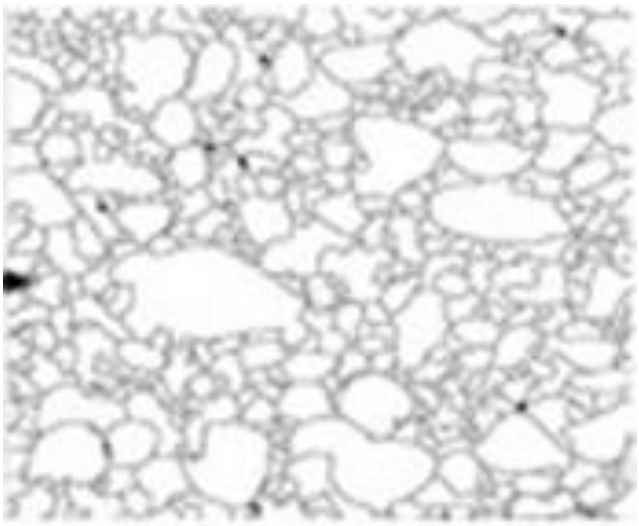

(c) MCW result

Fig. 1.17 Gravel segmentation in a sediment image.

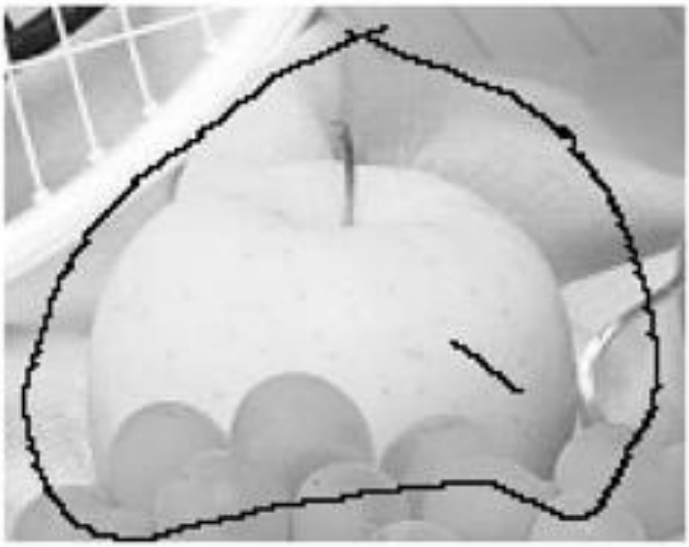

(a) Manually drawn markers to indicate apple and background

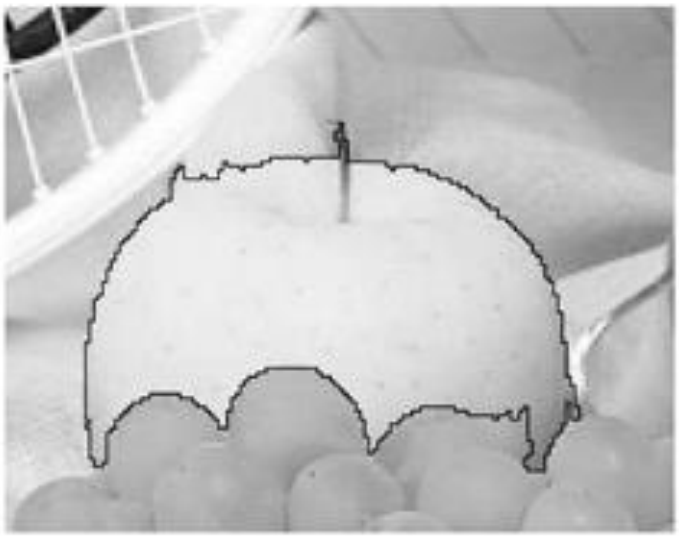

(b) final MCW result

Fig. 1.18 Apple segmentation result using manually drawn markers.

Image measurement with mathematical morphology involved the measurement of granulometry, directions and texture analysis.

1.2.2 Application of mathematical morphology in material microstructure analysis

S. Eddins[10] applied the watershed transformation to segment the steel optical image. It can be seen in Fig. 1.19 that the original immersion model generated so much over-segmentation. The application of marker-controlled watershed greatly improved the segmentation result.

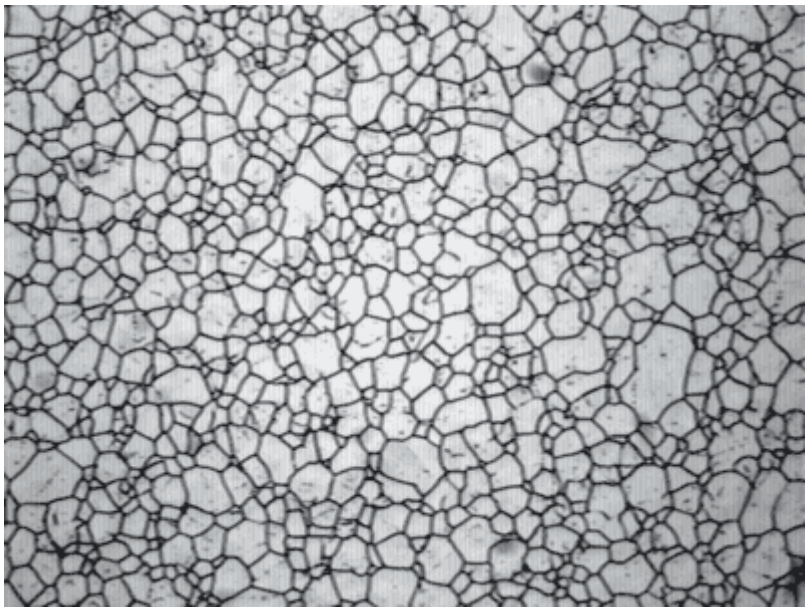

(a) Original optical image

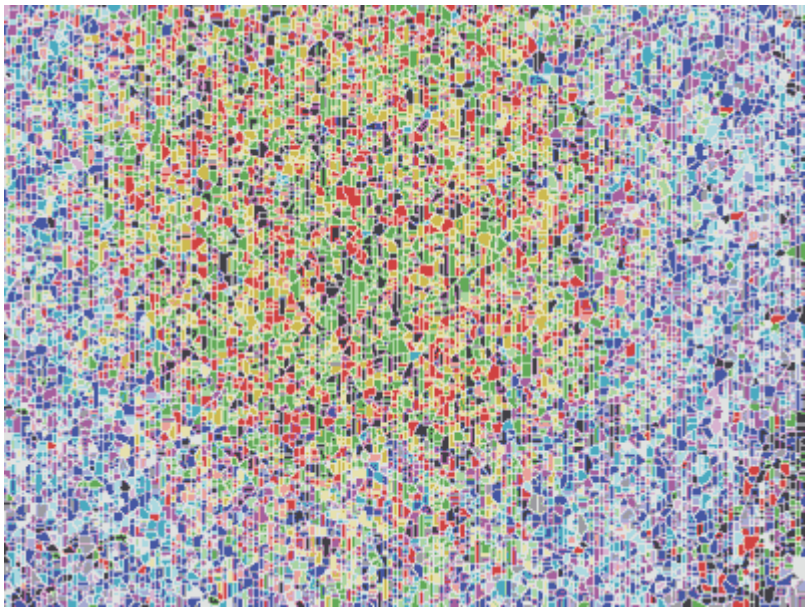

(b) Over-segmentation

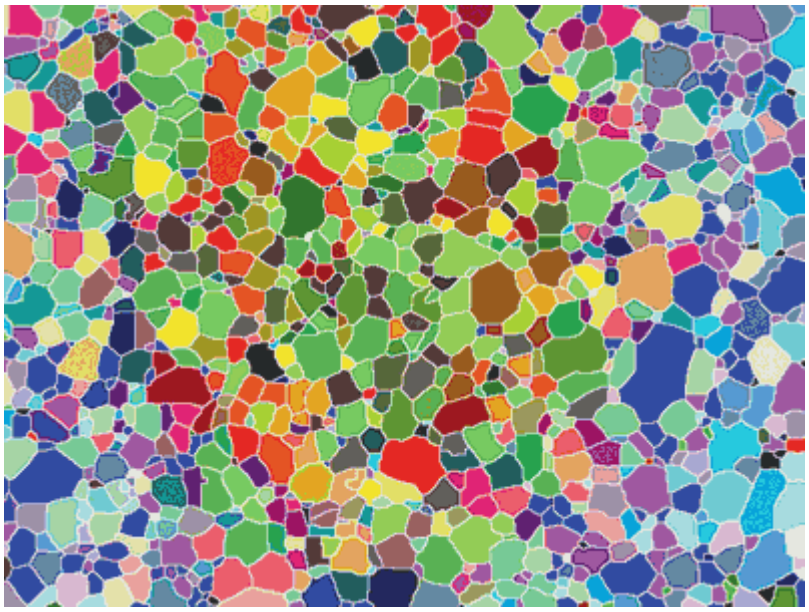

(c) Improved segmentation

Fig. 1.19 Steel microstructure with watershed transformation. a) original optical image, b) over-segmentation result with immersion model and c) improved segmentation with marker-controlled watershed (MCW).

The application of watershed transformation on the granular grains in steel presented good segmentation results. However, the shape of grains in material microstructure has many varieties. For instance, most of the primary α-Al phases in semi solid Al alloys are non-granular. Metal particles in ceramic matrix also appear sophisticated morphology. The conventional segmentation with watershed transformation is not enough to properly separate these phases or particles. A more difficult situation can be observed in the dendritic microstructures.

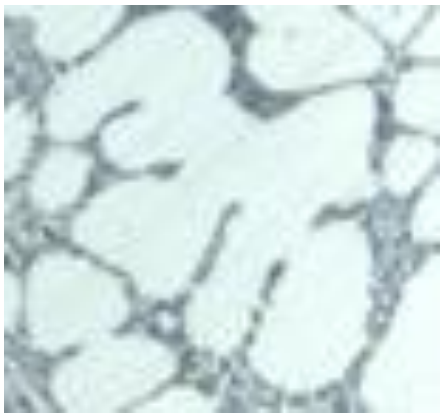

(a) Primary α-Al phase in semi-solid slurry

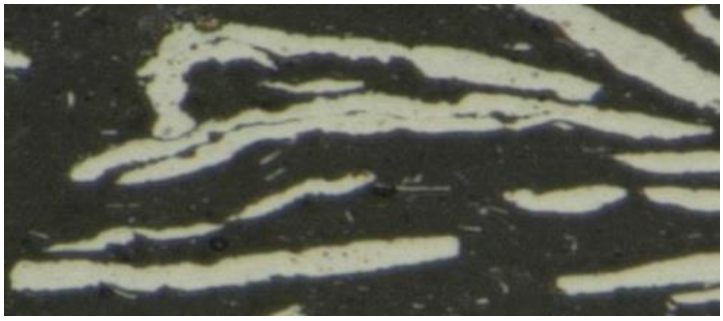

(b) metal particles in compound

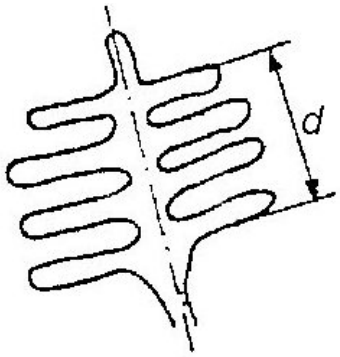

(c) dendrite

Fig. 1.20 Morphologies that difficult to segment with conventional watershed transformation .

1.3 Objectives and Outlines

As been addressed in the previous section, the current image processing method has problems in dealing with sophisticated grain shapes in material microstructure. Therefore, the objective of this thesis is as follows.

1. To develop an image processing method for segmenting non-granular primary α-Al phase and measure the size distribution for semi-solid Al alloy slurry.

2. To develop an image processing method for segmenting long-strip metal particles in compound and characterize its shape.

3. To develop an image processing method for secondary arm extraction in Al-Si alloy and measure the SDAS and DCS.

The structure of this thesis is as follows.

In chapter one, the main parameters to characterize material microstructure have been discussed and the conventional measuring methods of these parameters have been discussed. The progress of image segmentation method has been reviewed. Finally, the objective of this thesis has been explained.

In chapter two, the image segmentation method for non-granular primary α-Al phase has been developed and the primary α-Al phase size distribution has been measured.

In chapter three, the image segmentation method for long-strip metal particle in compound has been developed and the aspect ratio characterization method has been improved.

In chapter four, the image analysis method for secondary dendrite arm extraction has been developed and the dendritic morphology parameters, such as SDAS and DCS, are measured.

In chapter five, the main contents in every chapter will be summarized. The conclusions concluded from each chapter will also be shown.

References

1. P. P. Anosov, *Collected works*, Akademiya Nauk SSSR, 1954.
2. H. C. Sorby, *Philosophical Magazine Series 4*, 1856, **11**, 20-37.
3. A. Delesse, *Procédé mécénique pour déterminer la composition des roches*, Savy, 1862.
4. R. T. Howard and M. Cohen, *Trans. AIME*, 1947, **172**, 413.
5. C. S. Smith, *Grain shapes and other metallurgical applications of topology*, American Society for Metals, 1951.
6. S. A. Saltykov, *Metallurgizdat, Moscow*, 1958, **267**.
7. R. T. DeHoff and F. N. Rhines, *Quantitative Microscopy. (Papers Presented at a Symposium on Quantitative Metallography Held at the University of Florida, Gainesville 1961). Rhines: Symposium on Quantitative Metallography 1961*, McGraw-Hill, 1968.
8. E. E. Underwood, *Quantitative stereology*, Addison-Wesley Pub. Co., 1970.

9. F. William, *An introduction to probability theory and its applications*, 1950.

10. S. Eddins, *The Mathworks Journal, Matlab®, News and Notes*, 2002, 47-48.

11. V. Randle, *Materials Characterization*, 2009, **60**, 913-922.

12. D. Stokes, *Principles and practice of variable pressure: environmental scanning electron microscopy (VP-ESEM)*, John Wiley & Sons, 2008.

13. G. Binnig, C. F. Quate and C. Gerber, *Physical review letters*, 1986, **56**, 930.

14. B. Fultz and J. M. Howe, *Transmission electron microscopy and diffractometry of materials*, Springer Science & Business Media, 2012.

15. G. Binnig and H. Rohrer, *Surface science*, 1983, **126**, 236-244.

16. P. Das, S. Dutta and S. K. Samanta, *Proceedings of the Institution of Mechanical Engineers, Part B: Journal of Engineering Manufacture*, 2013, **227**, 1474-1483.

17. W. D. Callister and D. G. Rethwisch, *Materials science and engineering*, John Wiley & Sons NY, 2011.

18. R. DeHoff, *Materials Research*, 1999, **2**, 111-126.

19. E. Hall, *Proceedings of the Physical Society. Section B*, 1951, **64**, 747.

20. N. J. Petch and I. J. Iron Steel, *London*, 1953, **173**, 25.

21. V. K. Shante and S. Kirkpatrick, *Advances in Physics*, 1971, **20**, 325-357.

22. S. Kirkpatrick, *Physical Review Letters*, 1971, **27**, 1722.

23. F. Bueche, *Journal of Applied Physics*, 1972, **43**, 4837-4838.

24. A. Maaroufi, K. Haboubi, A. El Amarti and F. Carmona, *Journal of Materials Science*, 2004, **39**, 265-270.

25. A. Celzard, E. McRae, C. Deleuze, M. Dufort, G. Furdin and J. Marêché, *Physical Review B*, 1996, **53**, 6209.

26. R. Spear and G. Gardner, *AFS Transactions*, 1963, **71**, 209-215.

27. C. Caceres and B. Selling, *Materials Science and Engineering: A*, 1996, **220**, 109-116.

28. A. E1382-97(2010), *Standard Test Methods for Determining Average Grain Size Using Semiautomatic and Automatic Image Analysis*, ASTM International, West Conshohocken, PA, 2010.

29. B. Jennings and K. Parslow, in *Proceedings of the Royal Society of London A: Mathematical, Physical and Engineering Sciences*, The Royal Society, 1988, pp. 137-149.

30. H. G. Merkus, *Particle size measurements: fundamentals, practice, quality*, Springer Science & Business Media, 2009.

31. L. Gao, Y. Yan, G. Lu and R. M. Carter, *Flow Measurement and Instrumentation*, 2012, **27**, 20-28.

32. M. Coster and J.-L. Chermant, *Cement and Concrete Composites*, 2001, **23**, 133-151.

33. J. Prewitt and M. L. Mendelsohn, *Annals of the New York Academy of Sciences*, 1966, **128**, 1035-1053.

34. R. C. Gonzalez and R. E. Woods, *Digital Image Processing*, Pearson/Prentice Hall, 2008.

35. R. B. Cattell, *The journal of abnormal and social psychology*, 1943, **38**, 476.

36. J. Canny, *IEEE Transactions on pattern analysis and machine intelligence*, 1986, 679-698.

37. G. Matheron and J. Serra, in *Proc. 6th Intl. Symp. Mathematical Morphology*, Sydney, Australia, 2002, pp. 1-16.

38. J. Serra, *Image analysis and mathematical morphology, v. 1*, Academic press, 1982.

39. L. Najman and H. Talbot, *Mathematical morphology*, John Wiley & Sons, 2013.

40. P. Soille, *Morphological image analysis: principles and applications*, Springer Science & Business Media, 2013.

41. G. Wang, Y. Wang, H. Li, X. Chen, H. Lu, Y. Ma, C. Peng, Y. Wang and L. Tang, *PLOS ONE*, 2014, **9**, e110991.

42. S. Beucher and M. Bilodeau, in *Intelligent Vehicles' 94 Symposium, Proceedings of the*, IEEE, 1994, pp. 296-301.

43. S. Beucher and C. Lantuéjoul, 1979.

44. S. Beucher, in *Acoustics, Speech, and Signal Processing, IEEE International Conference on ICASSP'82.*, IEEE, 1982, pp. 1928-1931.

45. L. Vincent and P. Soille, *IEEE Transactions on Pattern Analysis & Machine*

Intelligence, 1991, 583-598.

46. Y. Tarabalka, J. Chanussot and J. A. Benediktsson, *Pattern Recognition*, 2010, **43**, 2367-2379.

47. W. Hartmann and A. Loderer, *Surface Topography: Metrology and Properties*, 2014, **2**, 044001.

48. F.-J. Chang and C.-H. Chung, *Journal of hydrology*, 2012, **440**, 102-112.

49. J. Cousty, G. Bertrand, L. Najman and M. Couprie, *IEEE Transactions on Pattern Analysis and Machine Intelligence*, 2009, **31**, 1362-1374.

Chapter 2. Primary α-Al grain size distribution measurement for semi-solid AC4CH slurry using mathematical morphology algorithms

2.1 Introduction

Aluminum die casting with semi-solid slurry is drawing attention due to its outstanding performance[1]. Usually, the homogeneous distribution of primary α-Al grain size in the semi-solid slurry is desirable. Varieties of semi-solid slurry preparation method[2-5] were proposed to achieve homogeneous morphology in the slurry. Usually, homogeneous primary grain size distribution in the semi-solid slurry is desirable for many products[6]. In the practice, primary grain size is measured from an optical image instead of a SEM image or EBSD image due to its convenient acquisition and low equipment-cost. A human subjective measurement can assure the accuracy and effectiveness of the measurement, whereas it is a tedious and labor-intensive process. Therefore, an image processing technique has been applied to improve the measurement

efficiency and to relieve the labor intensity. In the standard measurement method[7] with image processing technology suggested by ASTM international, a grain size in a bi-phase microstructure could be estimated with the ratio between total area and the total number of grain interested so as to avoid the troubles brought by the noises. However, this estimation method found difficulties for semi-solid Al slurry microstructures in which eutectic α-Al phase shared same color to primary α-Al phase. The volume fraction of primary and eutectic Al phase was much larger than the real fraction. P. Das[8] et al. conducted a detection of the edges of the primary α-Al and calculated fractal dimension[9] based on the edge detecting result. They found that the fractal dimension decreased when the average primary phase size upgraded. They attempt to generate a global factor to characterize the primary phase size. However, the homogeneity of the primary α-Al grain morphology could not be reflected from the mean grain size. A distribution histogram of the primary α-Al grain size will be more dedicated. B. Dutta[10] et al. reported that the interception method was capable of yielding a complete size distribution of chord length in primary and eutectic Al phase for an as cast microstructure of Al alloy after simple processing with mathematical morphology algorithms. They split the mean chord length in primary and eutectic Al with a statistical analysis manner. A systematic error must be removed for the calculation of mean chord length in primary α-Al. This method still yielded an estimation of mean value and could not directly tell the homogeneity of the primary α-Al grain.

The conventional primary α-Al grain size measurement measured the primary α-Al grain size averagely or indirectly. The difficulty in properly segmenting individual primary α-Al grains led to such a problem. Recently, mathematical morphology[11, 12] has been widely developed[13] and applied in many fields[14-17] to segment the overlapped cells

or congregated grains on the image with noises or unclear grain edges. Watershed algorithm[12] is one of the most frequently used image segmentation algorithms in mathematical morphology. However, the early local minima model (also can be called immersion model) of watershed algorithm[18] was prone to be influenced by the noises and sensitive to the grayscale variations in an image and hence resulted in much over-segmentation. S. Eddins[19] applied h-minima method to remove the minima that were too shallow and successfully suppressed the over-segmentation when he tried to make a proper segmentation for steel microstructure. This method worked well for the micrographs in which the individual grains had clear dividing lines. However, there are no such clear boundaries between the primary and eutectic Al phases in semi-solid Al-Si alloy slurry. A marker-image method[20] was reported to be capable of suppressing over-segmentation. L. Wojnar[21] used ultimate eroding method[13] to prepare the marker-images. He compared the segmentation result with conventional image processing techniques and concluded that watershed algorithm with markers yielded better segmentation result. R. Al-Raoush[22] prepared the ultimate eroding point markers by calculating the local maxima of Euclidean distance in the interested grains. He subsequently used the marker image to segment the granular particles in a bi-phase image and achieved good segmentation result. The results showed that the watershed algorithm yielded the best segmentation for congregated grains. One problem of the ultimate eroding point method is that it works well for granular-shaped grains[23-25] but produced much over-segmentation when the grain shape is non-granular. J. Cheng[26] et al. reported that shape markers prepared by thresholding Euclidean distance map greatly improved the image segmentation for the congregated objects. L. V. Valdés[27] et al. also reported that different shape markers by altering the threshold would yield different

segmentation quality. This provided a feasible candidate to facilitate the primary α-Al segmentation. However, there are still several problems that are hindering the application of watershed algorithm to the segmentation of primary α-Al in semi-solid slurries of Al alloys. Firstly, the semi-solid slurries of Al alloys mainly contain primary α-Al and eutectic phase. The eutectic phase is a mixture of secondary Al and Si phase. A contamination by the eutectic Al must be eliminated for accurate measurement of primary α-Al grain size. Secondly, the morphology of in semi-solid slurry is complex and non-granular. The present work describes a proposed image processing method for the semi-solid Al slurry microstructures based on the mathematical morphology to make an appropriate segmentation for primary α-Al grains and then to yield accurate primary phase grain size distribution histogram . Attention is given to discuss the advantages and disadvantages of the image processing methods.

2.2 Image analysis method for primary grain size measurement

A basic primary grain size measurement procedure with image processing is shown in Fig.2.1. It includes four steps in sequence. Firstly, optical images should be taken from the specimens and be converted into proper format. Secondly, primary grain edges should be identified in the pre-processing procedure to eliminate its influence on the final result. In the next step, the primary grains would be segmented into optically separated grains and identified with image segmentation algorithms. The objective in this step is to achieve separated individual primary grains. Finally, individual primary

grain size could be measured with certain method. The desired result was the primary grain size distribution histograms.

2.2.1 Original image acquisition

The original optical image was taken from an AC4CH alloy with 450 × magnification. The image size was 1600×1200 (pixel × pixel). The pixel length was 0.356μm. The optical image was converted into grayscale image for the reason that it is not necessary to perform image analysis on color images. Firstly, the optical images of aluminum alloys were not colorful. And secondly, segmenting color images usually consumed much longer time and higher computation resources than segmenting grayscale images. An original image of AC4CH alloy is shown in Fig. 2.2

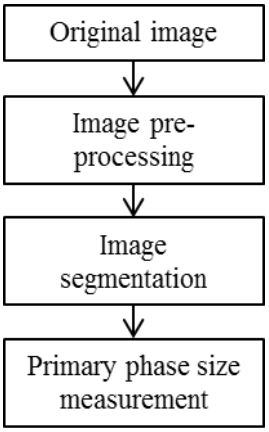

Fig.2.1 Flowchart of the image processing procedure.

2.2.2 Image pre-processing

After the etching during sample preparation, Al grain and Si grain appeared two different grayscale in the optics. The Al grains were bright and Si grains were dark. We could easily identify the Si grains by implementing binarization[28] on the original

grayscale image. The key parameter was the threshold for binarization.

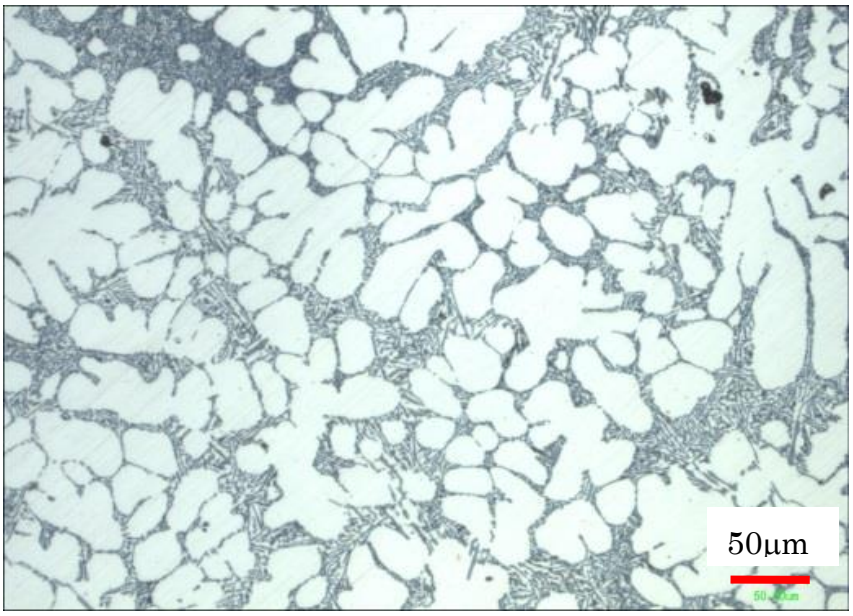

Fig. 2.2 Optical image of AC4CH alloy.

Fig.2.3 illustrates the method to select a threshold for binarization in this study and its result. Firstly, the grayscale at central line of the original image was extracted and listed in a chart. Secondly, the grayscale variation at the borders between Al grains and Si grains was observed and then a threshold higher than the grayscale of Si grains but lower than the grayscale of Al grains was selected. We selected 194 as the threshold in this case and produced the result. It is shown in Fig. 2.3 (b) that this threshold well accomplished the task to identify Al grains and Si grains.

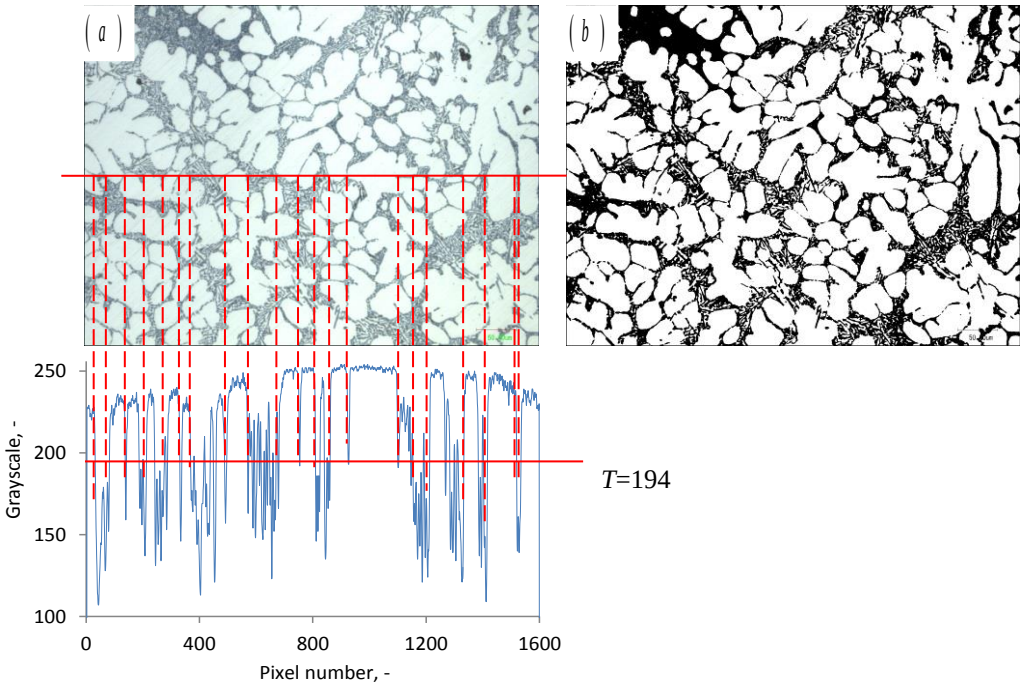

Fig.2.3 Grayscale values at the central line of original image and the binarization result. a) Original grayscale image and the grayscale at its central line; and b) binarization result using threshold T = 194, the white object is Al grains and the black background is Si grain.

2.2.3 Image segmentation

Watershed transformation (WST) was the most commonly used mathematical morphology algorithm to segment congregated grains in an image. In the early models of WST[13], over-segmentation was very common due to the sensitiveness to the grayscale variation. A marker-controlled watershed[29] (MCW) algorithm well solved such a problem. It employed a marker image to specify the location of the grain nuclei. The quality of the prepared marker-image determined the results of segmentation. In the frequently used image analysis software ImageJ, the marker image is prepared with ultimate eroding points (UEP) method[18]. However, the UEP method would generate several markers for one primary grain if the grain was not equiaxed.

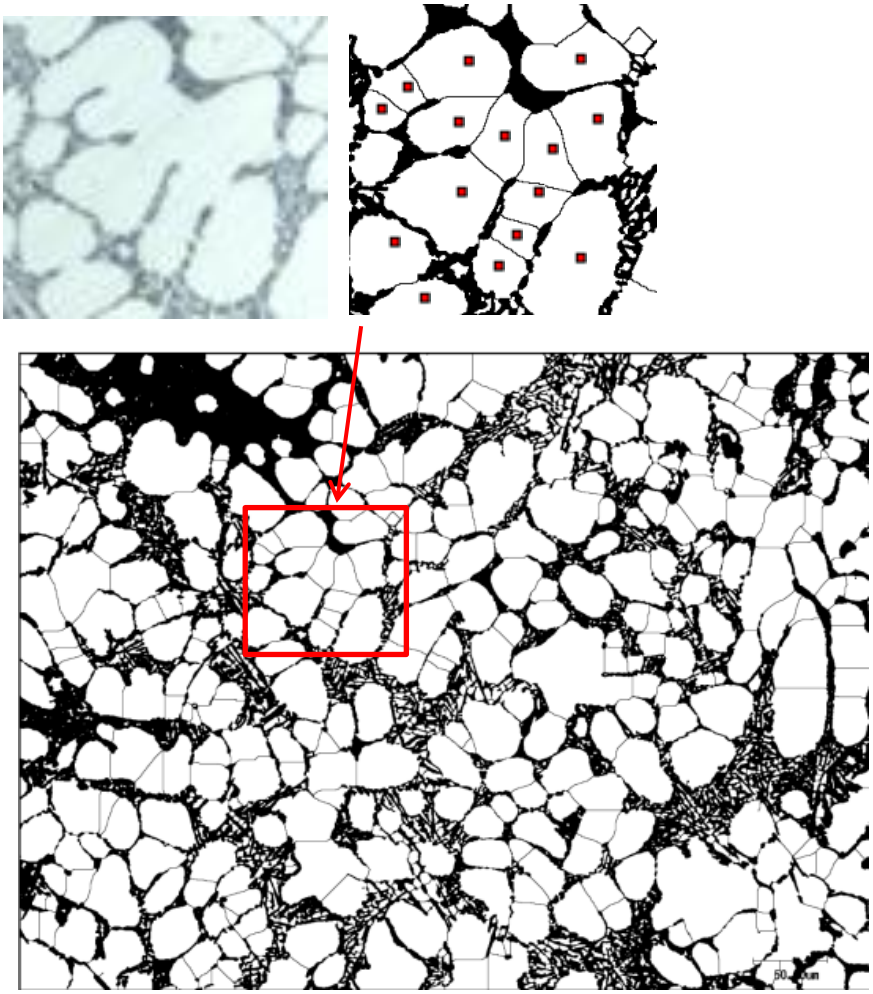

Fig. 2.4 Image segmentation result for a semi-solid slurry structure with watershed function in imageJ.

Fig. 2.4 shows an example of over-segmentation with marker-image prepared with UEP method. It was implemented on the binary image in Fig. 2.3(b) with ImageJ analysis software. It can be seen that many false boundaries were constructed. The large, unequiaxed primary grains had been mistakenly split into small regions. The anisotropy of the primary grains caused the multi-existence of UEP for one grain and thus resulted

in the numerous over-segmentations.

2.2.4 Primary grain size measurement

We can measure the individual grain area after the image segmentation. Usually, equivalent diameter is used to characterize grain size. Fig. 2.5 illustrates the calculation mechanism of equivalent diameter for one grain. The equivalent diameter of a grain is the diameter of a circle with same area to the grain. The algorithm is depicted by Eq. 2.1.

$$d_{equivalent} = 2\sqrt{\frac{A}{\pi}} \tag{2.1}$$

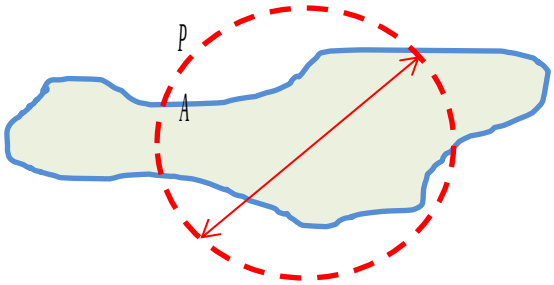

Fig. 2.5 Illustration of equivalent diameter.

Fig. 2.6 shows the manual measurement for one primary grain cell. The red line is the manually drawn polygon. The area of the polygon will be used as the area of the primary grain, which is 3381.82μm^2 for this primary grain cell. This method is accurate to yield a distribution of primary grain size, but the efficiency is low and requires large labor-intensity.

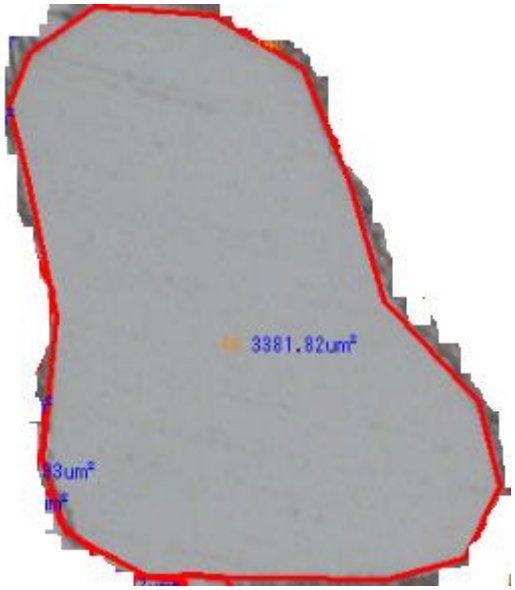

Fig. 2.6 Manual measurement result of primary grain size distribution.

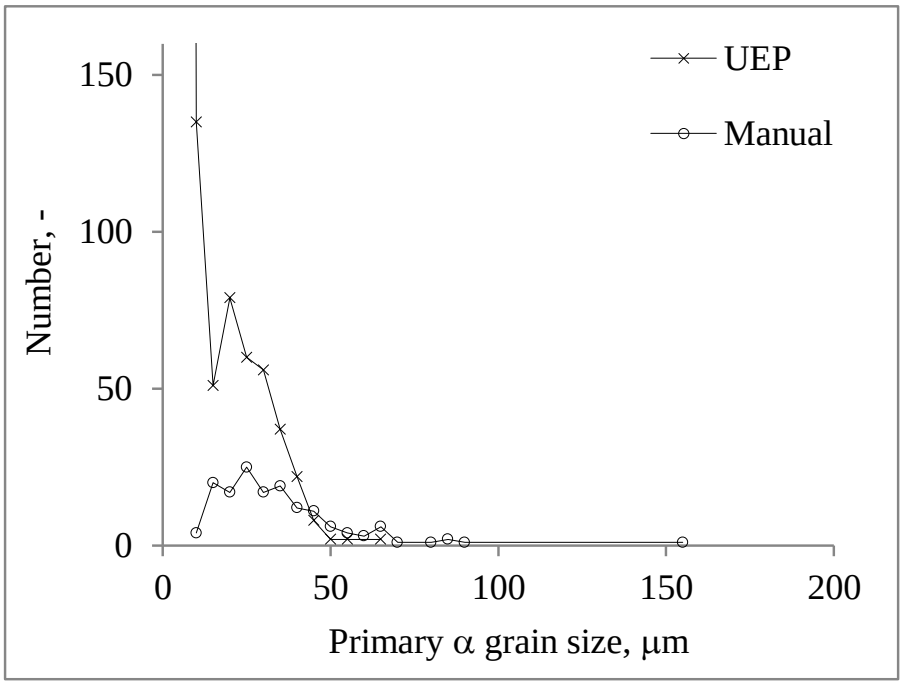

Fig. 2.7 Primary grain size measurement result with manual method and UEP method.

Fig. 2.7 shows the measurement result of primary grain size distribution with manual

method and conventional image processing method. The image processing method is carried out with ImageJ software. The maximum primary α-Al grain size with manual measurement is 155μm, whereas that of the image analysis method with UEP method is only 65μm. This is caused by the over-segmentation of excess markers generated by UEP method. In contrast, the number of those larger than 10μm and smaller than 40μm is over-estimated. Apparently, the image analysis method using UEP markers failed to yield close result to the manual result. The image analysis method has to be improved.

2.3 Improvement of the image segmentation

2.3.1 Image segmentation with shape markers prepared by Euclidean distance map method

Shape markers[26] prepared with Euclidean distance map is reported to be able to reduce over-segmentation. The preparation of marker-image with EDM method (see in Appendix 1.6) is as follows. In the first step, the Euclidean distance from white pixels to the closest black pixels was calculated pixel wise to obtain the Euclidean distance map. In the second step, the Euclidean distance map was binarized to remove white pixels which were close to black pixels. An example of shape markers prepared for primary α-Al grain is shown in Fig. 2.8(a). The red shape is the marker prepared. Obviously, the shape markers well preserved the integrality of primary α-Al grain. Fig. 2.8(b) shows the markers prepared with EDM method for the actual grayscale original image. Obviously, the shape markers prepared with EDM method preserves the integrality of a primary Al grain and generated separated markers for congregated grains.

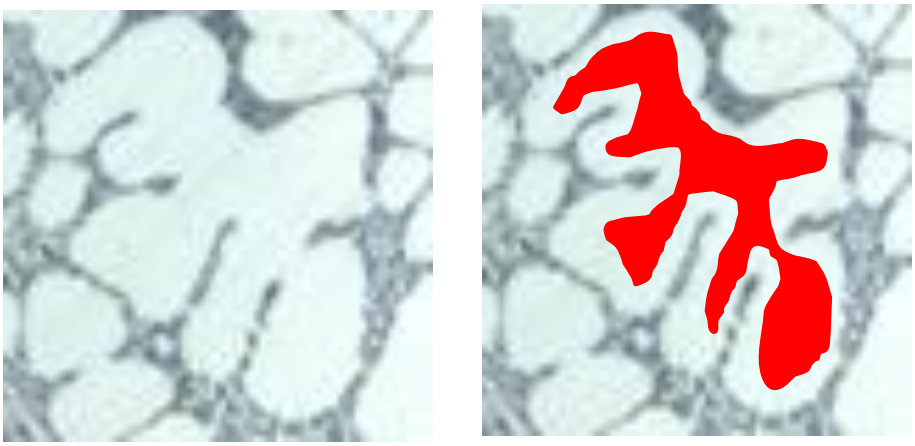

(a) Example of shape marker prepared with EDM method

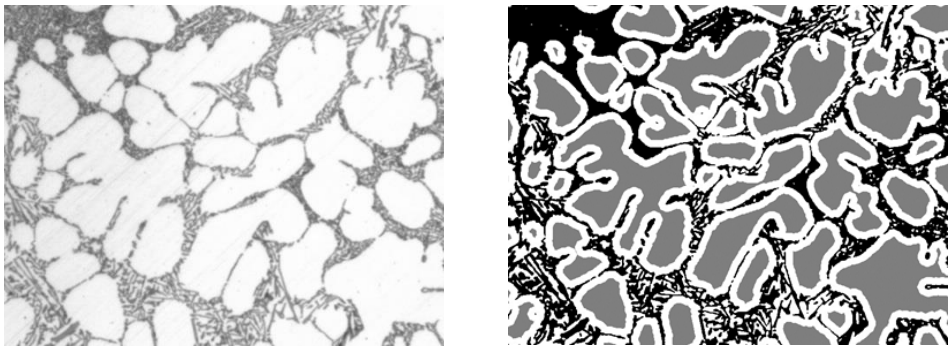

(b) Actual original grayscale image and markers prepared with EDM method

Fig. 2.8 Example of shape marker prepared with EDM method.

The threshold used to binarizing Euclidean distance is important. This is because large threshold will produce excess markers while small threshold will fail to generate separated markers for congregated primary α-Al grains. In general, the Euclidean distance will be normalized. After normalization, the maximum Euclidean distance became 1 and the minimum distance became 0. The other Euclidean distance will be calculated proportionally.

When we mention distance threshold in this chapter, we mean the threshold for the normalized value. Image segmentation using EDM marker-image is shown in Fig. 2.9

(a). The Si phase has been removed and the result is shown in Fig. 2.9 (b). The distance threshold is 0.2. The black pixels are the silicon grain identified in Fig. 2.3 (b). Different primary α-Al grains are painted with different colors. It can be seen that the integrality of the primary grains has been well preserved. One problem is that the α-Al grains in eutectic grains have been classified into the neighboring primary α-Al grains. This deteriorates the final primary grain size measurement result.

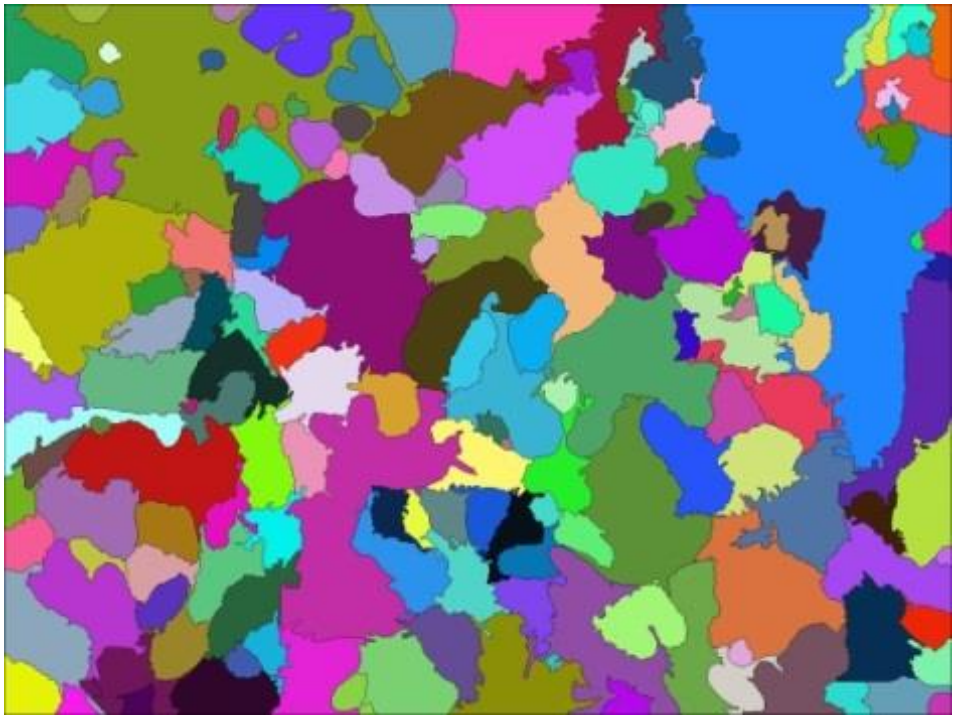

(a) Watershed transformation result with EDM markers

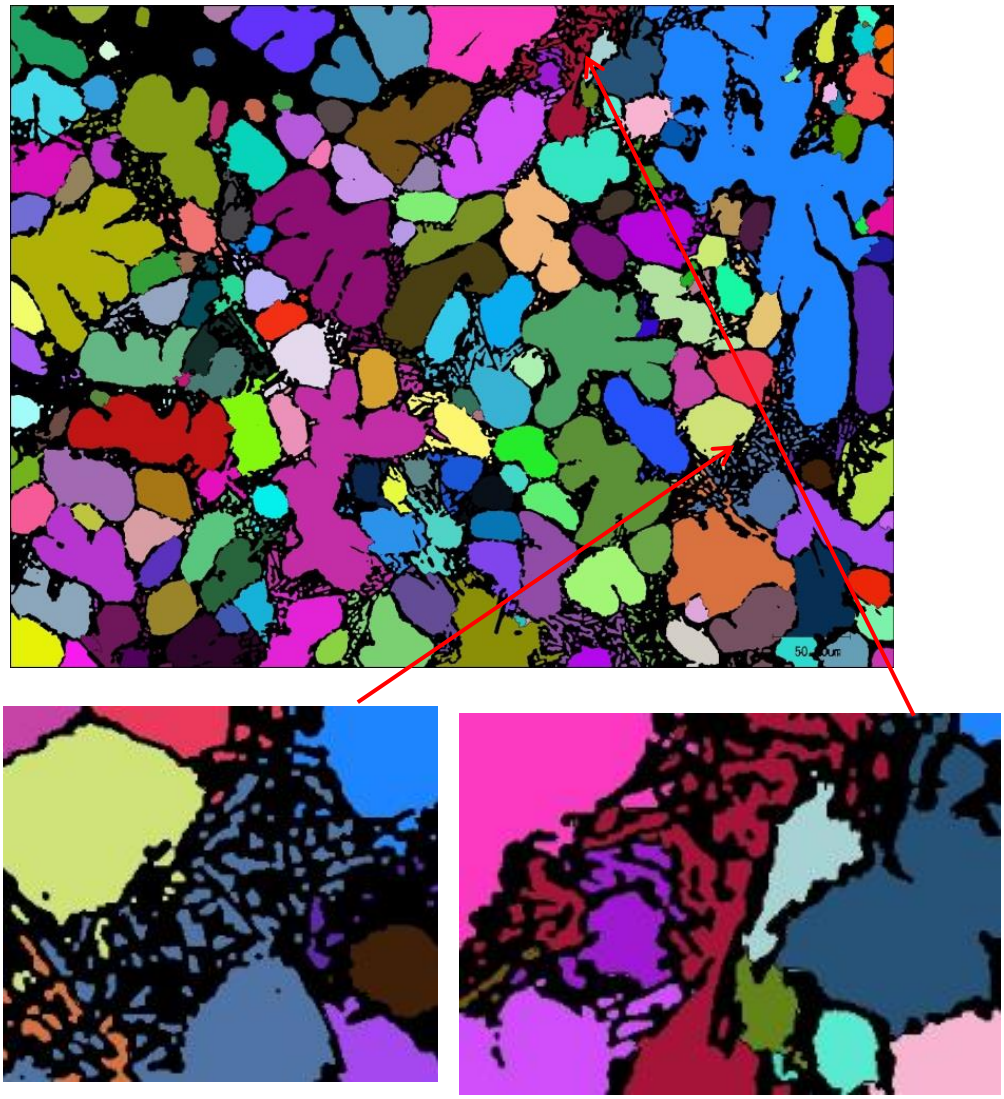

(b) Primary phase segmentation result after filtering Si phase

Fig. 2.9 Image segmentation result of the Euclidean distance map method

Fig. 2.10 shows the primary α-Al grain size distribution measured from the image segmentation result of Fig. 2.9. The maximum primary α-Al grain was over-estimated. This is because that the eutectic Al grains were identified as part of the primary α-Al grains. Another problem is that the number of grains within [10μm, 40μm] was under-estimated. It can be seen that the measurement result was still far away from the manual result. Therefore, the influence of eutectic Al grains has to be eliminated.

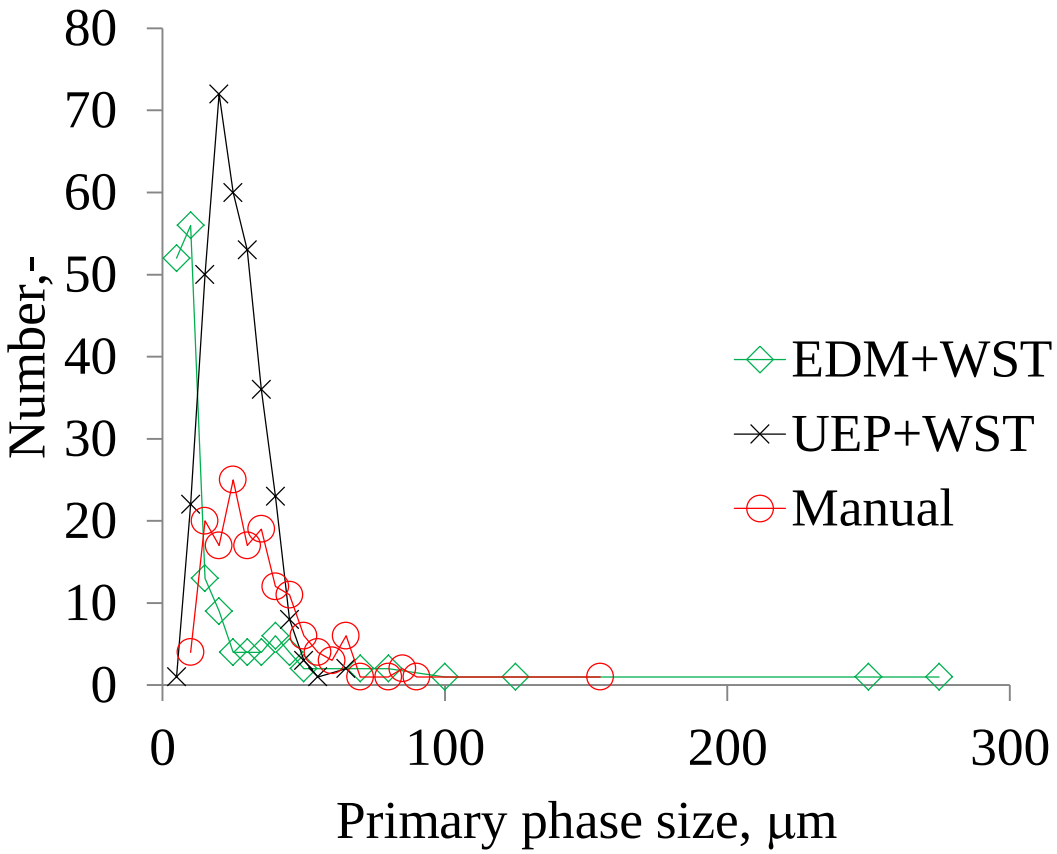

Fig. 2.10 Primary grain size distribution measured by EDM method.

2.3.2 Identification of the primary α-Al grain

Opening (see in Appendix 1.3) algorithm is a mathematical morphology transformation used to eliminate the small blobs. Fig. 2.11(a) and Fig. 2.11(b) shows an application example of opening to eliminate the small white particles. Obviously, the small white particles have been eliminated while the shape of the large white particles preserved their shapes. The size of particles it can remove depends on the kernel size and shape of structuring element in the opening algorithm. Fig. 2.11(c) shows an application of opening operation. In the microstructure of semi-solid slurry of AC4CH alloy, mainly four types of grains exist. They are large size primary α-Al grain, small

size primary α-Al grain, eutectic Al grain and Si grain, respectively. The kernel size of the opening operation should be carefully selected so that the opening operation could remove all the eutectic Al grains and preserve every primary α-Al grain. Therefore, we selected 3 candidate kernel sizes for the opening operation. They are 4, 7 and 12 pixels. It can be seen that some eutectic Al grain was not removed when the kernel size is small. When the kernel size is too large, some small primary α-Al grains were removed and the other small primary α-Al grains became rectangle shape. In comparison, when the kernel size is 7, the small primary α-Al grains were preserved while the eutectic Al grains were removed.

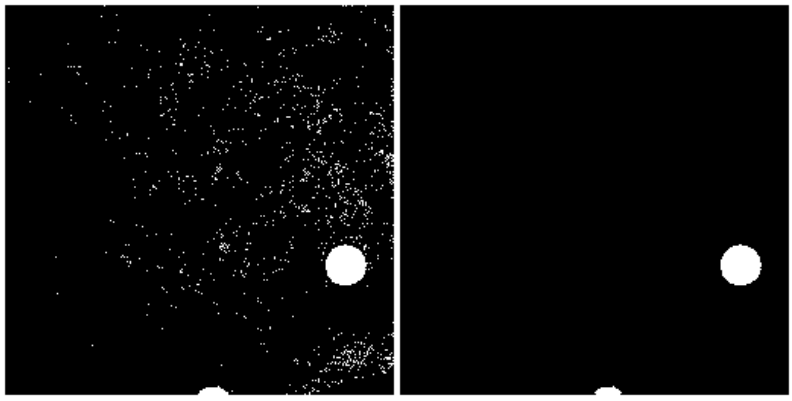

(a) (b)

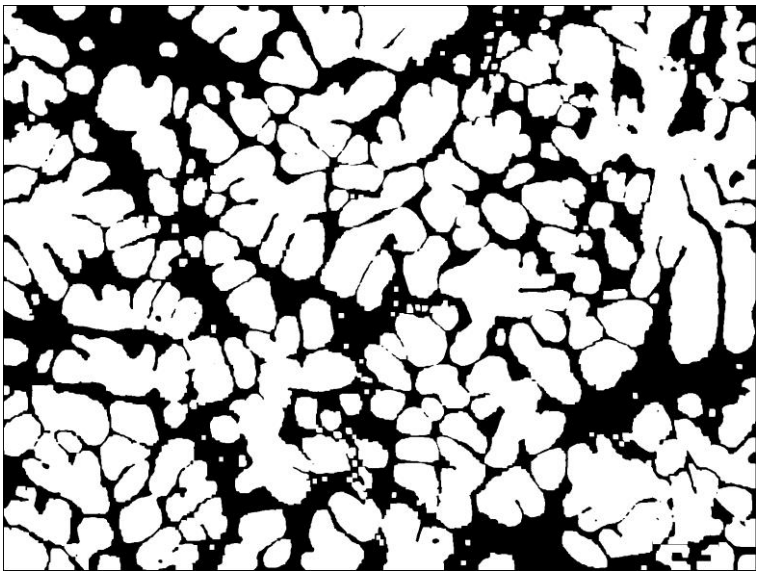

(c)

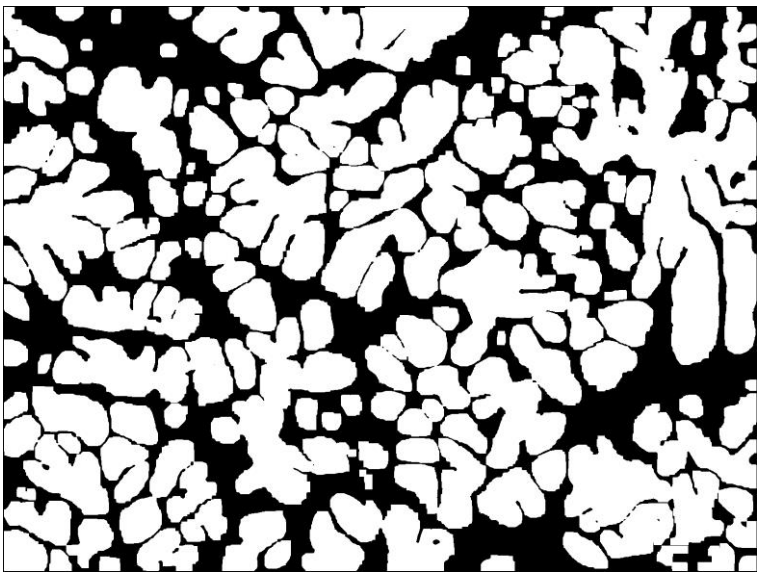

(d)

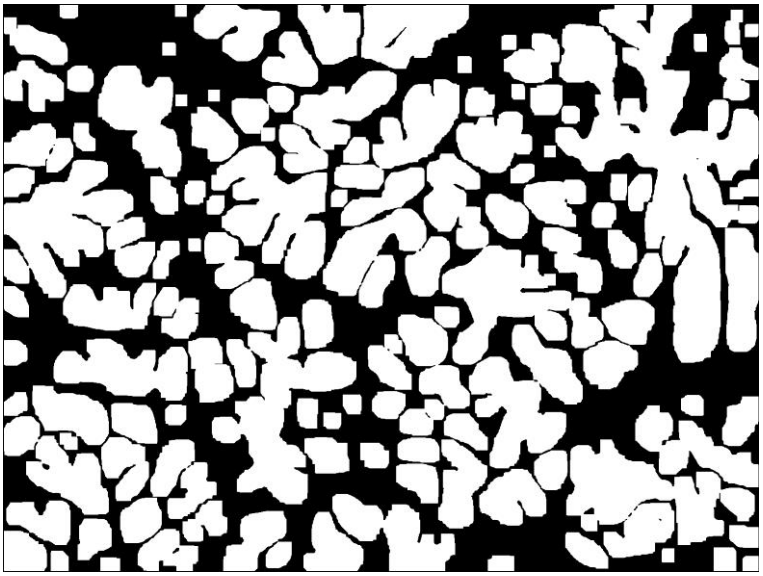

(e)

Fig. 2.11 Example of opening operation. (a) Sample image with small white noises before opening, (b) Result image after opening operation, (c) open result of Fig. 2.3(b) with kernel size 4 pixels, (d) open result of Fig. 2.3(b) with kernel size 7 pixels and (e) open result of Fig. 2.3(b) with kernel size 12 pixels.

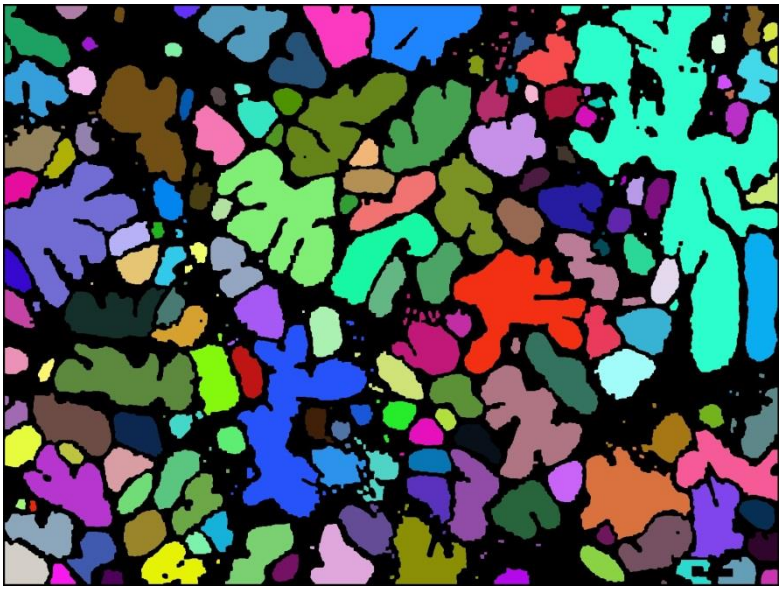

(a) Structuring element kernel size is 4 pixels

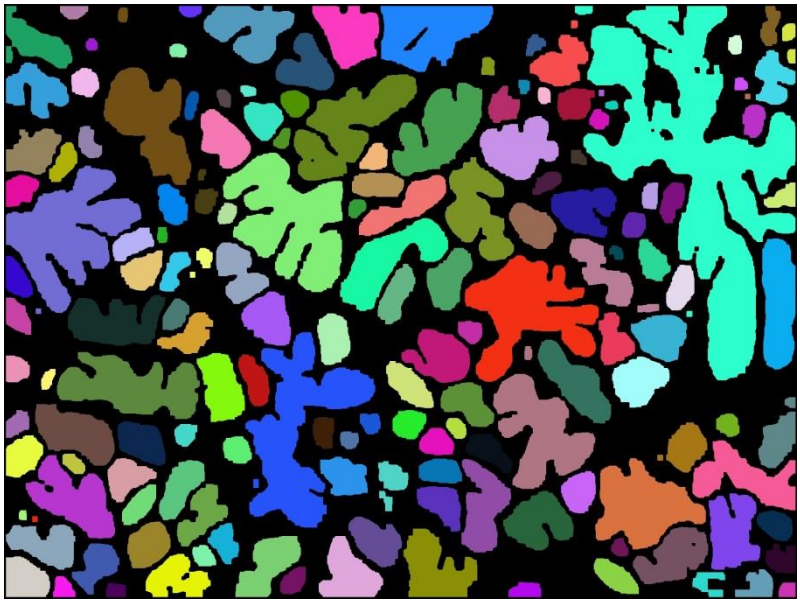

(b) Structuring element kernel size is 7 pixels

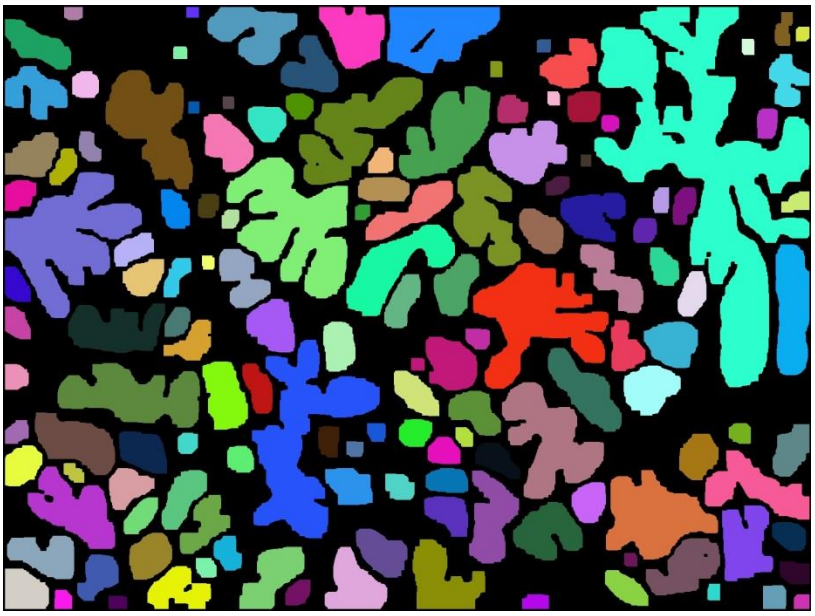

(c) Structuring element kernel size is 12 pixels

Fig. 2.12 Opening result of Fig. 2.9. Structuring element shape is a square and the kernel size is 12 pixels. (a) Structuring element kernel size is 4 pixels, (b) Structuring element kernel size is 7 pixels and (c) Structuring element kernel size is 12 pixels.

The primary grain size measurement results are shown in Fig. 2.13. All the kernel size yielded much better result than the conventional method. A further observation into the results of the three kernel size shows that kernel size 4 over-estimated the small size primary grain. This is because the mall kernel size cannot remove all the eutectic grains. In fact, kernel size 12 will also remove some small primary grains. However, there is over-segmentation brought by porosities. The kernel size 7 gives the best elimination result of eutectic grains. There is still a little over-estimation of large size primary α-Al grains. This is resulted from the under-segmentation of small primary α-Al grains. When we prepare the shape markers by binarizing Euclidean distance map, the

maximum distance within some small primary grains were smaller than the threshold. Thus, there were no markers generated for the small size primary α-Al grains. These grains were not eliminated by opening, either. They were classified into their neighboring large α-Al grains. Then, the size of the maximum primary α-Al grain was over-estimated and the number of the large primary α-Al grains was also over-estimated.

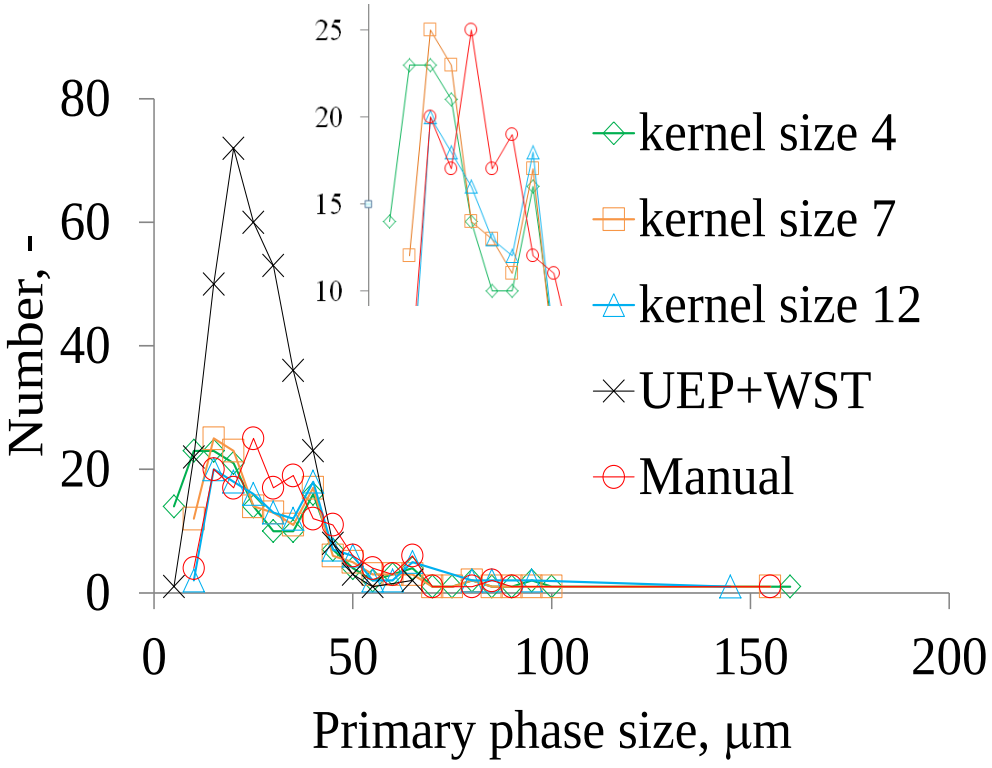

Fig. 2.13 The comparison of primary grain size distribution result with different kernel size of structuring element in opening.

2.3.3 Identification of small primary grains

Some primary grains are very small. The EDM method failed to prepare a marker

for such small primary grains. Meanwhile, they were not eliminated by the opening algorithm. Thus, they will be takes as part of their neighboring primary grains. Fig. 2.14 shows the failures of identification for some small primary α-Al grains. This leads to over-estimation of large primary grains and under-estimation of small primary grains. In this section, we applied watershed transformation for the second time to segment this kind of small primary grains. The marker-image in the second watershed transformation is prepared from the result of opening. The objects in the opening result have been eroded with a rectangle structuring element whose size is 1 pixel.

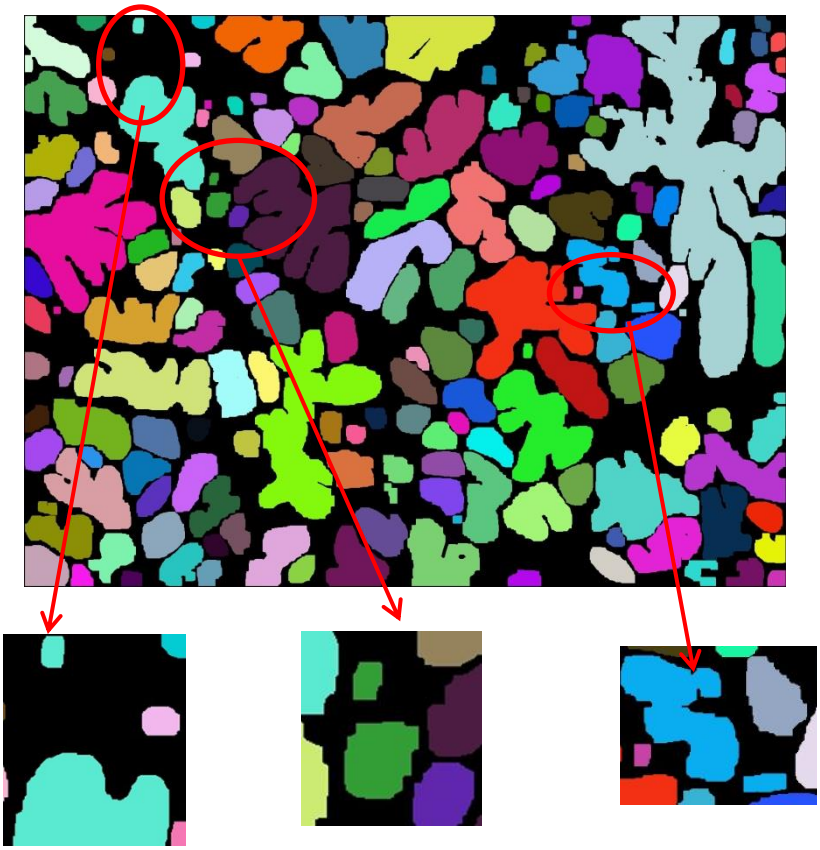

Fig. 2.14 Illustration of the failure for small primary α-Al grains.

(a) Second watershed transformation result

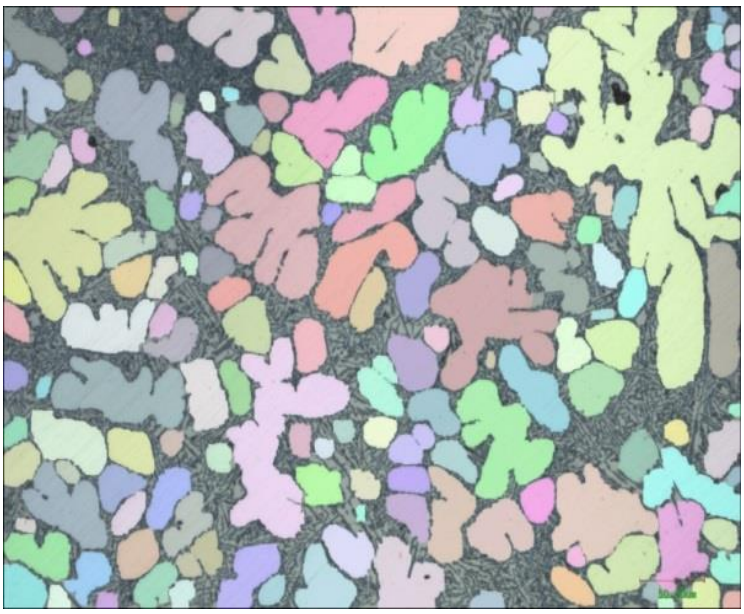

(b) Primary phase identification after filtering eutectic phase.

Fig. 2.15 Final image segmentation result for primary grains. The segmentation results have been combined with original image.

Fig. 2.15(a) shows the second watershed transformation result. The eutectic phase has been removed and segmentation result is shown in Fig. 2.15(b). Original grayscale image was also added into the segmentation result to demonstrate the segmentation effectiveness. The structuring element for opening was a rectangle which kernel size was 7 pixels. It can be seen visually that the primary grains have been well segmented. The primary grain size distribution result is shown in Fig. 2.16. It can be seen from the data that the proposed method yielded a close result to the manual measurement.

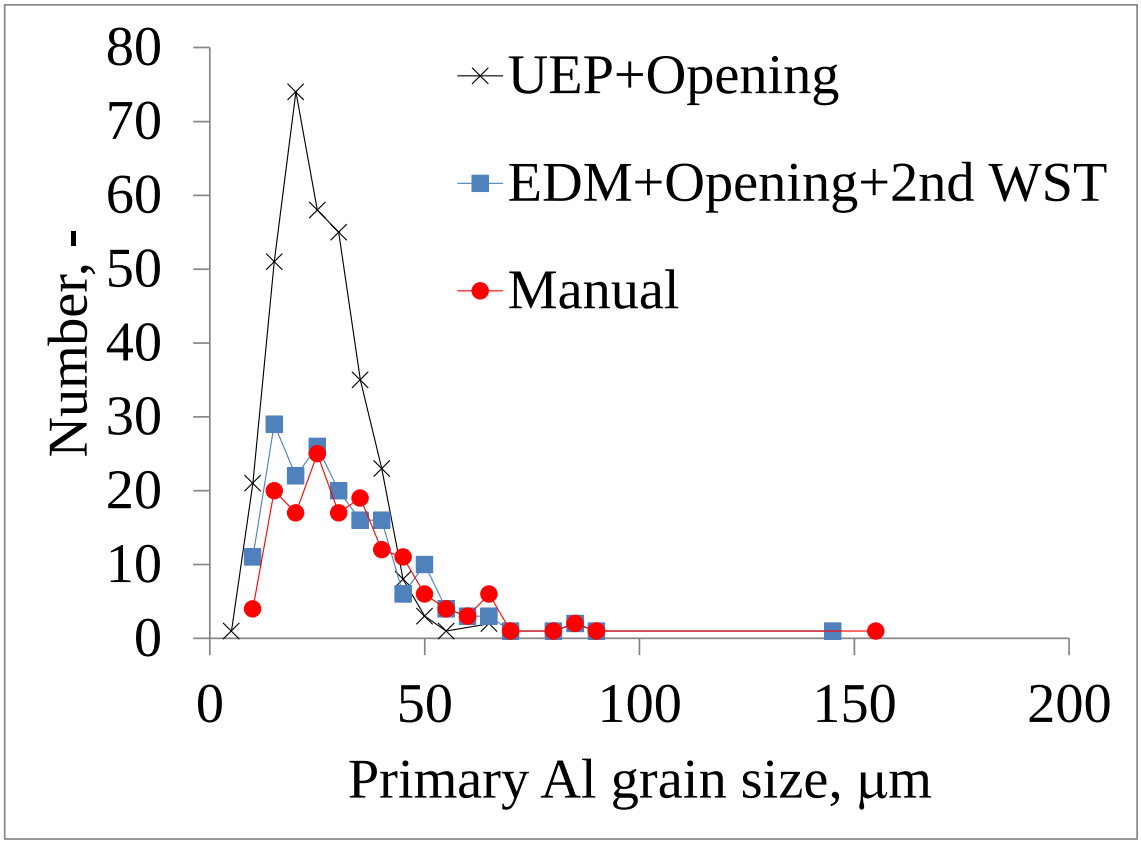

Fig. 2. 16 Final primary grain size distribution result.

2.3.4 The influence of Euclidean distance threshold

Besides the structuring element kernel size, the distance threshold for preparing

marker image from EDM image also influences the measurement result. In this step, the Euclidean distance of each pixel was normalized. i.e. the maximum Euclidean distance was set to 1 and the minimum distance was 0. Fig. 2.17 shows the markers prepared with EDM by different threshold. The gray shapes are the markers. It can be seen that congregated grains share one marker when the threshold is small (0.10) and one primary Al grain has two markers when the threshold is large (0.25). A marker prepared with intermediate threshold (0.20) will yield a proper marker which separates the congregated grains while preserves integrality of the other grains.

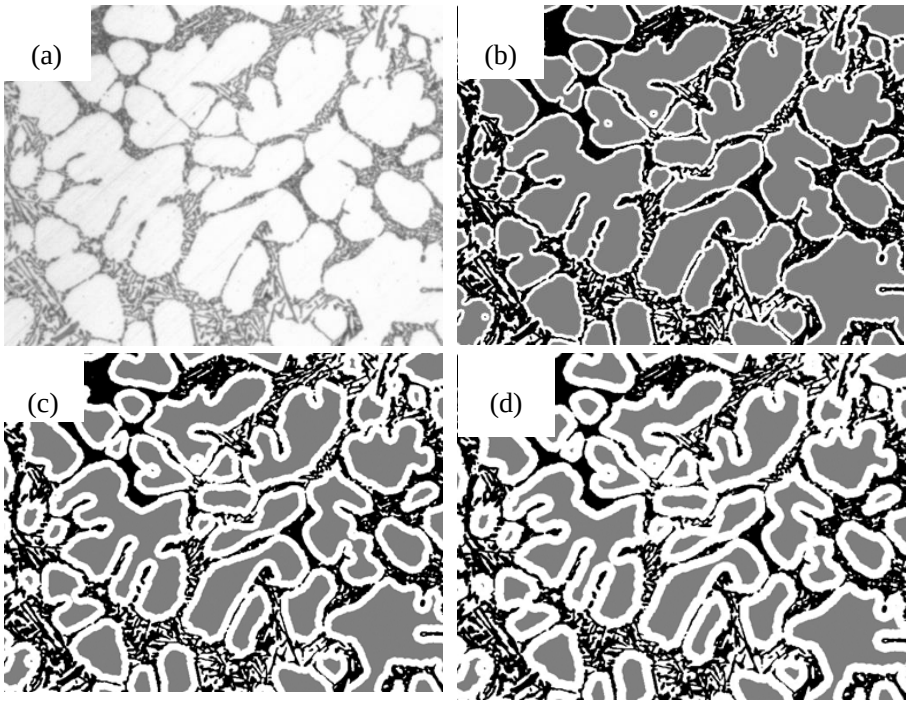

Fig. 2.17 Influence of Euclidean distance threshold for preparing markers (gray objects). (a) Original grayscale image, (b) markers prepared with distance threshold of 0.1 times of maximum distance, (c) markers prepared with distance threshold 0.2 times of maximum distance and (d) markers prepared with distance threshold 0.25 times of maximum distance.

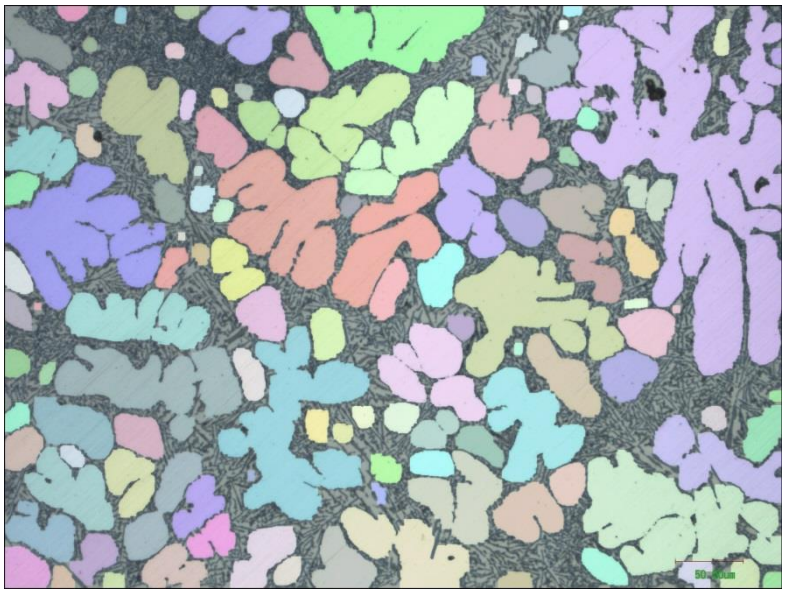

(a) Euclidean distance threshold = 0.10

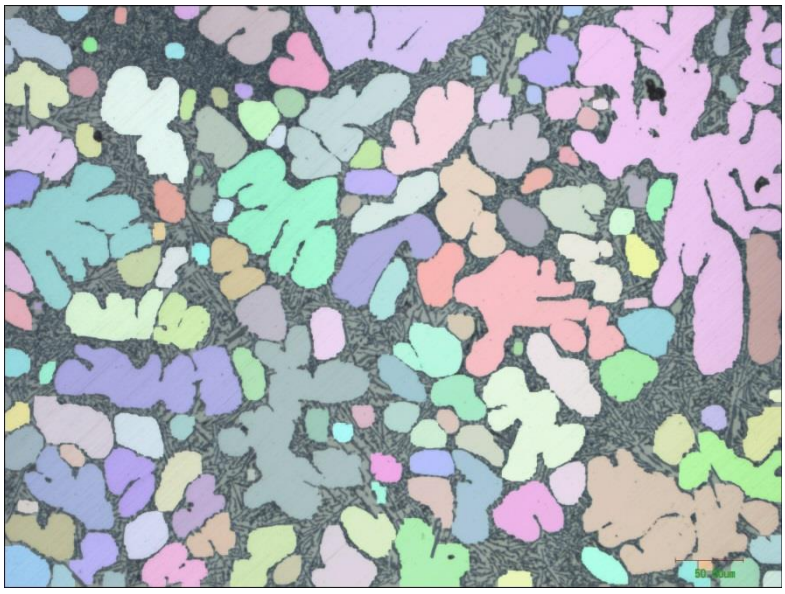

(b) Euclidean distance threshold = 0.15

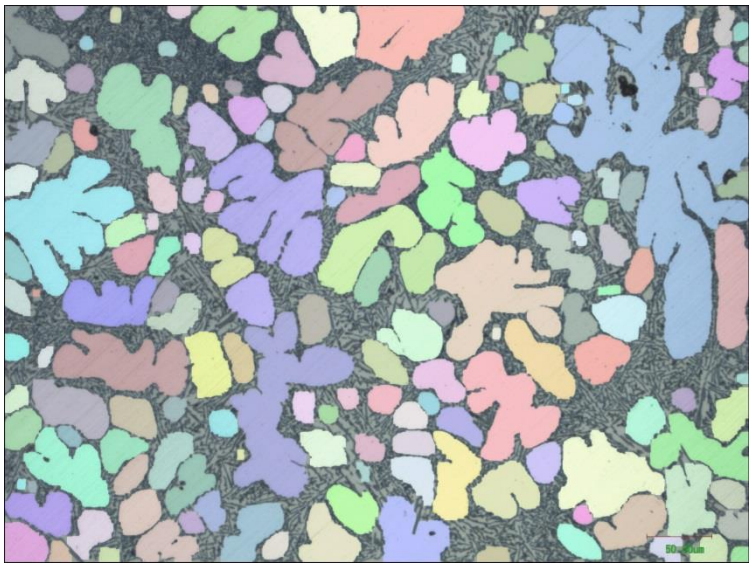

(c) Euclidean distance threshold = 0.20

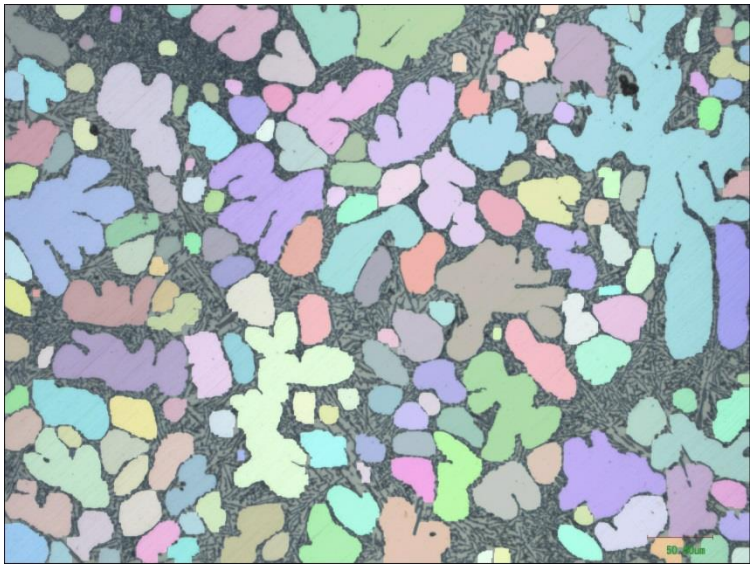

(d) Euclidean distance threshold = 0.25

Fig. 2.18 Image segmentation result using different Euclidean distance threshold. (a) Euclidean distance threshold = 0.10, (b) Euclidean distance threshold = 0.15, (c) Euclidean distance threshold = 0.20 and (d) Euclidean distance threshold = 0.25.

Fig. 2.18 shows the segmentation results using distance threshold 0.1, 0.15, 0.20 and 0.25 to prepare marker images. It can be seen that the congregated primary α-Al grains cannot be segmented when the distance threshold was small. In contrast, some large primary α-Al grains were over-segmented when the distance threshold was large.

Fig. 2.19 shows the measurement result of primary α-Al grain size distribution with different Euclidean distance threshold. Apparently, the small Euclidean distance threshold over-estimated the number of large primary α-Al grains and under-estimated those of the small ones. In contrast, large distance enlarged the measured number of small α-Al grains and under-estimated those of the large ones. When Euclidean distance threshold is 0.2, the result has best coincidence with manual result.

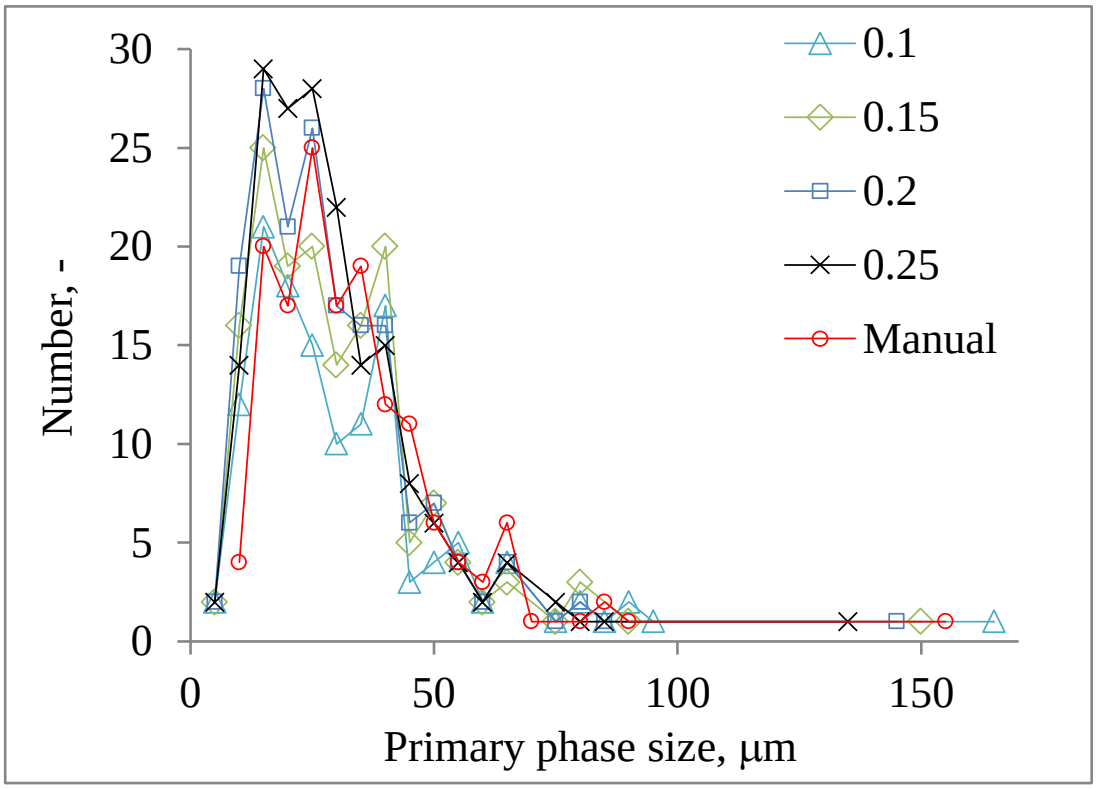

Fig. 2.19 Comparison of primary α-Al grain size distribution with different Euclidean distance threshold.

2.3.5 Image analysis procedures

The flow chart of the image pre-processing and image segmentation in the proposed method is shown in Fig. 2.20. Original image was firstly pre-preprocessed with binarization algorithm and then used to prepare another two images. One was an opening image in which eutectic grains were eliminated and the other one was an EDM image. The EMD image was subsequently used to prepare a marker-image for WST. An intersection between the result of first WST and closing image resulted in the segmentation result on the first ground. We successively implemented a second WST for the purpose of identifying small isolated primary grains. Finally, the opening image, which was used in the first WST, was utilized to intersect the result of second WST. The intersection result was the final image segmentation result. OpenCV plugged in Visual studio 2012 was used to compose the program.

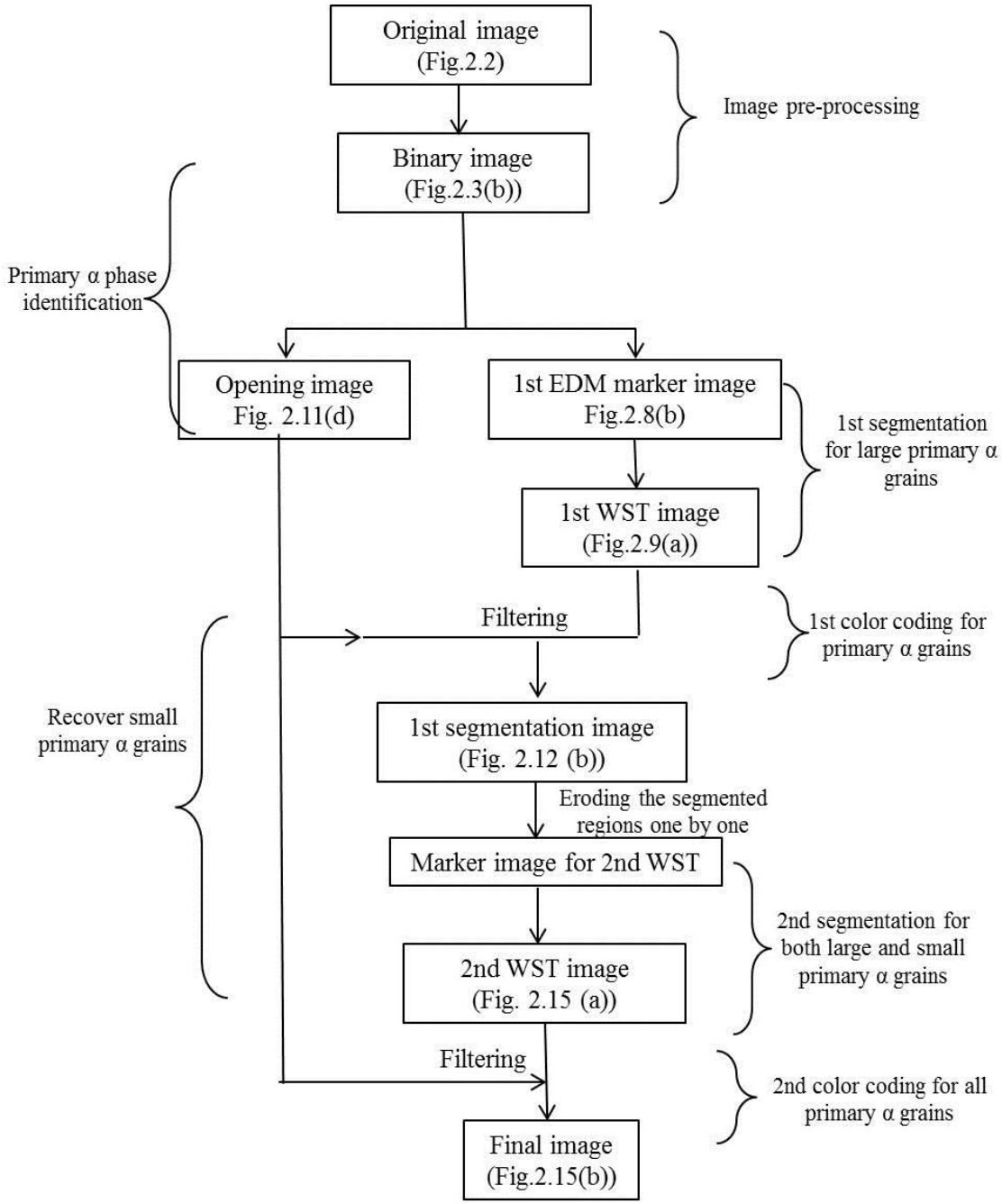

Fig. 2.20 Image analysis procedures.

2.4 Image segmentation for bad quality image and results

Image shade and artifacts are the major factors impacting image quality[21]. Fig.

2.21(a) shows an image with bad image quality taken by optical microscope. The left part of the image is much brighter than the right part. Also, noises by insufficient polishing generated during sample preparation procedure are very common on the image. When we perform binarization with a constant threshold value (T = 193) on the original image, the problem of image shade can be very clearly seen in Fig. 2.21 (b). This image shade is brought by the uneven illumination intensity. Image shade causes many details of primary grain borders disappears in the binary image. This will decrease measurement accuracy of the image analysis. Thus, we must eliminate it.

$$BTH_B = \lambda_B(f) - f \tag{2.2}$$

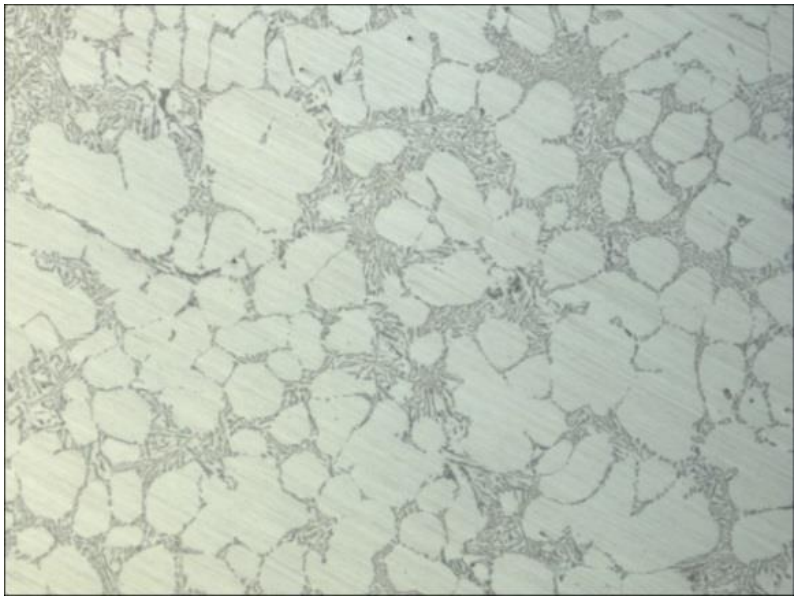

a) Original image

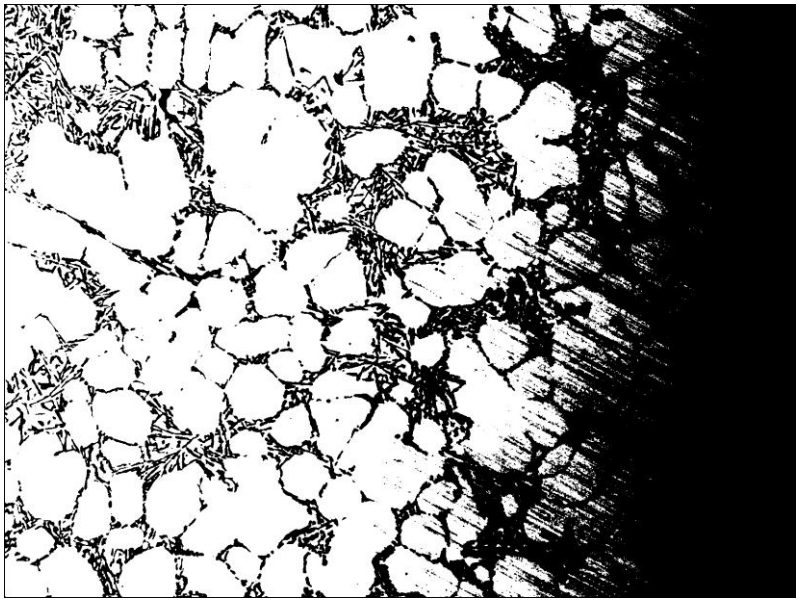

b) binarized image of a using threshold T = 193.

Fig. 2.21 Optical image of bad image quality and the binary result.

We apply Black top hat[13] (BTH) transformation to reduce image shade. BTH algorithm for a grayscale image is depicted in Eq. 2.2, where f denotes the image and $\lambda_B(f)$ indicates the closing[12] result of image f with structural element B. The deviation between the closing result and the image is defined as BTH result. In this study, the structuring element for closing was a flat square with a kernel size of 17. Too large kernel size would consume too much computation time and resource while too small size would not give pleasant result of image shade extraction. Fig. 2.22 (a) shows the BTH transformation result of Fig. 2.21 (a). To assure that the primary grains were brighter than the eutectic grains, we used a pure white image to subtract the BTH result image. Subsequently, the image contrast was enhanced by stretching[30]. Fig. 2.22 (b) shows the result after contrast enhancement. The grayscale values at the central line

were extracted and shown in the figure below. It can be observed that most of the grayscale values at the borders of the primary grains are smaller than 40. The grayscale values within primary grains distributed from 40 to 256. Thus, we manually selected T= 40 as the threshold to make binary image. Fig. 2.23 is the binarization result of Fig. 2.22 (b). There is almost no influence of image shade and there are clear borders between primary grains and eutectic grains. Moreover, the artifact noises observed in Fig. 22 (b) are also eliminated.

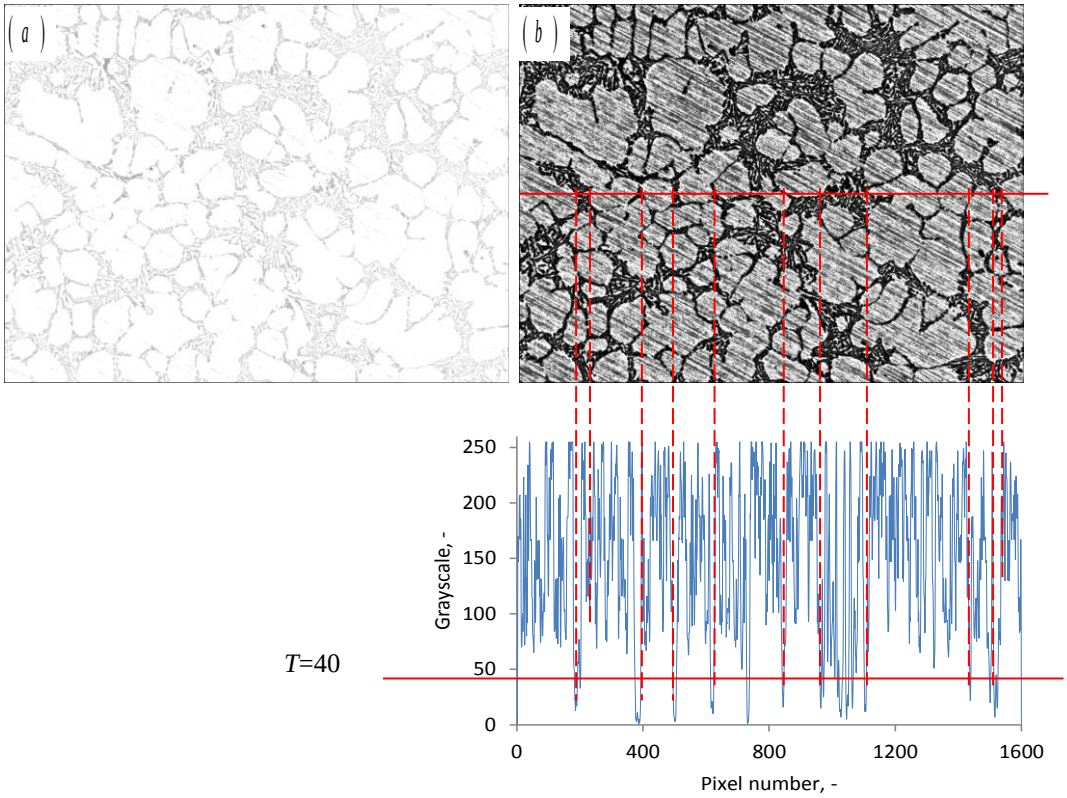

Fig.2.22 BTH transformation result and contrast enhanced result of bad quality image. The result has been inversed to make primary grains brighter than eutectic grains. a) BTH transformation result; and b) contrast enhanced result of image a, grayscale at the central line of the contrast reinforced image is shown, a threshold *T*= 40 has been selected to make binary image.

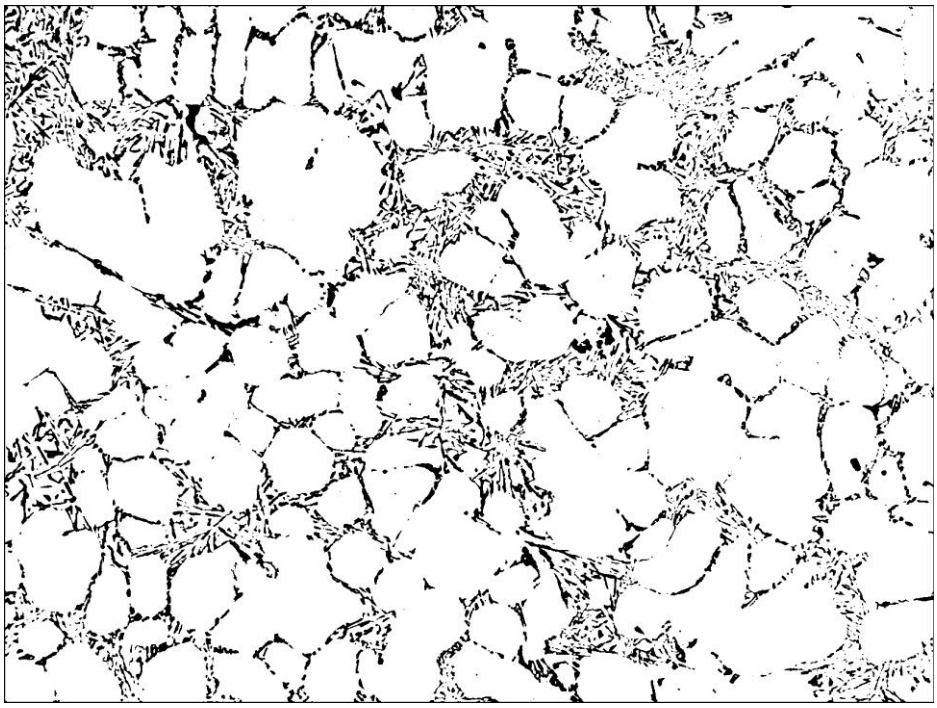

Fig. 2.23 Binarization result of Fig. 2.22 (b) with threshold *T*=40.

We performed both the conventional and proposed methods on Fig. 2.21(a) and Fig. 2.22 (a). Hence, we obtained four types of image analysis results, which are conventional method, proposed method, BTH + conventional method and BTH + proposed method. The image segmentation results of proposed method and BTH + proposed method are shown in Fig. 2.24. The proposed method without BTH made a good segmentation on the left part of the image. However, it failed to produce proper image analysis result for the right part owing to the severe image shade. A pleasant result has been observed from the result of BTH + proposed method. Most of the primary grains have been identified and there is nearly no volume contamination from the eutectic grains.

Primary grain size measurement results are shown in Fig. 2.25. The result of the

proposed method without BTH coincides with that of the manual measurement within [0μm, 30μm]. It declines largely after 30μm. The proposed method with BTH presents extremely good coincidence with the manual result. Moreover, the maximum primary grain size was successfully measured by the proposed method, no matter with or without BTH. In contrast, the implementation of conventional method, no matter on normal image or on BTH image, appears much larger difference with manual result. Still, the maximum grain size is much smaller than that in manual result. Therefore, the fusing application of proposed method highly improved the measurement accuracy and, certainly, enhanced the robustness of the proposed method.

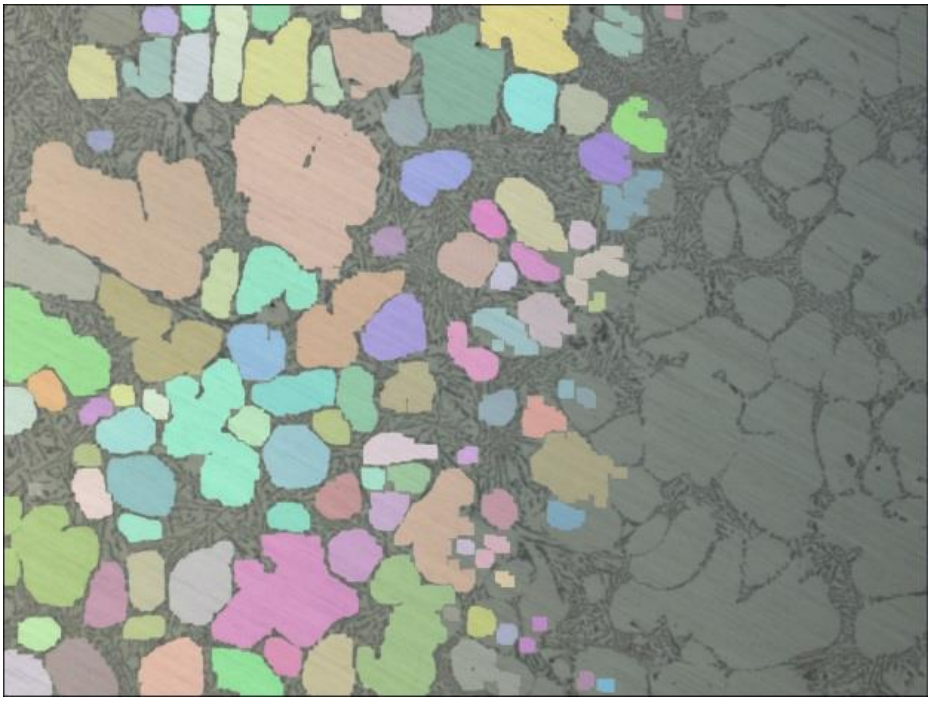

(a) Segmentation result before BTH.

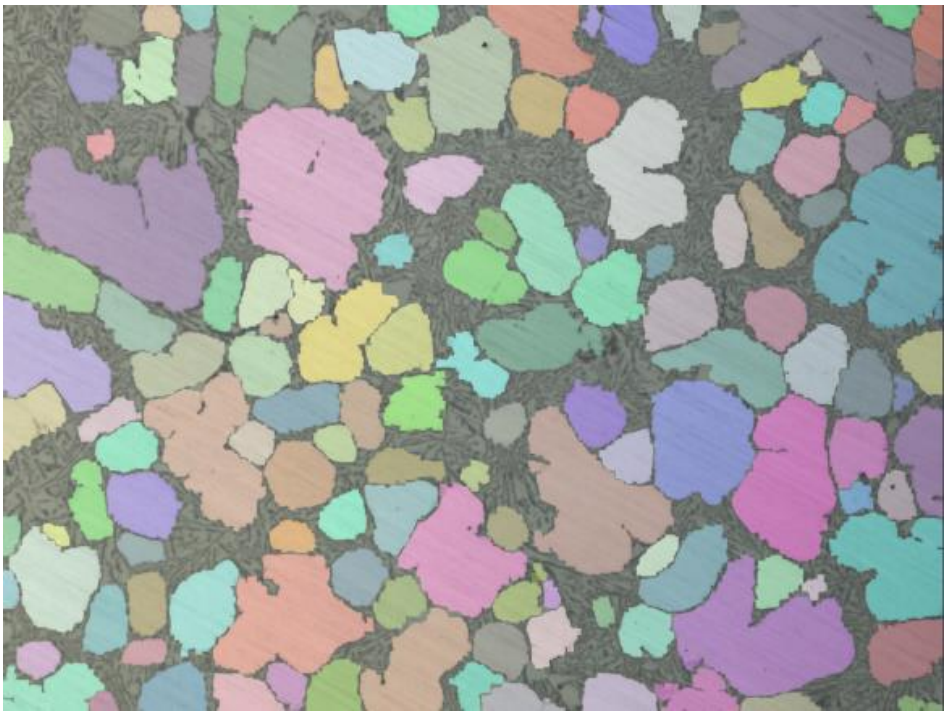

(b) Segmentation result after BTH

Fig. 2.24 Image segmentation results of bad quality image without and with shade elimination using BTH transformation. a) Proposed method, without image shade elimination, and b) proposed method, with image shade elimination.

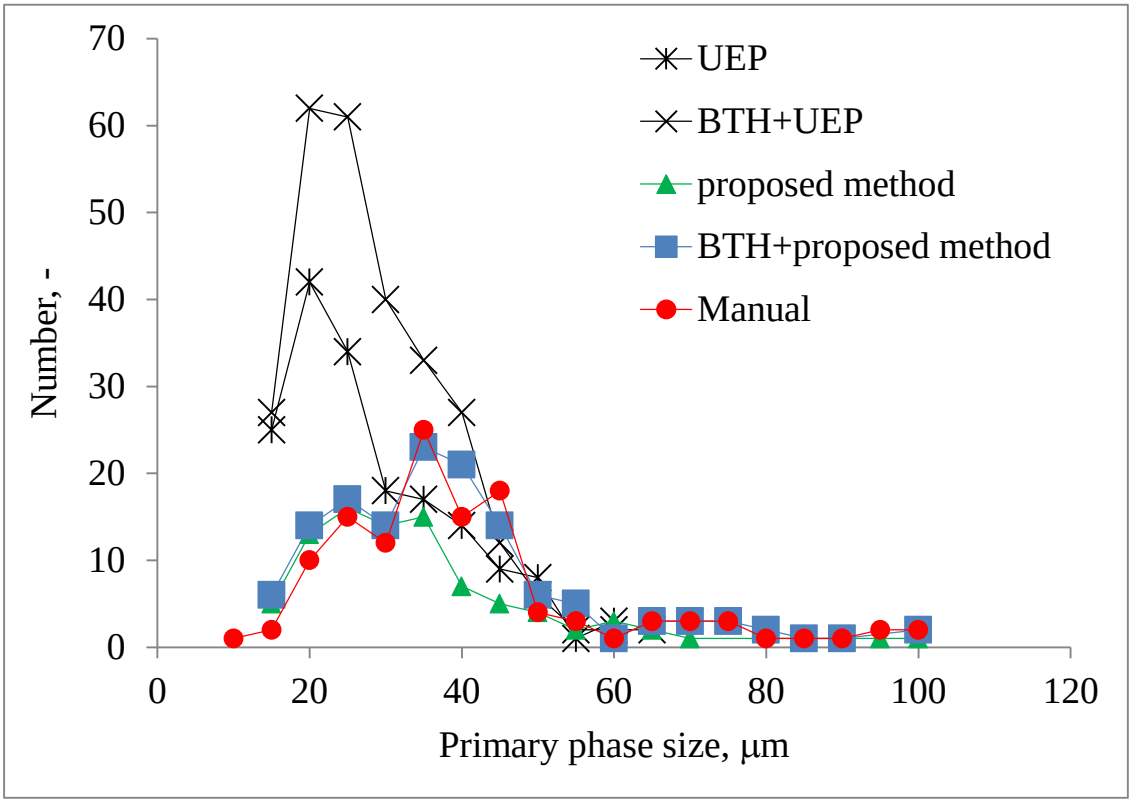

Fig.2.25 Comparison of measurement result of primary grain size with different methods on bad quality image.

2.5 Image analysis for different resolution images

Very fine primary grains may exist on the optical images. As is shown in Fig. 2.26 (a), there are many small primary grains dispersed in the intermediate region among large primary grains. This image was taken under the lens magnification of 450×. The small primary grains were so blurred and numerous that it is difficult to manually draw approximate polygons for all of them. Fig. 2.26 (b) is the region marked by red rectangle in Fig. 2.26 (a) under the lens magnification of 1000×. The small primary grains became clearer. Image segmentation with conventional and proposed methods had been performed on the area in red rectangle of Fig. 2.26 (a) as low resolution target,

and magnified image of Fig. 2.26 (b) as high resolution target to investigate the influence of lens magnification. Same to the previous section, segmented regions smaller than the minimum manual result will be deleted.

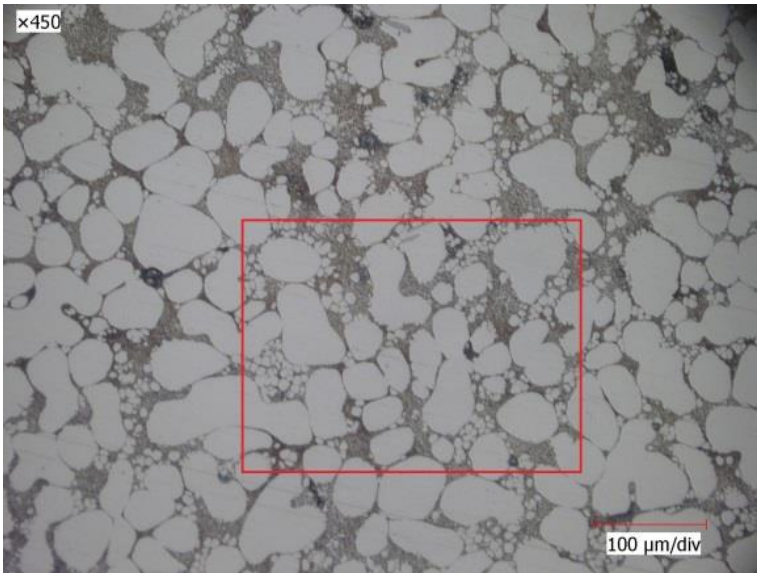

(a) Sleeve slurry microstructure at magnification of 450X

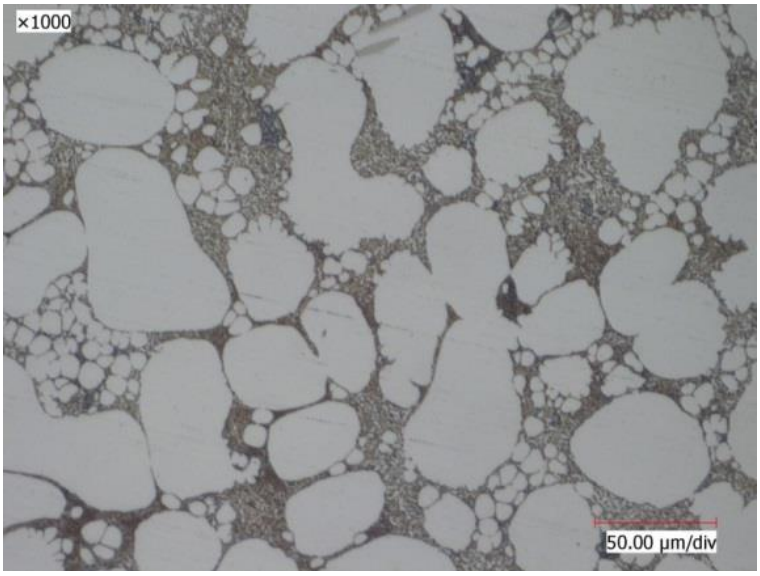

(b) sleeve slurry microstructure at magnification of 1000X

Fig. 2.26 Specimens used to investigate the influence of magnification.

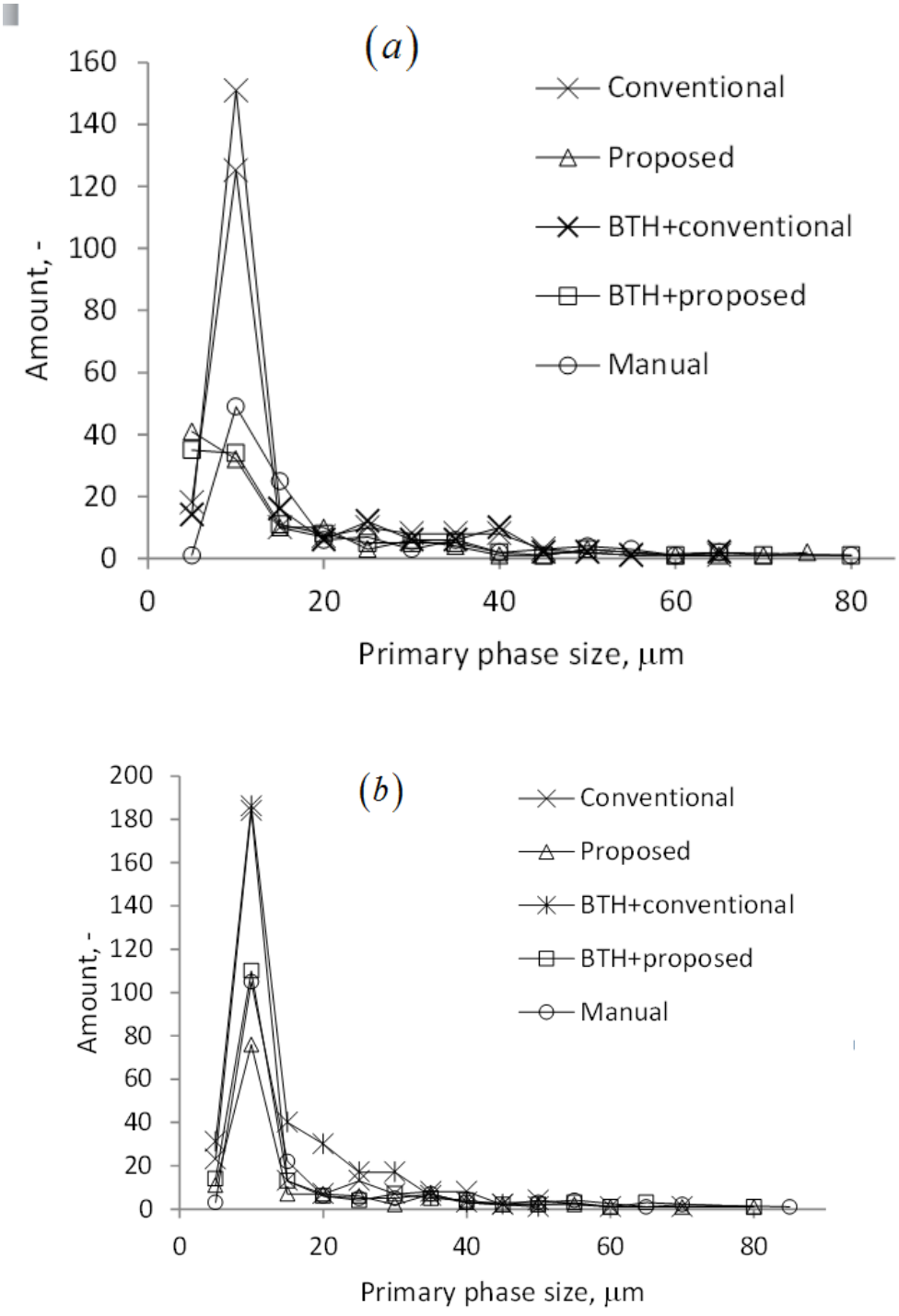

Fig. 2.27 Primary grain size distribution measurement results for different image resolutions. a) image with 450× lens magnification, b) image with 1000× lens magnification.

Fig. 2.27 shows the primary grain size measurement results by different methods. The primary α-Al grain size measurement results for the two resolution images are different. This is because the fine primary grains are too small to distinguish in Fig. 2.26 (a). Thus the total number of primary grains counted by manual method differs for the two images. We can see from the measurement results that BTH fusing proposed method gives the best results. All of the image analysis methods produced better measurement results for high resolution image than those for low resolution image.

2.6 Summary

An image analysis method for automatic primary grain size measurement of aluminum alloys. At the first step, eutectic grains were identified with opening algorithm. Next, an image segmentation using marker-image prepared with EDM method was implemented to separate individual primary grains. Eutectic grains were eliminated by intersect the image segmentation result with opening result. Finally, a second implementation of watershed transformation was conducted to segment small isolated primary grains dispersed in the eutectic grains. The results showed that the proposed method well reduced the over-segmentation, which was very common in the conventional method using UEP method to prepare marker-image. As a result, the proposed method presented much better coincidence with the manual result. Subsequently, influence of image quality was investigated using bad quality image. The results showed that the combining application of BTH transformation and proposed method generated the most decent result to the manual method. The application of proposed method without BTH on bad quality image still produced better result than the

conventional method and the conventional method with BTH transformation. Generally, the proposed method greatly improved the measuring accuracy for primary grain size in aluminum alloys. And, the fusing operation with BTH transformation improved the robustness of the proposed method to different image quality.

References

1. F. Pahlevani, Y. Endo, J. Yaokawa, M. Itamura, M. Kikuchi, O. Nagasawa and K. Anzai, in *Solid State Phenomena*, Trans Tech Publ, 2006, pp. 358-361.

2. M. Itamura, K. Anzai, N. Hirata, S. Shimaski and T. Maeda, in *Solid State Phenomena*, Trans Tech Publ, 2013, pp. 441-446.

3. M. Itamura and K. Anzai, U.S. Patent No. 9,038,705. U.S. Patent and Trademark Office, Washington DC, 2015.

4. A. Kikuchi, K. Anzai, M. Itamura, M. Kikuchi and E. Niiyama, U.S. Patent Application No. 11/596,842, 2005.

5. N. Hirata, Y. M. Zulaida, M. Itamura and K. Anzai, in *Solid State Phenomena*, Trans Tech Publ, 2013, pp. 386-391.

6. C. Yoshida, K. Kitamura, Y. Ando and K. Hironaka, *Journal of Japan Foundry Engineering Society*, 1996, **68**, 141-147.

7. A. E1382-97(2010), *Standard Test Methods for Determining Average Grain Size Using Semiautomatic and Automatic Image Analysis*, ASTM International, West Conshohocken, PA, 2010.

8. P. Das, S. Dutta and S. K. Samanta, *Proceedings of the Institution of Mechanical Engineers, Part B: Journal of Engineering Manufacture*, 2013, **227**, 1474-1483.

9. R. Qin and Z. Fan, *Materials science and technology*, 2001, **17**, 1149-1152.

10. B. Dutta, O. Pompe and M. Rettenmayr, *Materials science and technology*, 2004, **20**, 1011-1018.

11. L. Najman and H. Talbot, *Mathematical morphology*, John Wiley & Sons, 2013.

12. J. Serra, *Image analysis and mathematical morphology, v. 1*, Academic press, 1982.

13. P. Soille, *Morphological image analysis: principles and applications*, Springer Science & Business Media, 2013.

14. F.-J. Chang and C.-H. Chung, *Journal of hydrology*, 2012, **440**, 102-112.

15. M. Coster and J.-L. Chermant, *Cement and Concrete Composites*, 2001, **23**, 133-151.

16. M. E. Plissiti, C. Nikou and A. Charchanti, in *BIOSIGNALS*, 2010, pp. 284-289.

17. J. Yao, S. D. O'Connor and R. M. Summers, in *Biomedical Imaging: Nano to Macro, 2006. 3rd IEEE International Symposium on*, IEEE, 2006, pp. 390-393.

18. L. Vincent and P. Soille, *IEEE Transactions on Pattern Analysis & Machine Intelligence*, 1991, 583-598.

19. S. Eddins, *The Mathworks Journal, Matlab®, News and Notes*, 2002, 47-48.

20. S. Beucher and M. Bilodeau, in *Intelligent Vehicles' 94 Symposium, Proceedings*

of the, IEEE, 1994, pp. 296-301.

21. L. Wojnar, *Image analysis: applications in materials engineering*, Crc Press, 1998.

22. R. Al-Raoush, *Physica A: Statistical mechanics and its Applications*, 2007, **377**, 545-558.

23. T. Ferreira and W. Rasband, *ImageJ/Fiji*, 2012, **1**.

24. W. Rasband, *National Institutes of Health: Bethesda, MD, USA*, 1997, **2012**.

25. C. A. Schneider, W. S. Rasband and K. W. Eliceiri, *Nature methods*, 2012, **9**, 671-675.

26. J. Cheng and J. C. Rajapakse, *IEEE Transactions on Biomedical Engineering*, 2009, **56**, 741-748.

27. L. C. Valdés and J. V. Lorenzo-Ginori, Preceedings of Conferencia Internacional sobre Ciencia de la Computación e Informática CICCI 2011.

28. I. Pitas, *Digital image processing algorithms and applications*, John Wiley & Sons, 2000.

29. X. Yang, H. Li and X. Zhou, *IEEE Transactions on Circuits and Systems I: Regular Papers*, 2006, **53**, 2405-2414.

30. R. C. Gonzalez and R. E. Woods, *Digital Image Processing*, Pearson/Prentice Hall, 2008.

Chapter 3. Image analysis for bended long-striped bi-phase microstructure based on mathematical morphology and its application on metal-ceramic composite

3.1 Introduction

Composites were reported to oppose high mechanical performance[1, 2]. Metal-ceramic composite was one of such a compound which appeared high mechanical performance and comparable electrical performance with metals[3]. The metal-ceramic composite possesses excellent mechanical properties in contrast to the mono metal or ceramic materials, which either have relatively low strength and low wear resistance or are brittle. Recently, a composite composed of long-stripped metal particles in glass matrix has been reported[3]. It performed excellent mechanical performance under high temperature and showed comparable electrical resistivity to metal materials. Usually, the volume fraction is the commonly used factor to evaluate the potential electrical

performance[4, 5]. Recent research showed that metal particle shape also had significant impact[3, 6-8]. Aspect ratio is a commonly used parameter to characterize particle shape in composite[9]. Fig. 3.1 shows the mechanism of measuring particle aspect ratio. It is the ratio of major and minor axis of a particle. It was reported that metal-ceramic composite with high metal particle aspect ratio performed high electrical conductivity[3].

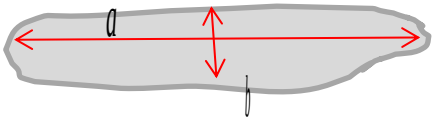

Fig. 3.1 Illustration of metal particle aspect ratio.

The evaluation of aspect ratio is important for evaluation of metal particle elongation during the milling procedure. The elongation of metal particle enhanced the conductivity of the composite[6]. The aspect ratio could be manually measured by measuring major axis length and minor axis length, respectively. It yielded accurate result of aspect ratio. However, it is tedious and labor-intensive to repeatedly measure major and minor axis for every metal particles.

Image processing techniques have been applied to improve the evaluation efficiency. The metal particles were firstly automatically segmented from the matrix and neighboring metal particles and then ware fitted with ellipses[3]. The major and minor axis of the metal particles were approximated with those of the fit ellipse[10]. The accuracy of the image processing method greatly relied on the image segmentation result. The conventional image segmentation method in imageJ software produced too much over-segmentation. The metal particles were mistakenly over-segmented into

many small regions. This made the segmented result of metal particles smaller than the actual particles. As a result, the aspect ratio of metal particles was under-estimated. In addition, the fit ellipse method found difficulties in yielding good evaluation of aspect ratio for bended shapes. It would under-estimate the major axis length and over-estimate the minor axis length for the bended metal particles.

Watershed transformation with manually drawn markers is reported to be able to segment complex situations in an image[11]. In this chapter, we applied manually drawn markers to indicate the individual metal particles so as to reduce over-segmentation of metal particles by conventional image segmentation method. In addition, the evaluation method for aspect ratio by image analysis has also been improved to yield good result for both straight and bended metal particles.

3.2 Specimen preparation

In this study, soda-lime glass powder (average particle radius is 14μm) is used as the matrix while the mixed Ni-Cr particle (Ni 77.5%, Cr 20%, Si 1%, Mn 0.8%, Fe 0.5%, C 0.2%) is used as the conductive filler. Firstly, a mixture of the two powders, weighted 50g, was obtained with the volume fraction of Ni-Cr powder is 30%. Secondly, the mixture was milled with 500g Si3N4 balls and 150ml ethanol in a planetary ball mill machine. Different milling time (2h~10h) is applied in order to get samples filled by metal particles of different aspect ratio. After ball milling, the ethanol was eliminated in an evaporator so as to obtain the dry mixture which was electrically sintered subsequently (sintering circumstance, pressure 38MPa, temperature 700 ℃, time 5min).

Two samples (size, 10ϕ×1.5mm) were sintered, one of which was used to test the electric resistance and the other one was used to investigate the microstructure. The samples were cut off, embedded in resin and grinded to take the microscopic images of the microstructure.

3.3 Conventional aspect ratio evaluation methods

3.3.1 Manual method

Manual measurement is the commonly used method to measure metal particle aspect ratio. As is illustrated in Fig. 3.2, there are two kinds of metal particles in a metal-ceramic composite micrograph. The first one is straight strip and the other one is bended strip. A straight line connecting the farthest two pixels in the former strip (upper figure in Fig. 3.2) and a polyline fitting farthest routine in the latter strip (downer figure in Fig. 3.2) were used to measure major axis. The minor axis length was the largest thickness of the strips. In this chapter, manual measurement is taken as the most accurate result. The merit of manual method is that it could yield accurate result of the metal particle aspect ratio. However, it calls for high labor-intensity and large time-consumption.

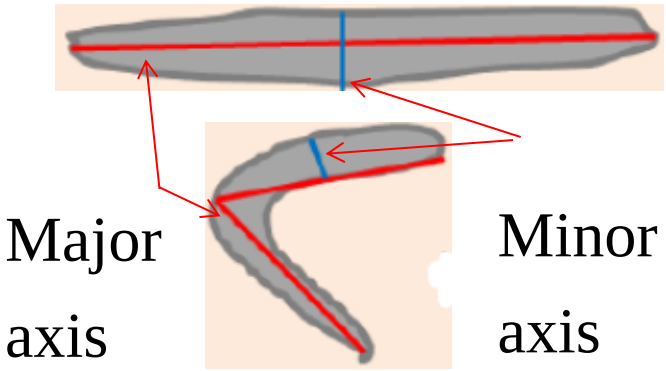

Fig. 3.2 Schematic for manual measurement of metal particle aspect ratio.

3.3.2 Image processing method

A typical image processing procedure comprises of four steps, which are image acquisition, image pre-processing, image segmentation and data measurement. Image acquisition has already been shown in section 3.2. The image pre-processing for the aspect ratio measurement of metal particles is simple. The metal particles are white and the glass matrix is black in the optical image of metal-ceramic composite microstructure. It can be seen in Fig. 3.3(a). A simple binarization operation will identified the metal particles from the matrix. Fig. 3.3(b) shows the binary result of a micrograph. This method fulfilled the identification of metal particles and the glass matrix. However, the congregated particles had not been separated. This will lead to the mistakes in the aspect ratio estimation of metal particles. The next steps are to segment individual metal-particle and to evaluate the major and minor axis. The conventional methods of the two steps are as follows.

(a) Original compound image

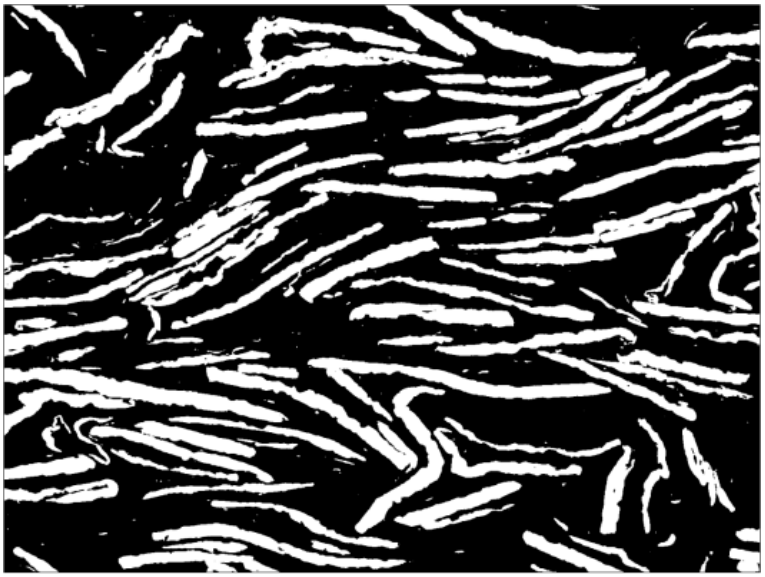

(b) binary image

Fig. 3.3 Image binarization result. a) original image and b) binary image.

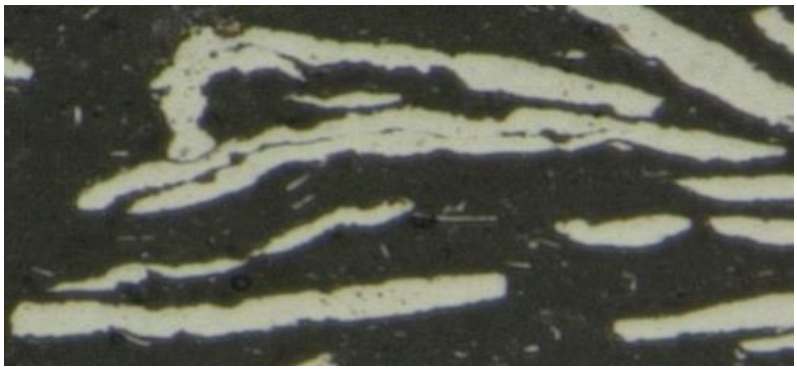

(a) part of original image in Fig. 3.3 (a)

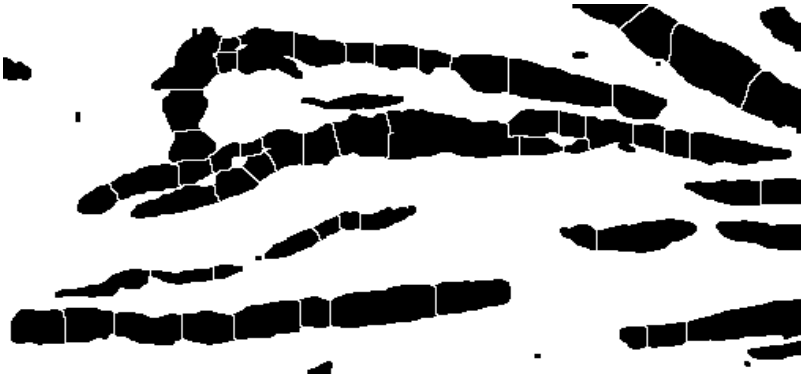

(b) WST with UEP markder

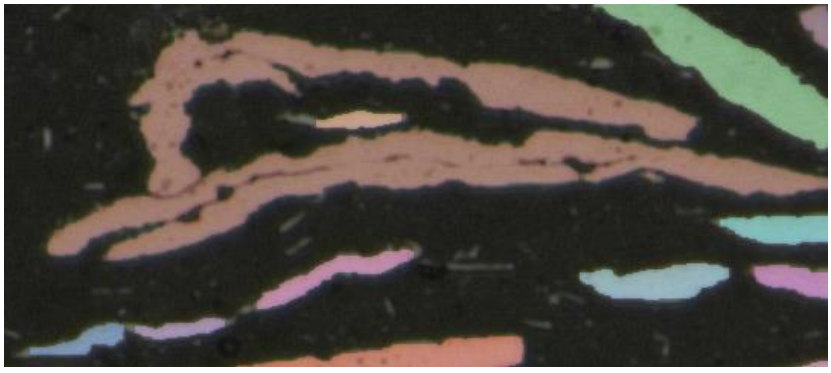

(c) segmentation result using shape marker from EDM.

Fig. 3.4 Image segmentation for part of original image in Fig. 3.3. a) original image, b) result of WST with UEP markers and c) image segmentation result using markers prepared by thresholding Euclidean distance map.

3.3.2.1 Image segmentation

Watershed transformation is the most commonly used algorithm to segment congregated grains or particles in an image[12]. Usually, the marker-controlled watershed is used to suppress the generation of over-segmentation. Local Euclidean distance maxima (same to Ultimate eroding point (UEP)) method and shape marker (by thresholding Euclidean distance map, shorten as EDM method) method are the two commonly used methods to automatically or semi-automatically prepare markers for watershed transformation. Fig. 3.4 shows the implementation results of the two methods on part of Fig. 3.3 image. Watershed transformation results with local Euclidean distance maxima (same to UEP) markers and with markers prepared by thresholding Euclidean distance map are shown in Fig. 3.4(b) and Fig. 3.4(c), respectively. Unfortunately, the metal particles were over-segmented into small regions in Fig. 3.4 (b) and under-segmented (metal particles were not segmented) in Fig. 3.4(c).

3.3.2.2 Fit ellipse method

Major and minor axis of a metal particle should be estimated after the individual metal particles have been segmented. Fit ellipse is one of the most commonly used methods. Fig. 3.5 shows the fit ellipse[10, 13, 14] method for straight and bended stripped particles. An ellipse is used to fit the contour of the metal particle. The major axis and minor axis of the ellipse are taken as the major axis and minor axis of the particle. One of the disadvantages of this method is that the major axis length of the fit ellipse for

bended-stripped particles becomes smaller than the real major axis and the minor axis length becomes larger. As a result, the aspect ratio of the bended stripped particles will be under-estimated. It can be seen in the right image of Fig. 3.5.

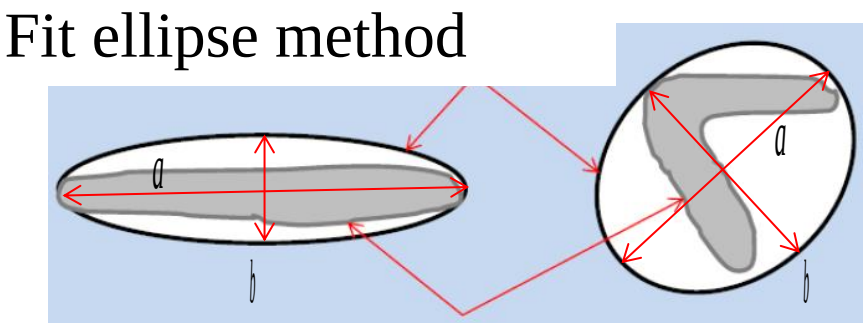

Fig. 3.5 Schematic for metal particle aspect ratio with fit ellipse method.

(a) Fit ellipses for binarization result

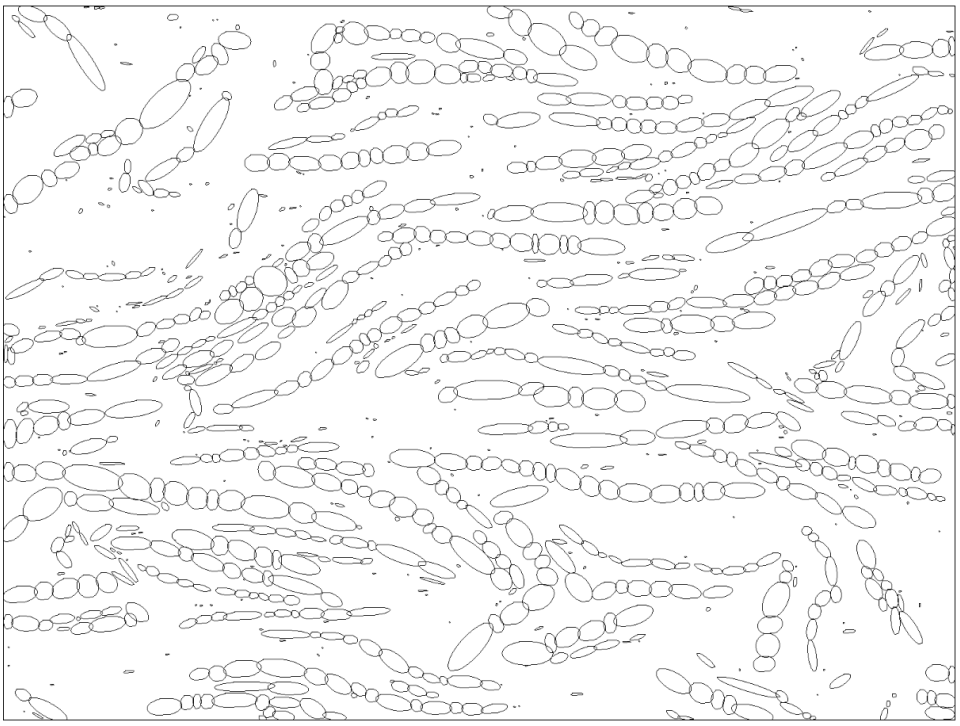

(b) Fit ellipse for WST result with UEP method

Fig. 3.6 Conventional metal particle aspect ratio measurement with fit ellipse method in ImageJ.

Fit ellipse method had been implemented on the results of binaryzation result and the UEP+WST method. Fig. 3.6 shows the implementation of fit ellipse method on the result of binaryzation result and the watershed transformation (WST) with UEP method. The border particles have been eliminated. It can be seen that before the WST, many particles congregated and were not segmented. The fit ellipses were calculated according to the region of congregated particles. The watershed transformation with UEP method made the situation worse. Congregated particles were over-segmented into many small regions. This situation was reflected in the final aspect ratio measurement results, which were shown in Tab. 3.1. Obviously, the aspect ratio of fit ellipse method

directly on binarization image has been under-estimated in contrast to manual result. However, the watershed transformation with UEP markers achieved an even smaller aspect ratio owing to the severe over-segmentation. The fit ellipse method was also implemented on the result of watershed transformation with markers by thresholding EDM.

Table 3.1 Aspect ratio evaluation result with different methods.

Methods	Manual	Binaryzation+ Fit Ellipse	UEP+WST+ Fit Ellipse	EDM+WST+ Fit Ellipse
Aspect ratio	13.41	8.28	2.23	7.92

3.4 Improvement of the image segmentation

Generally, the conventional image processing methods failed to give an accurate evaluation of the aspect ratio. A better image processing method is desirable. It involves of two aspects of improvement. Firstly, the image segmentation method should be improved so that the image would not be over-segmented or under-segmented. Secondly, particle major and minor axis estimation method should also be improved.

The automatic preparation of marker image with UEP method leads to over-segmentation for metal-ceramic micrographs and that with EDM method leads to under-estimation. Thus, a manual marker[11] preparation method was used in this chapter.

Fig. 3.7(a) shows the manual preparation of marker-image for Fig. 3.4 (a). Markers are used to indicate both metal particles and glass matrix. Fig. 3.7 (b) shows the segmentation results. Those glass matrix regions were deleted from the final segmentation results. It can be seen that this segmentation result is much better than the automatic preparation marker methods in Fig. 3.4.

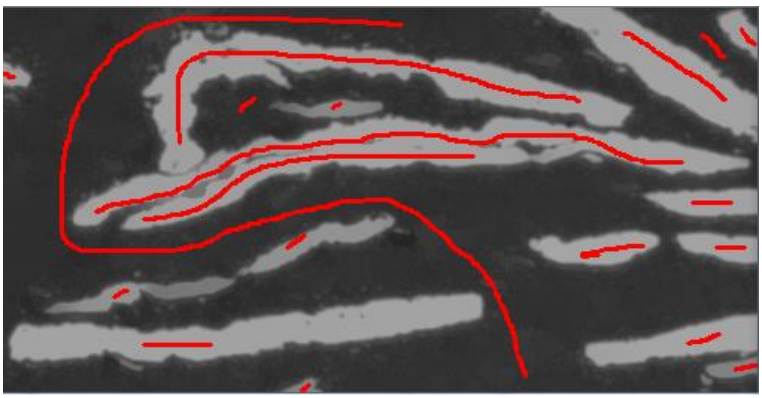

(a) manually drawn marker-image.

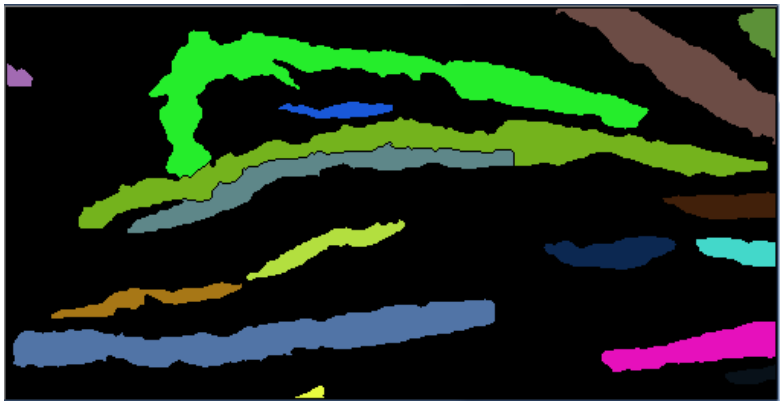

(b) WST result with manually drawn marker-image.

Fig. 3.7 Metal particle segmentation with watershed transformation. a) manually drawn marker-image, b) WST result with manually drawn marker-image.

Fig. 3.8 (a) shows the metal particle segmentation results for the whole original metal-ceramic micrograph. The edge particles had been removed from the segmentation result to reduce their influence on the evaluation result. Apparently, the segmentation result has no over-segmentation and no under-estimation. Fig. 3.8 (b) shows the fit ellipse result of the individual metal particles. The green boxes are the convex rectangles of the particles. The yellow curves are the metal particle boundaries. The pink ellipses are the calculated fit ellipses for the metal particles. The aspect ratio result evaluated with fit ellipse method on the individual metal particle image is 8.29. It still has large error with manual result. Thus, we must improve the aspect ratio evaluation method.

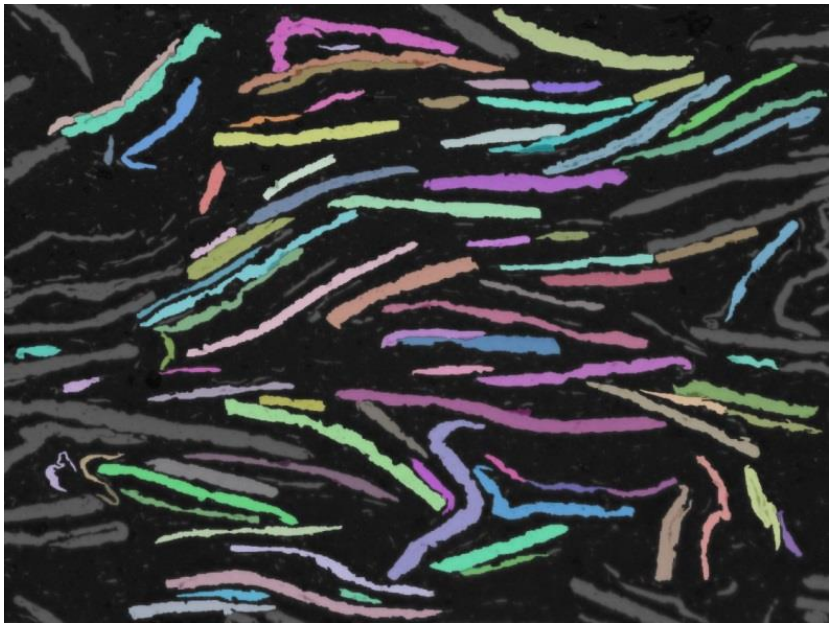

(a) Image segmentation result with manual marker-image.

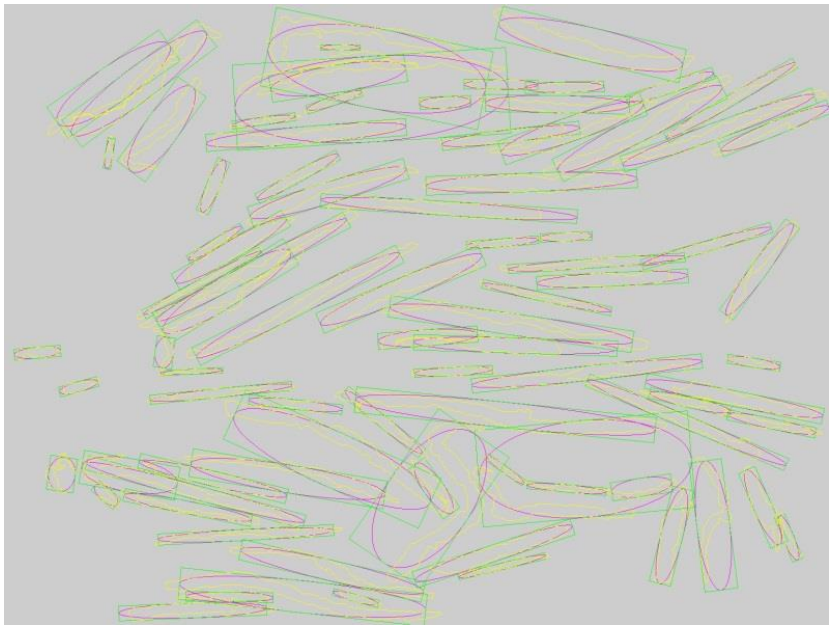

(b) Fit ellipse result of the segmentation result.

Fig. 3.8 Image segmentation result of Fig. 3.3 (a) with hand drawn markers and (b) fit ellipse of the individual metal particles.

3.5 Improvement of the aspect ratio evaluation method

In order to improve the aspect ratio evaluation method, we proposed two kinds of methods to overcome the shorthand of fit ellipse method.

3.5.1 Maximum inscribed circle method

Fig. 3.9 illustrates the aspect ratio of a metal particle s. Here, l is the major axis of this particle. Suppose the l is equally divided into N parts ($N \to \infty$), then l can be calculated using:

$$l = \sum_{i=0}^{N} l_i \tag{3.1}$$

The thickness of the metal particle at i th part is defined as d_i. The area of the metal particle can be depicted as

$$S_S = \sum_{i=0}^{N} l_i d_i = l d_{mean} \tag{3.2}$$

Here, d_{mean} is the mean thickness of the metal particle along the major axis. c is the maximum inscribed circle (MIC) in the metal particle and its diameter is d_{MIC}.

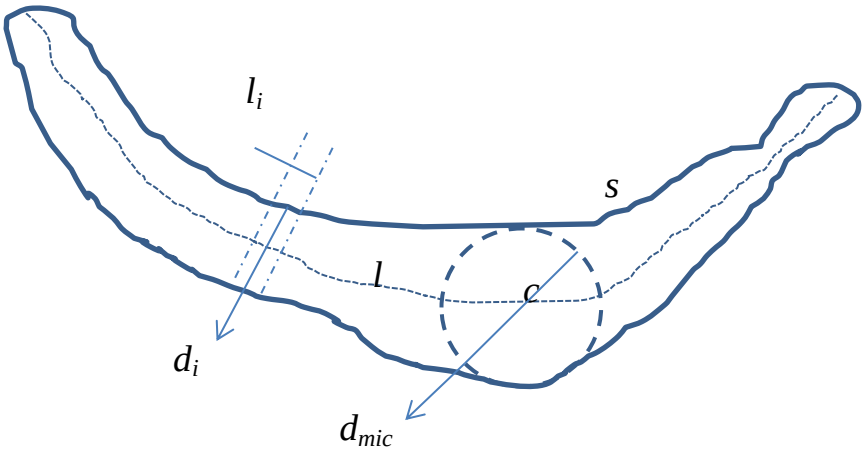

Fig. 3.9 Schematic of aspect ratio measurement.

If we define the aspect ratio is the ratio between major axis length and minor axis length and the minor axis length is the maximum inscribed circle diameter, we can derive Eq. 3.3.

$$AR = \frac{l}{d_{MIC}} = \frac{\pi l d_{MIC}}{\pi d_{MIC}^2} = \frac{\pi l d_{MIC}}{4 S_{MIC}} = \frac{\pi d_{MIC}}{4 d_{mean}} \bullet \frac{S_S}{S_{MIC}} \tag{3.3}$$

For a long strip shape, $\frac{4 d_{mean}}{\pi d_{MIC}} \approx 1$, then the ratio between the two areas can be

assumed as the aspect ratio.

3.5.1.1 Verification with manually drawn images

Fig. 3. 10 shows 4 types of shapes to testify the accuracy of maximum inscribed circle method. The maximum inscribed circle results is shown in Fig. 3.11. Fig. 3.12 shows the calculation result of aspect ratio by maximum inscribed circle method, fit ellipse method and manual method. It can be seen that both the maximum inscribed circle method and fit ellipse method yielded exact result with manual result for ellipses. For rectangle shapes, both of the two methods show error with manual result. However, the maximum inscribed circle method is more accurate. In fact, there is a systematic error for maximum inscribed circle method when evaluating the aspect ratio of rectangles. As the average thickness of rectangles are equal to d_{MIC}, which means $\frac{4d_{mean}}{\pi d_{MIC}} \approx \frac{4}{\pi}$. i.e. Aspect ratio evaluated with MIC method for rectangles is always 30% larger than the real value. For the straight strips, the both of the two methods yielded accurate result to the manual result. However, the maximum inscribed circle method appeared larger error for N0. 7 and No. 8 particles. This is because the thickness of the two particles is homogeneous. Thus, they are more rectangle-like than the other particles. As is depicted, the MIC method has systematic error for rectangle-like shapes. The fit ellipse method shows very good accuracy for straight stripped particles. For the bended strips, the maximum inscribed circle method produced very close result to the manual result. In contrast, the fit ellipse method showed very large error. Generally, the MIC method works well for different shapes while the fit ellipse method confronts limitation for the bended stripped particles. Although there is systematic error for

rectangle-like shapes, the MIC method still shows better effectiveness for different shapes.

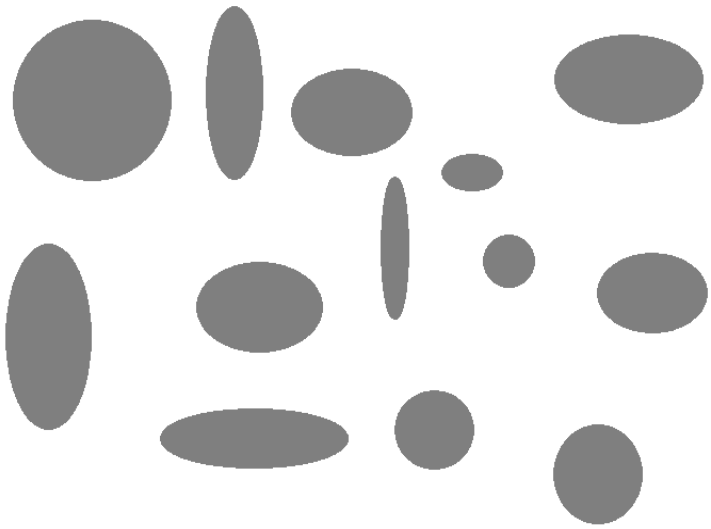

(a) Ellipse

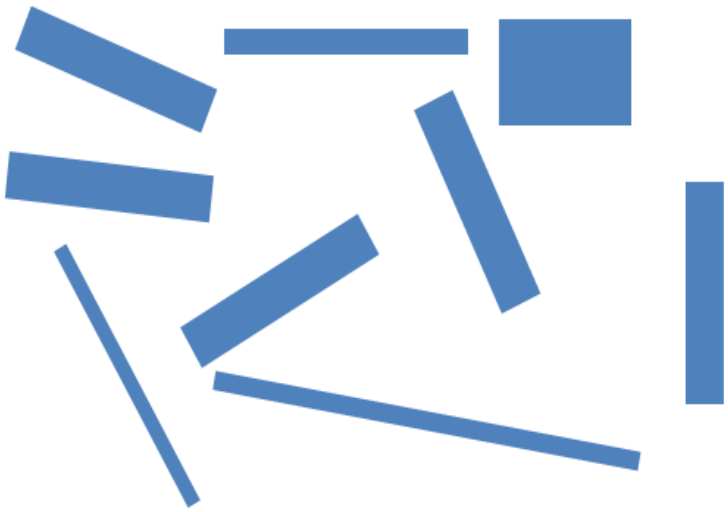

(b) Rectangle

(c) Strips

(d) Bended strips

Fig. 3.10 Hand-drawn shapes to verify maximum inscribed circle area method.

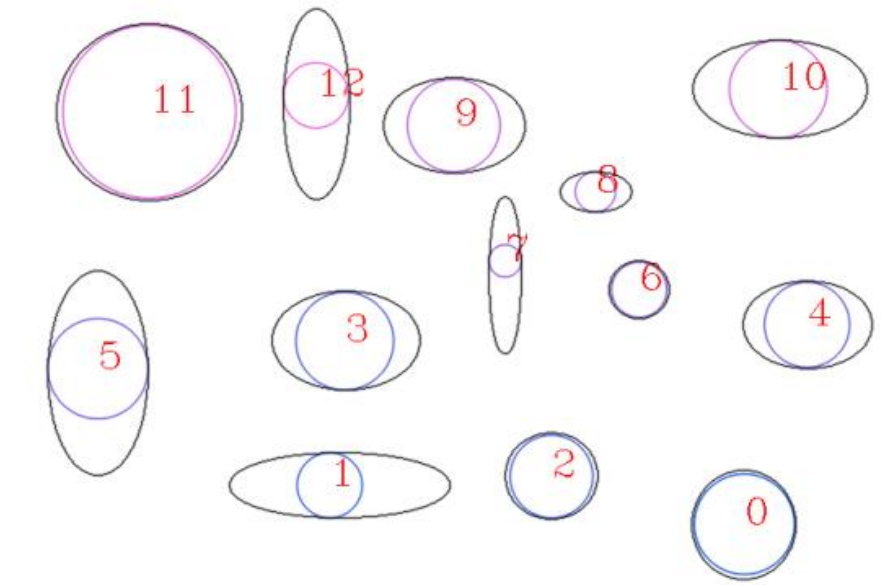

(a) Ellipse

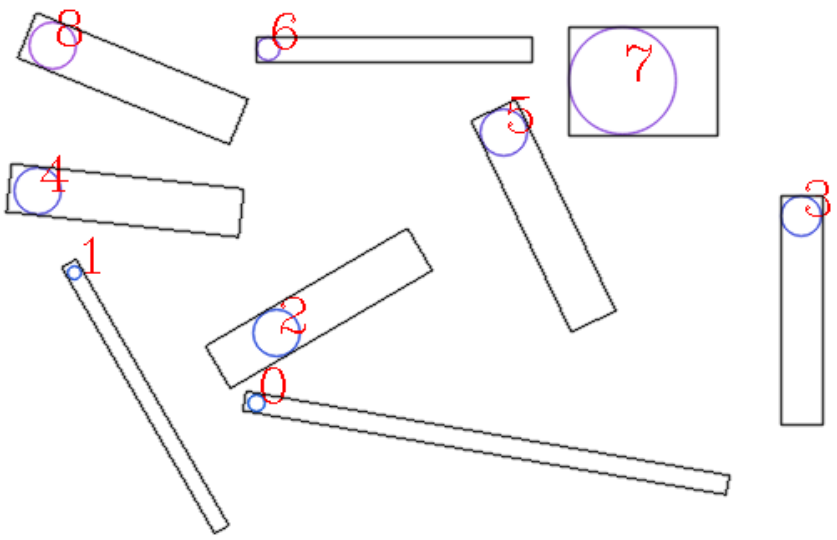

(b) Rectangle

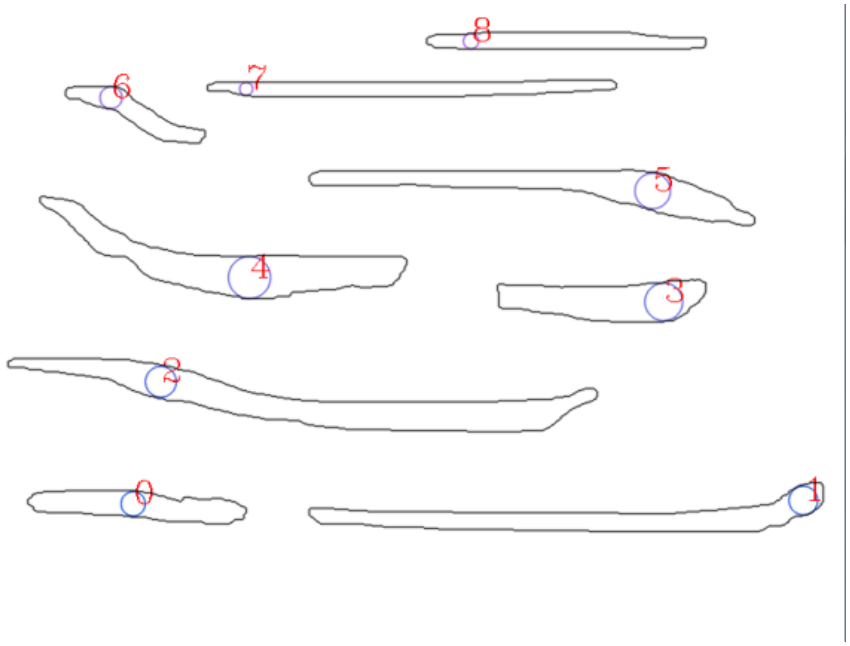

(c) Strips

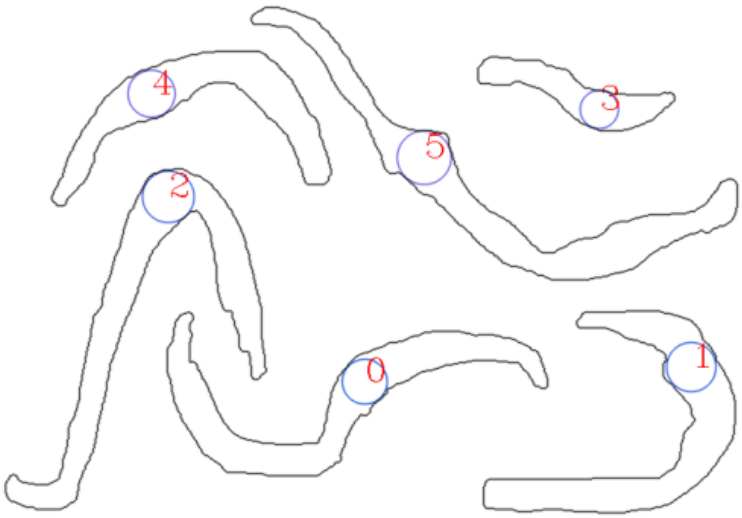

(d) Bended strips

Fig. 3.11 Maximum inscribed circle calculation results.

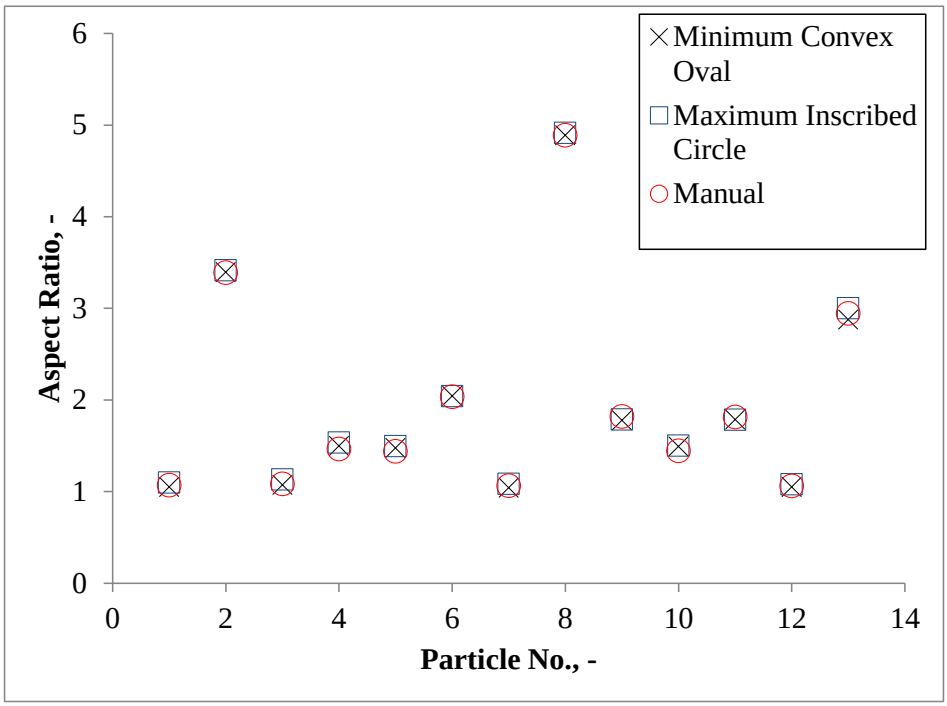

(a) Ellipse

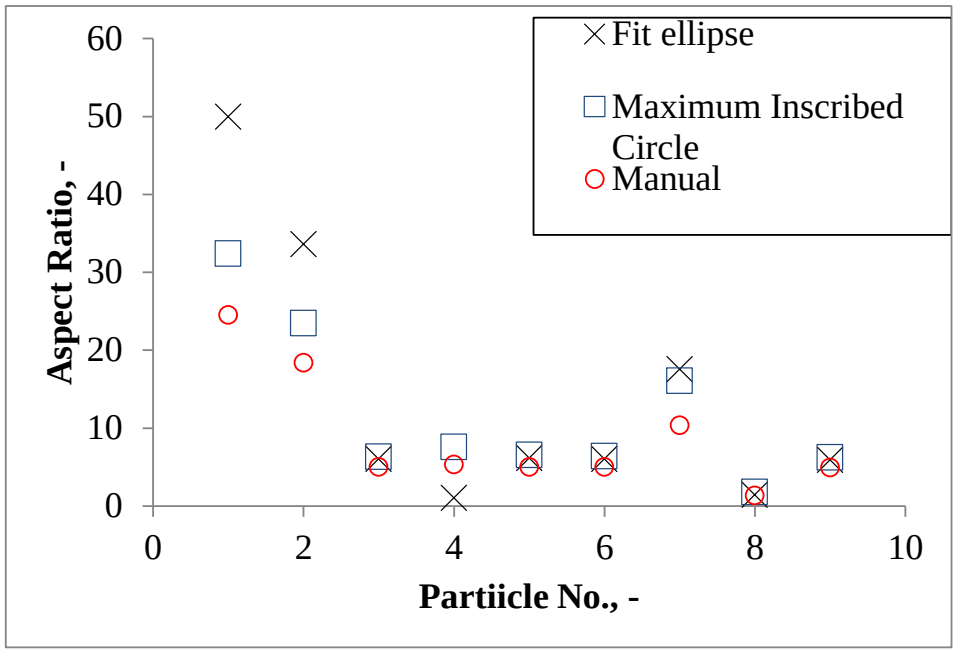

(b) Rectangle

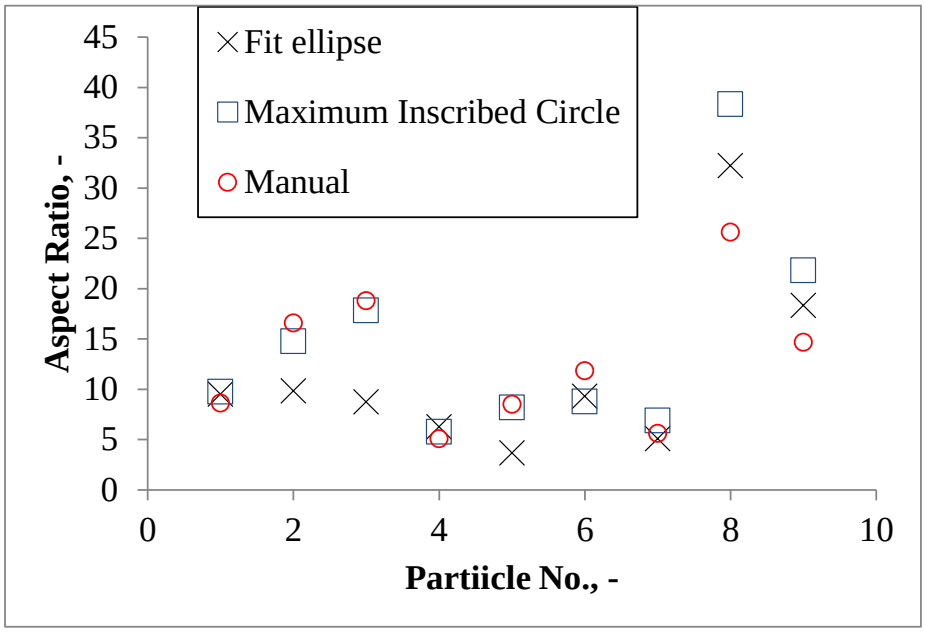

(c) Strips

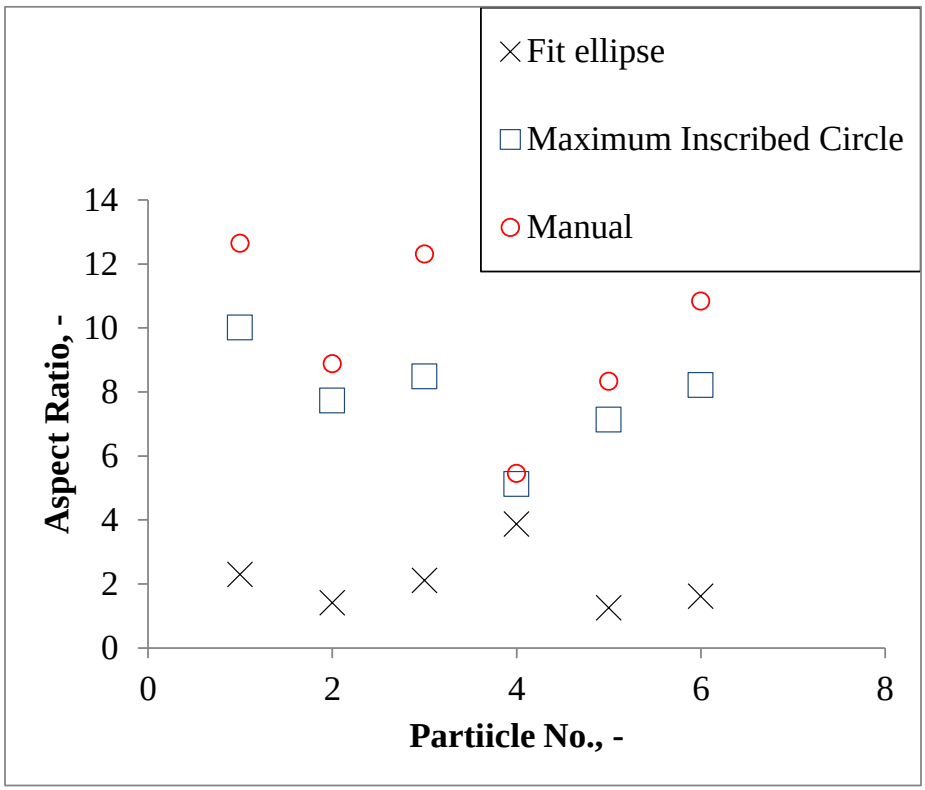

(d) Bended strips

Fig. 3.12 Comparison of aspect ratio result with fit ellipse method and MIC method.

3.5.1.2 Application of maximum inscribed circle method to actual image

The maximum inscribed circle method has been applied to the actual images. The original images are taken from samples manufactured under same rotation speed but different milling time. Fig. 3.13 (a), Fig. 3.14 (a) and Fig. 3.15 (a) show the original image obtained by milling time 2h, 4.5h and 10h, respectively. Apparently, the aspect ratio became larger when the milling time grew up. Fig. 3.13 (b), Fig. 3.14 (b) and Fig. 3.15 (b) show the image segmentation result with manually drawn markers. The metal particles were well segmented. Fig. 3.13 (c), Fig. 3.14 (c) and Fig. 3.15 (c) are the fit ellipse calculation results, in which the green, yellow and pink curves or shapes are the metal particle boundaries, convex rectangle and fit ellipses, respectively. Fig. 3.13 (d), Fig. 3.14 (d) and Fig. 3.15 (d) are the maximum inscribed circle calculation results. In fact, we also measured the aspect ratio by calculating the fit ellipses on the binary image using ImageJ. The comparison of aspect ratio by different methods is shown in Fig. 3. 16. The aspect ratio of the metal particles increases with the milling time. The maximum inscribed circle method yielded close result to fit ellipse method when the milling time is short, but became much larger than the fit ellipse method when the milling time grew up. The fit ellipse result that produced by the program in this chapter is larger than that produced by ImageJ software. There are two reasons contributed to this difference. Firstly, the binary image used to calculate fit ellipses with imageJ contains many tiny metal particles. These particles are not considered in the fit ellipse calculation in the program of this study, but are calculated by imageJ. Secondly, the metal particles are not well segmented in the binary image.

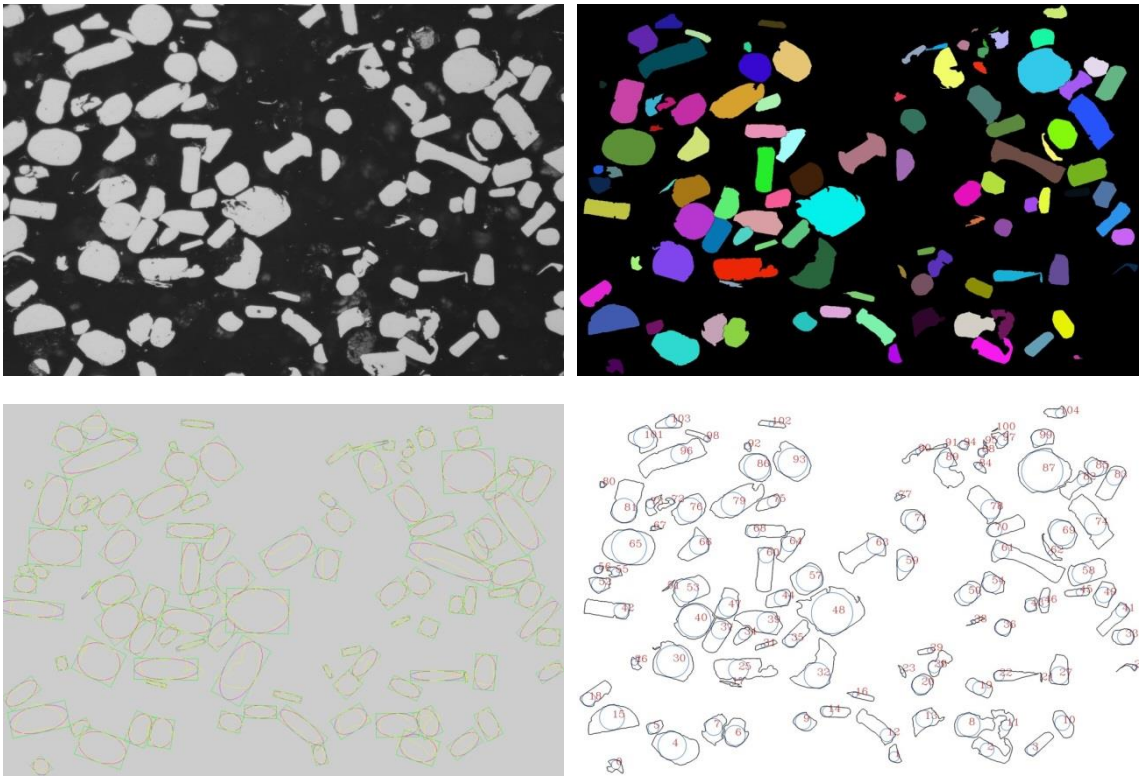

Fig. 3.13 Aspect ratio measurement with maximum inscribed circle method for the sample achieved under condition: milling time 2h, rotation speed 309rpm. (a) original image, (b) metal particle segmentation result, (c) Fit ellipse calculation and (d) maximum inscribed circle result.

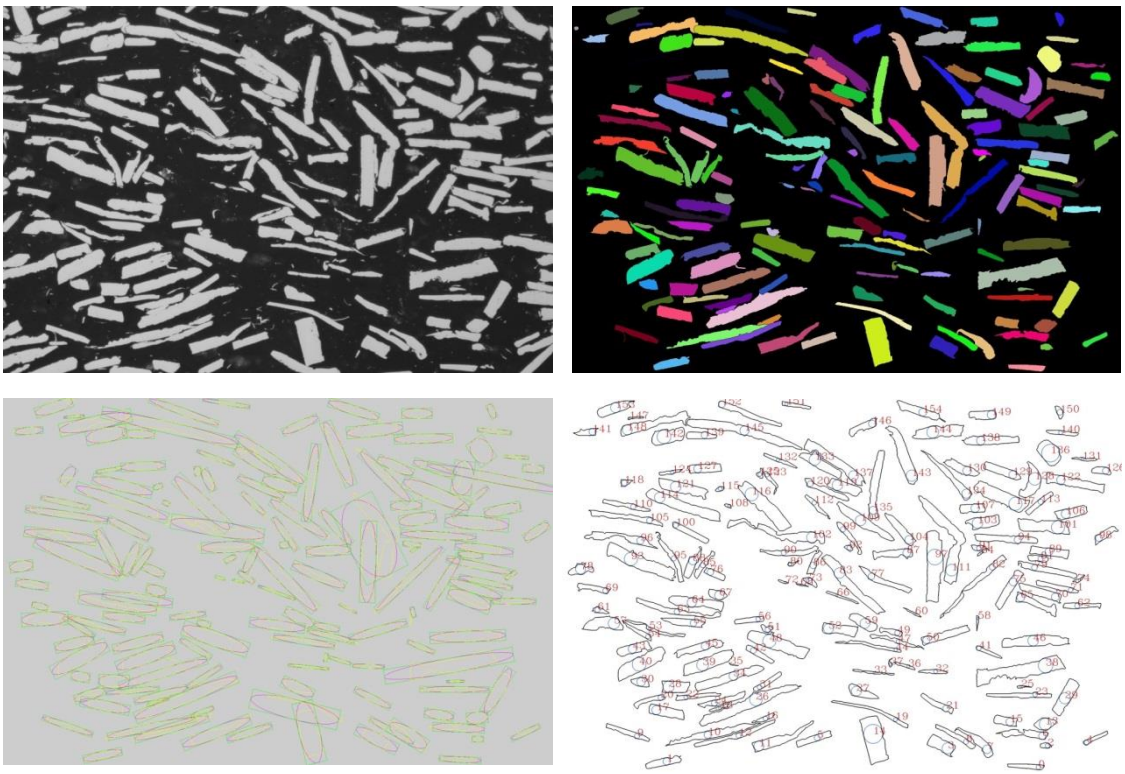

Fig. 3.14 Aspect ratio measurement with maximum inscribed circle method for the sample achieved under condition: milling time 4.5h, rotation speed 309rpm. (a) original image, (b) metal particle segmentation result, (c) Fit ellipse calculation and (d) maximum inscribed circle result.

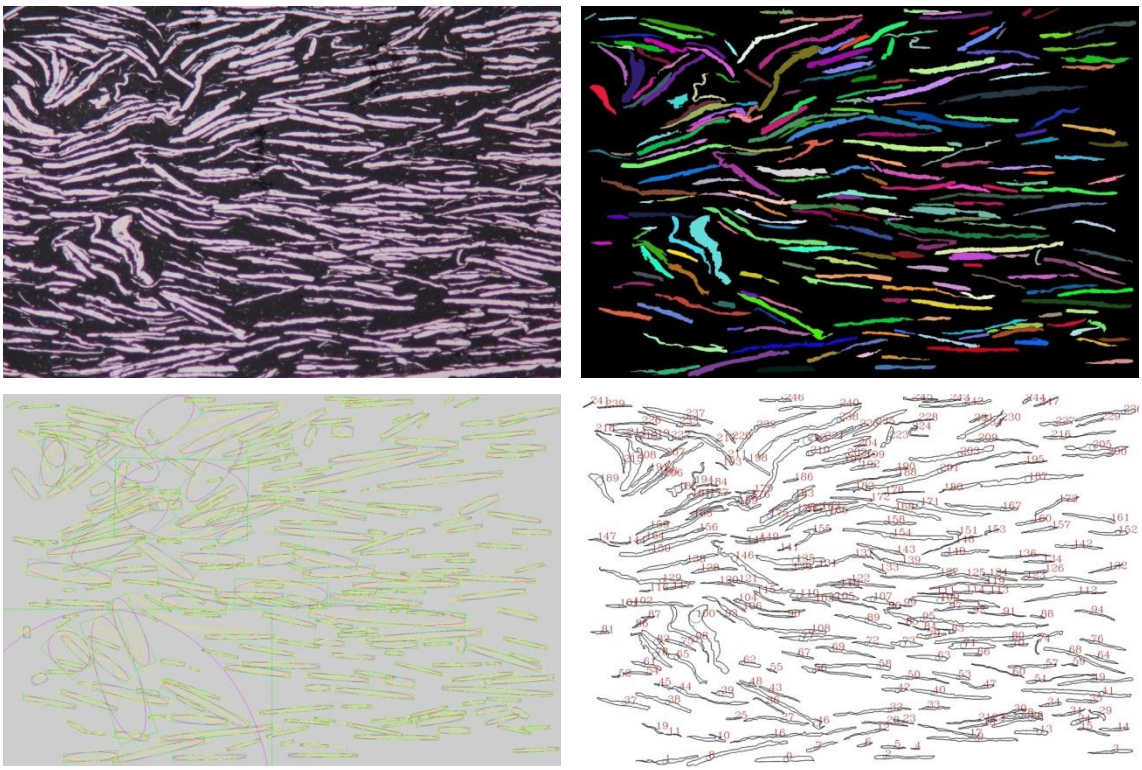

Fig. 3.15 Aspect ratio measurement with maximum inscribed circle method for the sample achieved under condition: milling time 10h, rotation speed 309rpm. (a) original image, (b) metal particle segmentation result, (c) Fit ellipse calculation and (d) maximum inscribed circle result.

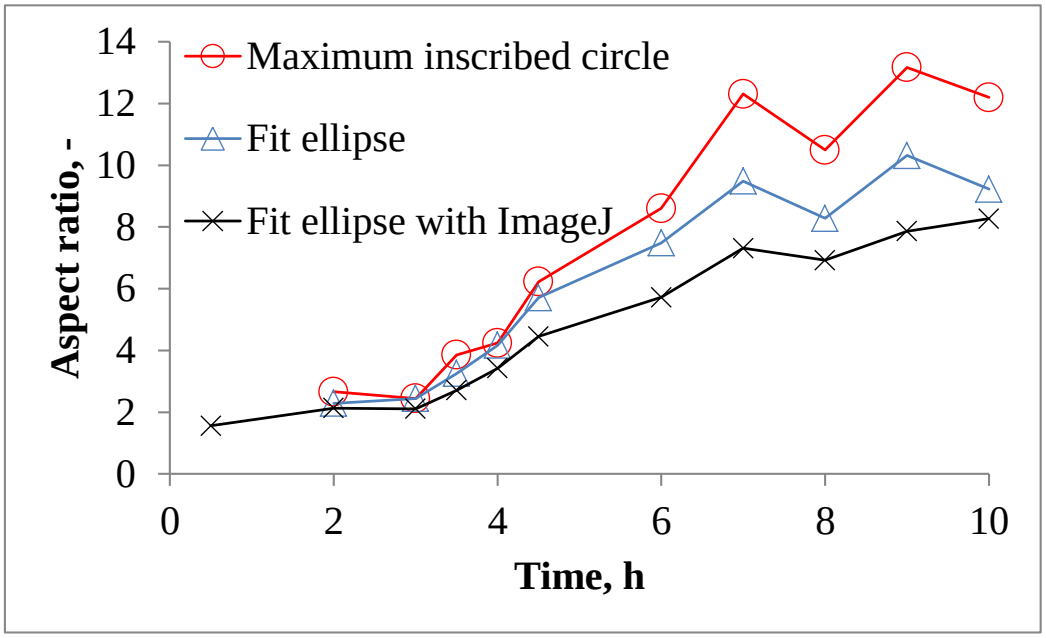

Fig. 3.16 Comparison of aspect ratio result with different methods for the samples under different conditions.

3.5.2 Major axis finding method

Although the maximum inscribed circle method yielded better result than the conventional fit ellipse method, it still had symmetric error when the particle shape is rectangle. Thus, we proposed another method to improve the evaluation of aspect ratio. As is shown in Fig. 3.9, the aspect ratio is:

$$AR = \frac{l_{major}}{l_{minor}} = \frac{l}{d_{MIC}} \tag{3.4}$$

Then we can directly calculate aspect ratio of a particle if we can measure the major axis length and the minor axis length.

3.5.2.1 Major axis extraction

As been stated previously, the major axis of a metal particle should be the curve that connecting the two ends of the particle. The thinning algorithm, which extracts the skeleton of a shape, is an appropriate method to calculate the major axis. Fig. 3.17 shows an example of skeleton extraction in a binary image, in which 0 pixels represent background and 1 pixels stand for the particle pixels. The right image is the skeleton achieved from the left image with thinning. The application results of thinning on the real image have been shown in Fig. 3.18 (a). The pink curves are the metal particle boundaries and the black curves are the skeletons. The skeletons have been numbered for better observation. One problem of this method is that there are many short branches, as shown in Fig. 3.18 (b). This will enlarge the skeleton length of the metal particles. Usually, the major axis length contains three parts, which are skeleton length and the distance from the endpoint to the particle boundaries. The over-estimation of skeleton length will make the evaluated major axis length large. Thus, the evaluated aspect ratio result, which is 23.82, was over-estimated. It is so large that the short branches must be eliminated.

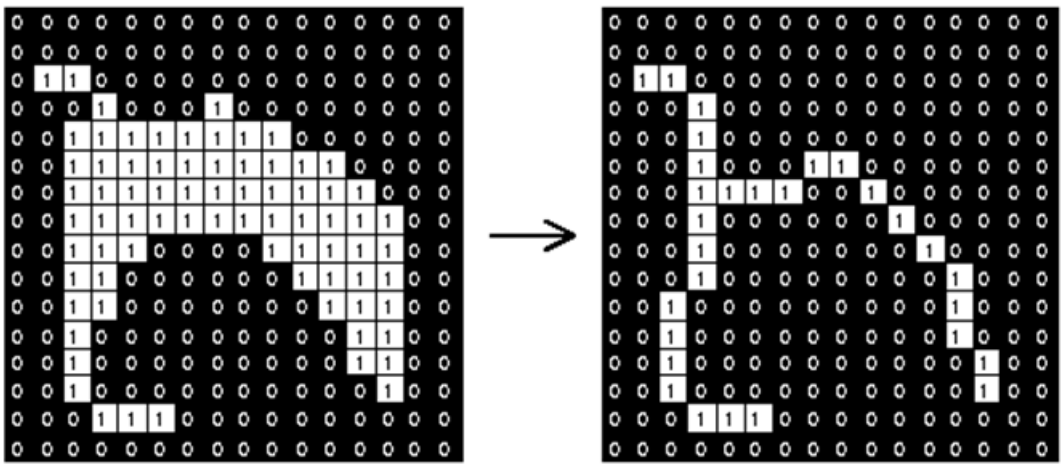

Fig. 3.17 Example of thinning (skeleton extraction).

Fig. 3.19 shows the illustration of the proposed method to eliminate the short branches. Red circles construct a skeleton obtained from thinning operation and we must extract the skeleton of the particle from them. Usually, short branches and loops are common in a skeleton from thinning operation. Assume the skeleton obtained from thinning is a pipe and water can flow through. When we pour water from one of the endpoints, the water will finally arrive in the other endpoints and immerse all the circles in the skeleton. As is illustrated, the first pixel immersed will be marked as 1. Its neighbors will be looked up and then be immersed and marked as 2. Similarly, the neighbors of circle 2 will be found and checked whether they have been immerses. The frontier moves to those circles not immersed. When the frontier meets bifurcation, the frontier divided and moves synchronously. When the frontier meets a loop, frontier will vanish if it meets with another frontier. Finally, only one skeleton from the endpoint to another endpoint is recorded. Only the skeleton with longest length will be used as the major axis length of the metal particle.

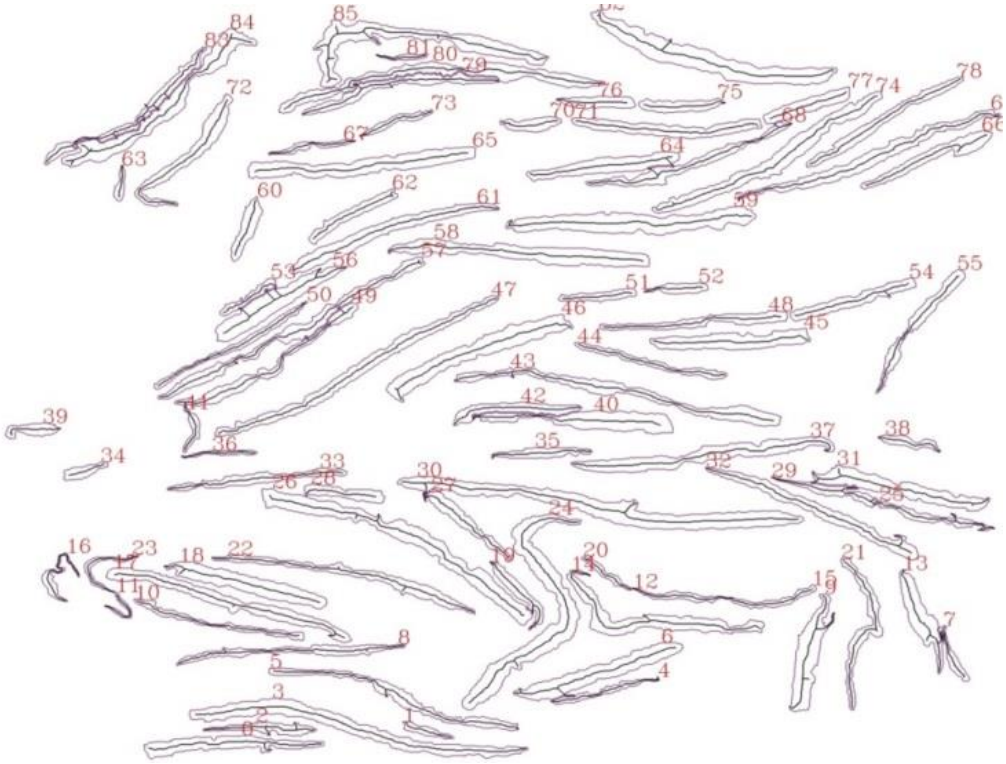

(a) Skeleton extraction result using thinning algorithm.

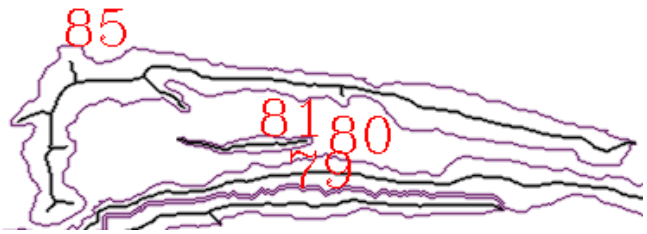

(b) Short branches in the skeleton extraction result with thinning operation.

Fig. 3.18 Skeleton extraction result of metal particles with thinning operation.

Fig. 3.20 shows the short branch elimination result for Fig. 3.18 (b). The purple curves are the metal particle boundaries and the black curves are the extracted major axis from the thinning result. Obviously, all of the short branches have been eliminated and the major axis was properly extracted. The final major axis extraction results for the

overall metal-ceramic image are shown in Fig. 3.21. In contrast to the results in Fig. 3.18(a), all the skeletons of the metal particles have no short branches. Thus, the proposed method yielded much better major axis length estimation result than the conventional thinning operation.

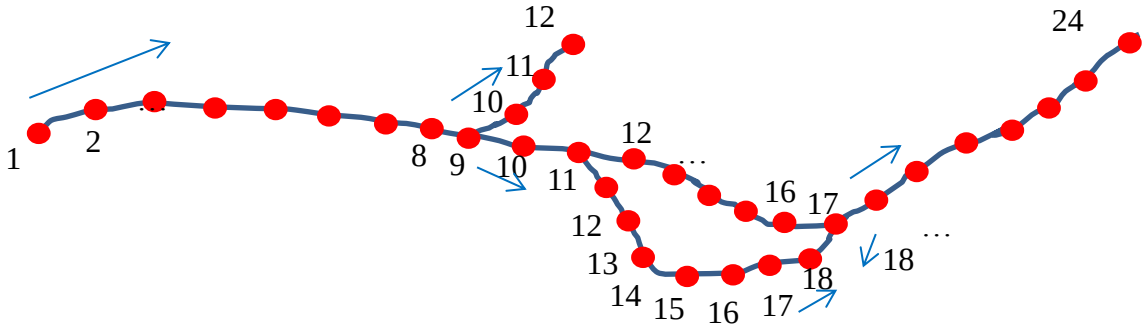

Fig. 3.19 Illustration of moving frontier method to achieve major axis.

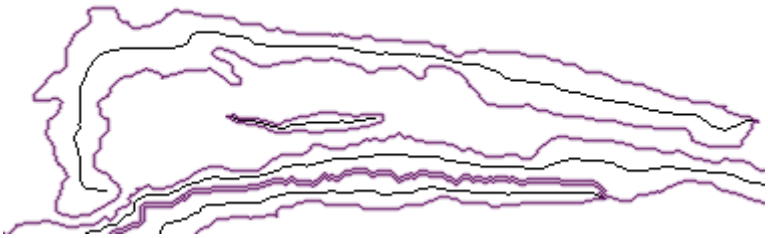

Fig.3.20 Short branches elimination result after the moving frontier method for Fig. 3.18 (b).

Fig. 3.21 Major axis extraction result for the whole image.

3.5.2.2 Minor axis estimation

Minor axis of the metal particles is evaluated by calculating the diameter of the maximum inscribed circles. Fig. 3.22 (a) is the maximum inscribed circle calculation results for the whole image. A zoomed-in image for No. 65 particle is shown below in Fig. 3.21 (b). Usually, the minor axis length is the maximum thickness of the metal particles if the curvature near minor axis is gentle. However, the minor axis length will be larger when the curvature near minor axis is dramatic.

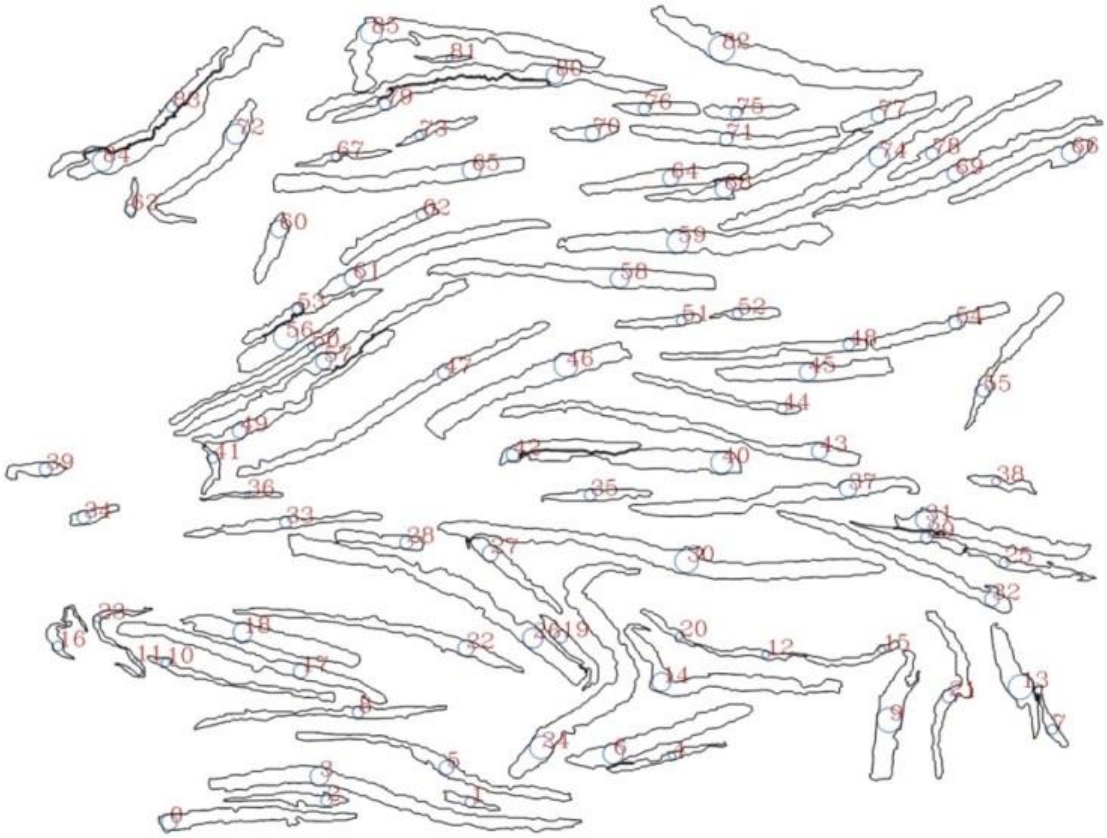

(a) the whole image

(b) No. 65 particle.

Fig. 3.22 Result of maximum inscribed circle calculation . (a) the whole image, (b) No. 65 particle.

3.5.2.3 Image analysis procedures

Fig. 3.23 shows the image analysis procedures in this chapter. Firstly, we achieved the micrographs of the metal-particle composite. A watershed transformation with hand

drawn markers was performed to acquire separated individual metal particles. The moving frontier method was proposed to find major axis from skeleton extraction result by thinning algorithm. Meanwhile, the minor axis was estimated by calculating the diameter of maximum inscribed circles. Finally, the aspect ratio was calculated by dividing major axis length with minor axis length.

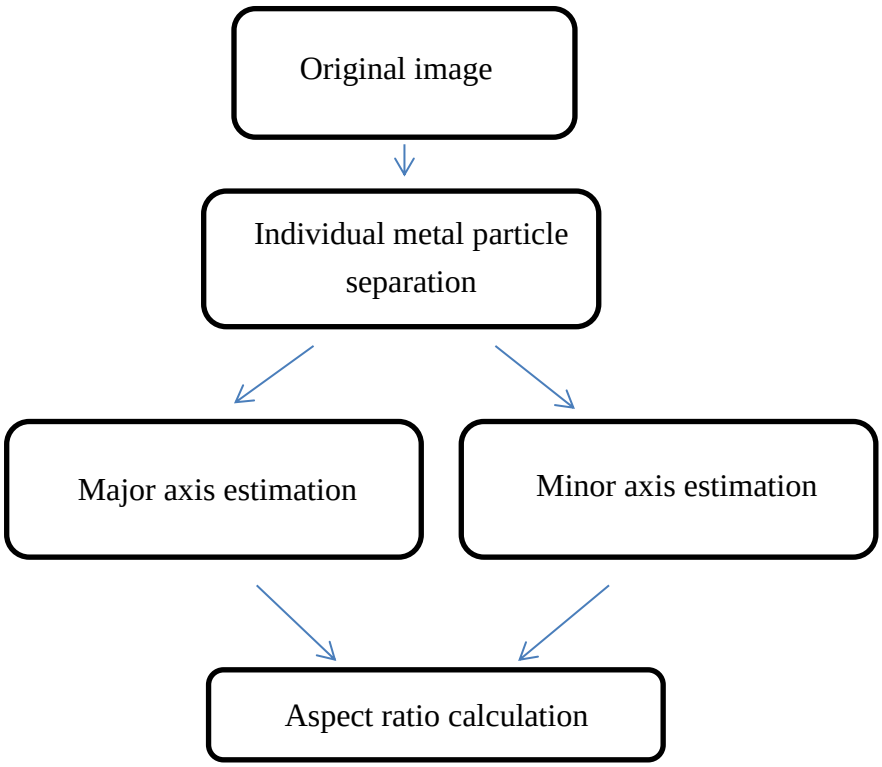

Fig. 3.23 Image analysis procedures in this chapter.

3.5.2.4 Aspect ratio measurement results by major axis finding method

Fig. 3.24 shows the comparison of aspect ratio measurement result with proposed method and conventional methods for individual metal particles segmented with watershed transformation using manually drawn markers. The relative error (Eq. 3.1) was used to compare the accuracy of different methods. The results show that the fit

ellipse method produced accurate results for the straight striped metal particles, however, had great error when the metal particle shape is bended striped. The maximum relative error of proposed method is under 30% in comparison of 100% for conventional method. This means that the proposed method produced more accurate results than the conventional method

$$relative \quad error = \frac{|AR - AR_{manual}|}{AR_{manual}} \times 100\% \tag{3.5}$$

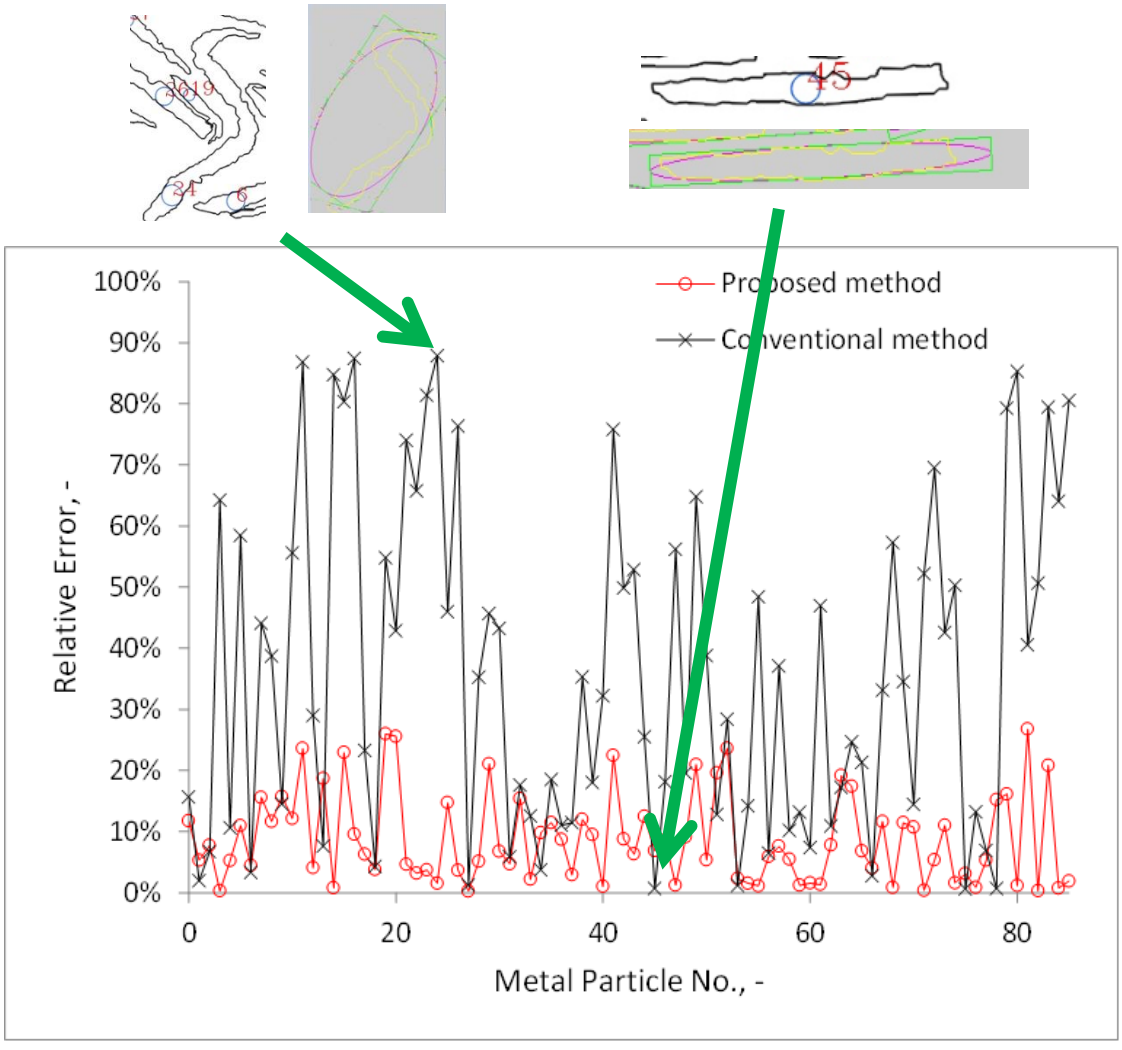

Fig. 3.24 Comparison of results with proposed frontier moving method and fit ellipse method.

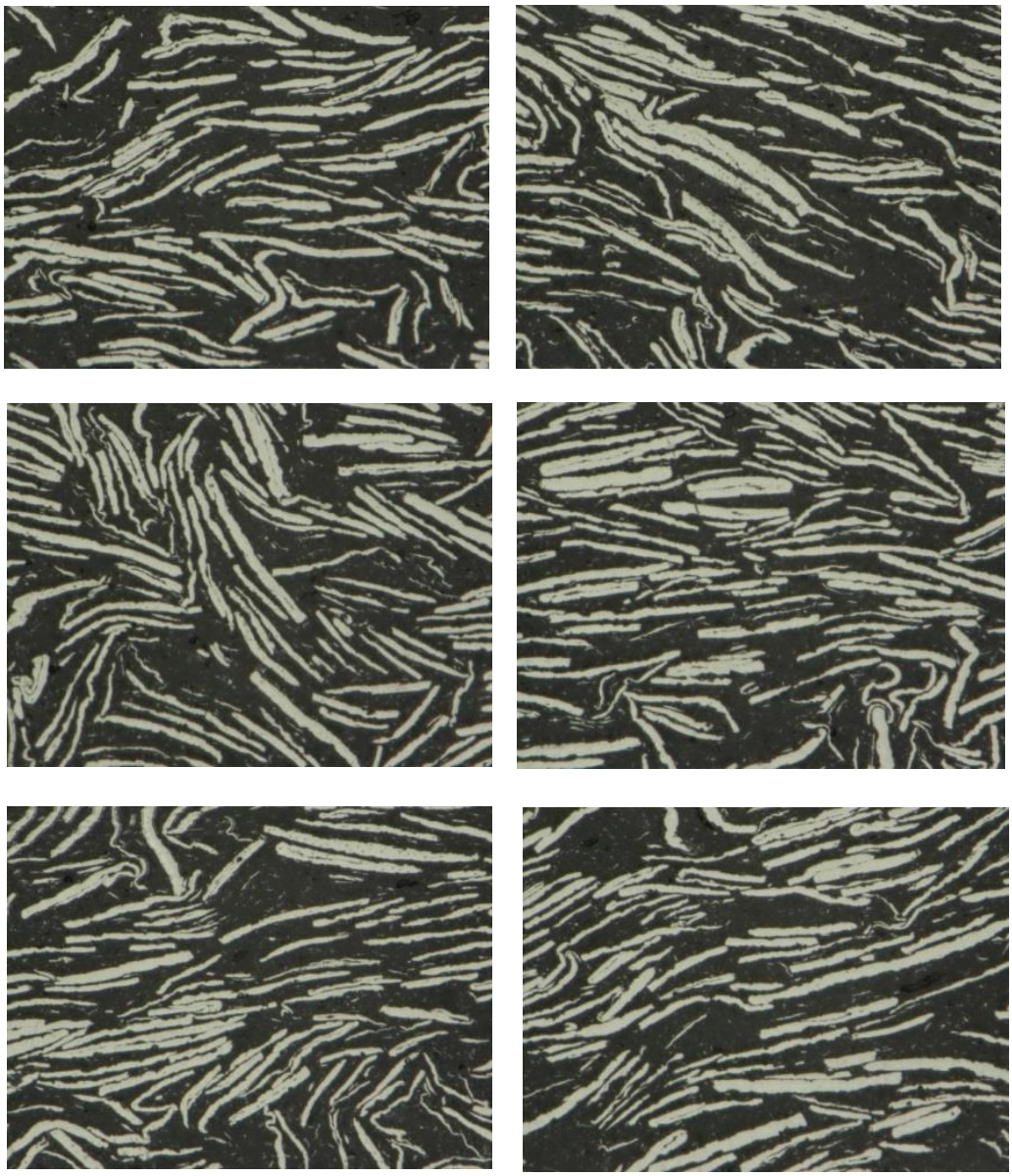

Fig. 3.25 Samples used to testify the aspect ratio measurement for mean aspect ratio. a) sample No. 1, b) sample No. 2, c) sample No. 3, d) sample No. 4, e) sample No. 5 and f) sample No. 6.

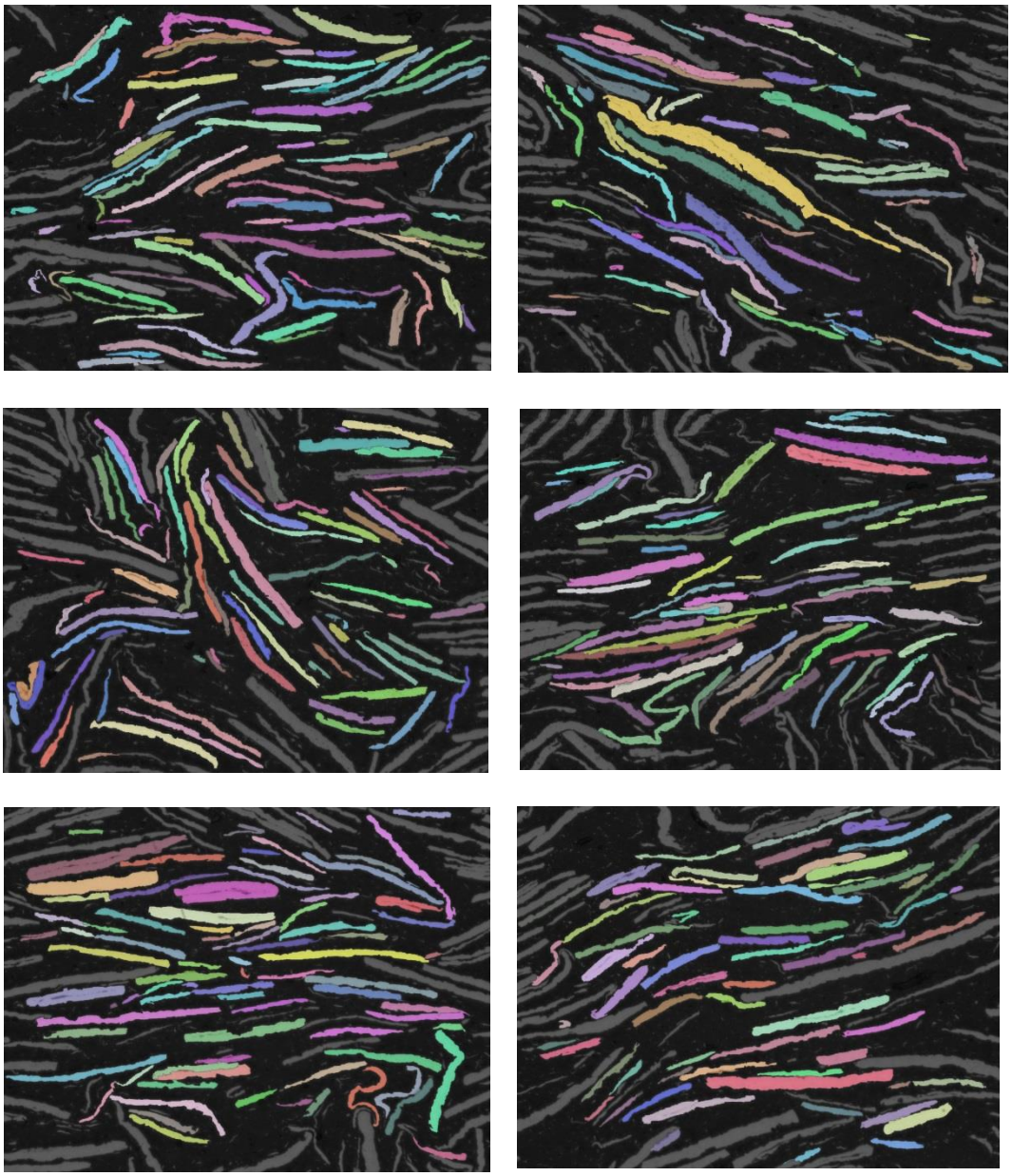

Fig. 3.26 Metal-particle segmentation result for the samples in Fig. 3.17. a) sample No. 1, b) sample No. 2, c) sample No. 3, d) sample No. 4, e) sample No. 5 and f) sample No. 6.

Fig. 3.27 Major axis finding result of the samples in Fig. 3.17. a) sample No. 1, b) sample No. 2, c) sample No. 3, d) sample No. 4, e) sample No. 5 and f) sample No. 6.

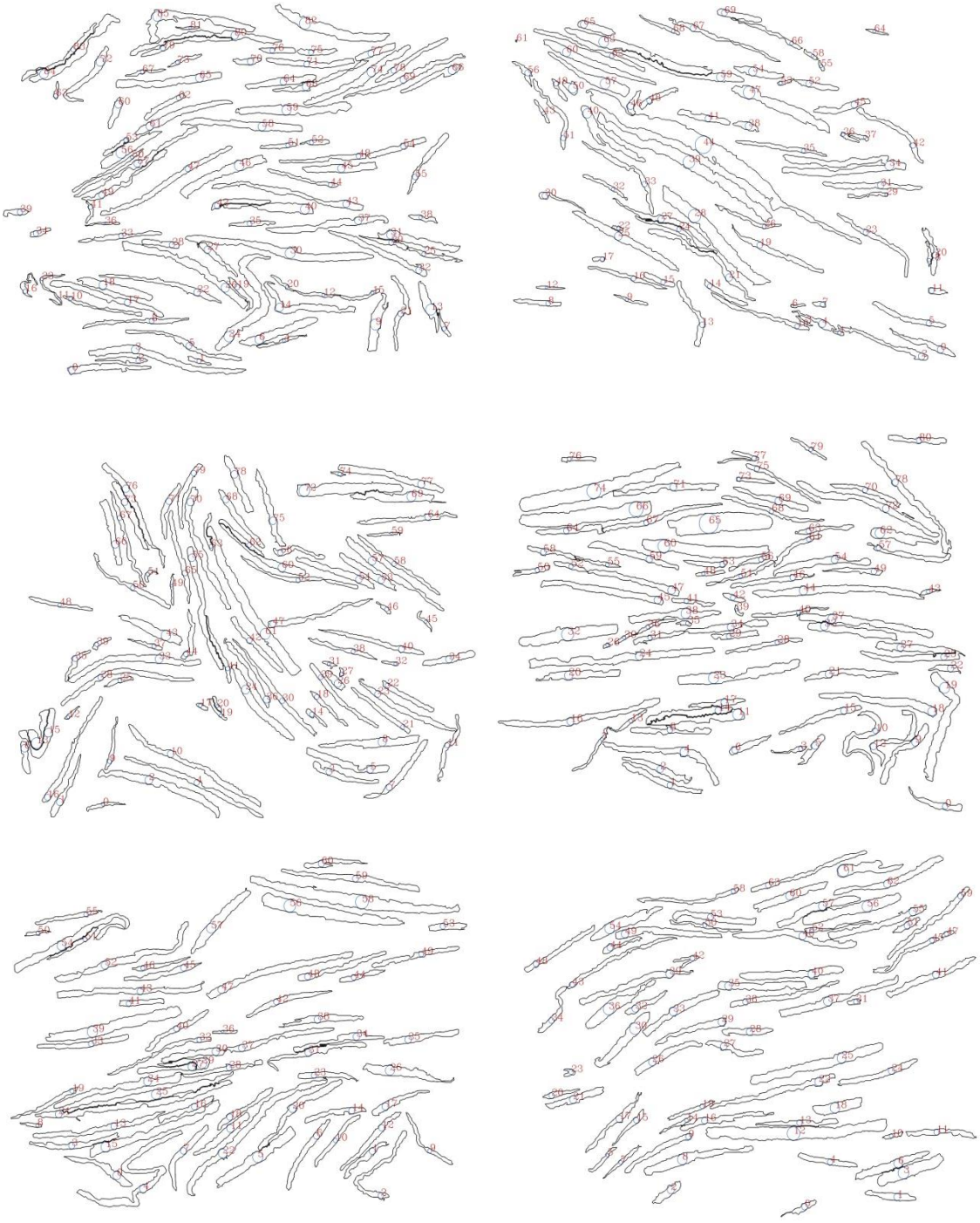

Fig. 3.28 Minor axis calculation with maximum inscribed circles for samples in Fig. 3.17. a) sample No. 1, b) sample No. 2, c) sample No. 3, d) sample No. 4, e) sample No. 5 and f) sample No. 6.

The measurement of mean aspect ratio value for all the metal particles in an microscopic image is also conducted and compared. Fig. 3.25 shows six original images used to measure aspect ratio of metal particles. Fig. 3.26, Fig. 3.27 and Fig. 3.28 show the results of metal particle segmentation, the major axis extraction and minor axis calculation. The mean value of the individual metal particles was used as the aspect ratio of the whole image. Fig. 3.29 is the result of mean aspect ratio measurement. It can be seen from the figure that the proposed method in this chapter gives much closer result to the manual result than the conventional evaluating method. The average manual result is a little larger than the proposed method because of the inherent problem of manual measurement. As is known, the major axis in manual measurement is a polyline which certainly is larger than the skeleton length of metal particles.

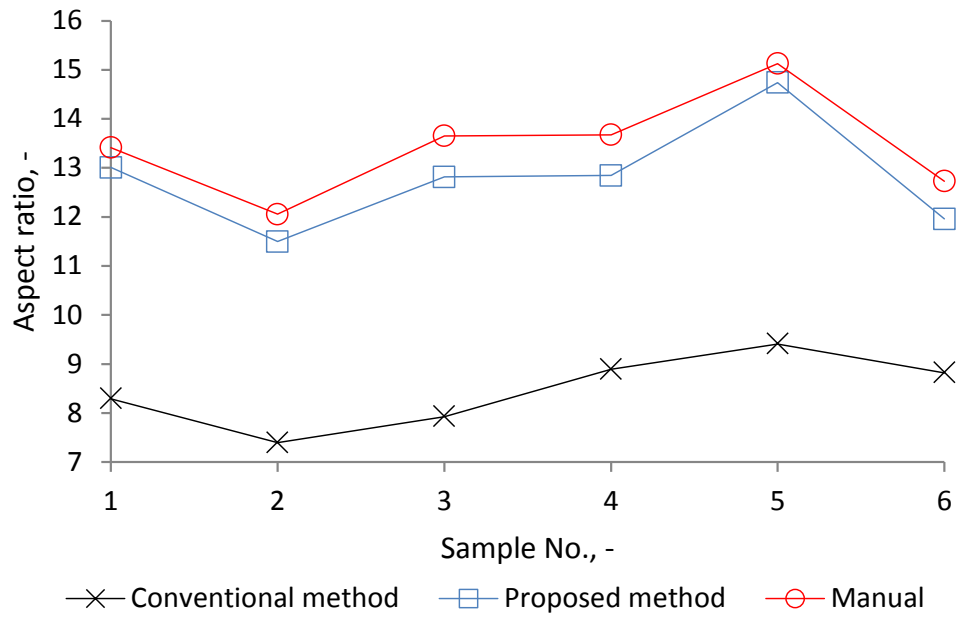

Fig. 3.29 Comparison of mean aspect ratio results with proposed method and fit ellipse method.

3.6 Summary

An image analysis method for metal particle aspect ratio measurement has been proposed in this chapter. The improvement comprises of two parts. The first one is the image segmentation method for metal particles and the second one is the aspect ratio evaluating method. Conventionally image segmentation method for aspect ratio is based on watershed transformation using automatic marker-image preparation method. It either over-segmented or under-segmented the metal particles in glass matrix. Thus, we used manual method to prepare the marker-image. The results showed that the manual method produced much better result in contrast to the watershed with UEP method and the method in chapter 2. The conventional aspect ratio evaluating method is fit ellipse method. It worked well for the straight striped metal particles, however, under-estimated those with bended strip shapes. In this chapter, a new image analysis method for aspect ratio evaluation has been proposed. Firstly, the major axis is estimated using skeletons extracted by thinning method. A further processing with proposed moving frontier method is used. Secondly, the minor axis length is estimated using the diameter of the maximum inscribed circle.

The comparison result of aspect ratio for individual metal particles shows that the proposed method produced much more accurate result than the conventional method, no matter the metal particle shape is straight strip or bended strip. The mean value for the individual metal particles in several images also proved that the proposed method produced closer result to the manual result than the conventional method.

References

1. M. Rosso, *Journal of Materials Processing Technology*, 2006, **175**, 364-375.

2. Y. Waku, N. Nakagawa, T. Wakamoto, H. Ohtsubo, K. Shimizu and Y. Kohtoku, *Nature*, 1997, **389**, 49-52.

3. Y. Waku, T. Yamashita, H. Kitagawa, M. Yoshinobu, H. Katsuyama, D. Hamano and S. Harui, *Scientific Reports*, 2017, **7**, 14662.

4. F. Bueche, *Journal of Applied Physics*, 1972, **43**, 4837-4838.

5. L. E. Nielsen, *Industrial & Engineering chemistry fundamentals*, 1974, **13**, 17-20.

6. Y. Waku, in *Advances in Gas Turbine Technology*, InTech, 2011.

7. Y. Waku, S. Iwamoto, M. Yoshinobu, S. Harui and K. Isobe, *Journal of the Japan Society of Powder and Powder Metallurgy/Funtai Oyobi Fummatsu Yakin*, 2010, **57**, 747-752.

8. Y. P. Mamunya, V. Davydenko, P. Pissis and E. Lebedev, *European polymer journal*, 2002, **38**, 1887-1897.

9. A. Celzard, E. McRae, C. Deleuze, M. Dufort, G. Furdin and J. Marêché, *Physical Review B*, 1996, **53**, 6209.

10. L. Gao, Y. Yan, G. Lu and R. M. Carter, *Flow Measurement and Instrumentation*, 2012, **27**, 20-28.

11. J. Cousty, G. Bertrand, L. Najman and M. Couprie, *IEEE Transactions on*

Pattern Analysis and Machine Intelligence, 2009, **31**, 1362-1374.

12. P. Soille, *Morphological image analysis: principles and applications*, Springer Science & Business Media, 2013.

13. C. Igathinathane, L. O. Pordesimo, E. P. Columbus, W. D. Batchelor and S. Sokhansanj, *Computers and Electronics in Agriculture*, 2009, **66**, 147-158.

14. E. J. Liu, K. V. Cashman and A. C. Rust, *GeoResJ*, 2015, **8**, 14-30.

Chapter 4. Image segmentation for dendritic microstructure and its application on SDAS and DCS measurement for Al-Si alloy based on mathematical morphology

The dendritic morphology has long been a topic for microstructure evaluation in alloys. However, the image analysis methods found difficulties in automatically or semi-automatically produce desirable SDAS and DCS measurement results. In this chapter, we proposed an image analysis method for semi-automatically achieve the SDAS and DCS results for different dendritic morphology.

4.1 Introduction

Secondary dendrite arm spacing (SDAS) has significant correlation to the local solidification time or cooling rate in the solidification process of aluminum alloys[1, 2]. Massive research has been conducted to reveal the quantitative correlation between them[3]. As is shown in Eq. 4.1 and Eq. 4.2, the SDAS positively correlate with the local

solidification time[2]. Here, c and n are the constant co-efficient. Usually, n is a value between 0.22 and 0.33 for aluminum alloys. t is the local solidification time, R is the cooling rate and ΔT_s is the non-equilibrium temperature.

$$SDAS = ct^n \tag{4.1}$$

$$t = \frac{\Delta T_s}{R} \tag{4.2}$$

Dendrite cell size (DCS) is another concerned dendritic morphology parameter. According to Spears[3] and Caceres[4], the ductility of the aluminum alloy has significant correlation to the DCS. Usually, fine DCS promises good ductility of the casting.

Fig. 4.1 illustrates the main parameters concerned in the dendritic structure analysis, which are SDAS and dendritic cell size (DCS), respectively. The former is the distance between the center lines of adjacent secondary dendrite arms (SDA) and the later one is the thickness of SDA.

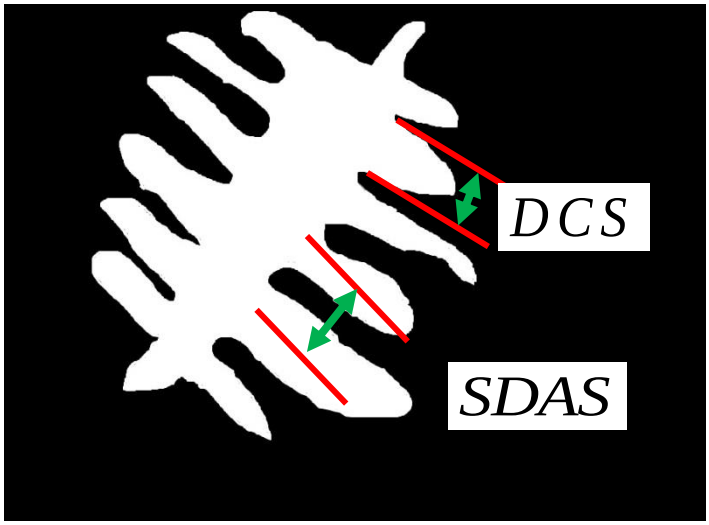

Fig. 4.1 Schematic for SDAS and DCS in a dendritic structure.

Traditionally, SDAS and DCS were measured manually by subjectively estimating SDA center lines. The results depend on the individual experience of the inspector. It must be measured several times to assure the objectivity. It would be labor-intensive.

Conventional SDAS measurement with image processing techniques tried to calculate the distance between adjacent center lines of eutectic phase in the space of two adjacent dendritic arms. Kalka[5] et al. used thinning algorithm to extract centerlines of inter-dendritic phase and then manually drew an intercept to measure the SDAS. He compared the samples from two component using statistic method and concluded that the similarity of two dendrite morphologies can be estimated by comparing SDAS distribution. The problem is the effectiveness. The SDAS measurement highly relies on the recognition of SDA edges with eutectic phase. If the edge of SDA is not clear, the measurement results of SDAS will be mistakenly estimated. In addition, the distance between center lines of inter-dendritic phases are not the SDAS. It is an indirect manner to evaluate the SDAS. Thus, it could not accurately reflect the dendrite morphology.

So far as the author knows, there is no reported image processing method to measure the DCS of the dendrite. In this study, measurement of DCS with image processing method will also be conducted.

In this chapter, the conventional SDAS measurement methods were discussed and a morphological method is proposed to semi-automatically extract SDA and to effectively measure the SDAS. In addition, the measurement of DCS has also been a task of the method. The measurement results with the traditional image processing method and the proposed image analysis method were also compared.

4.2 Conventional measurement methods

Usually, there are three types of methods in conventional measurement, which are manual method[6], intercept method[5] and mean intercept method[7]. These methods are illustrated in Fig. 4.2. Manual method is to judge the center lines of SDAs by human eyes and measure the distance between adjacent center lines by hand. Intercept method is to estimate center lines of eutectic phase and use a manually drawn intercept to determine intersection points with the center lines. The distance between adjacent intersection points is taken as SDAS. The mean intercept method is to manually draw a line on the optical microscopic image of dendrites. The number of SDA that the line covers will be counted by human. The average SDAS will be estimated by dividing line length with SDA number. The intercept method is to calculate the distance between center lines of inter-dendritic phases. The center lines were achieved by thinning eutectic grains. Mean intercept method is to measure the mean distance between *n* dendrite arms. The manual method and mean intercept method are conducted by human and the intercept method is conducted by image processing method.

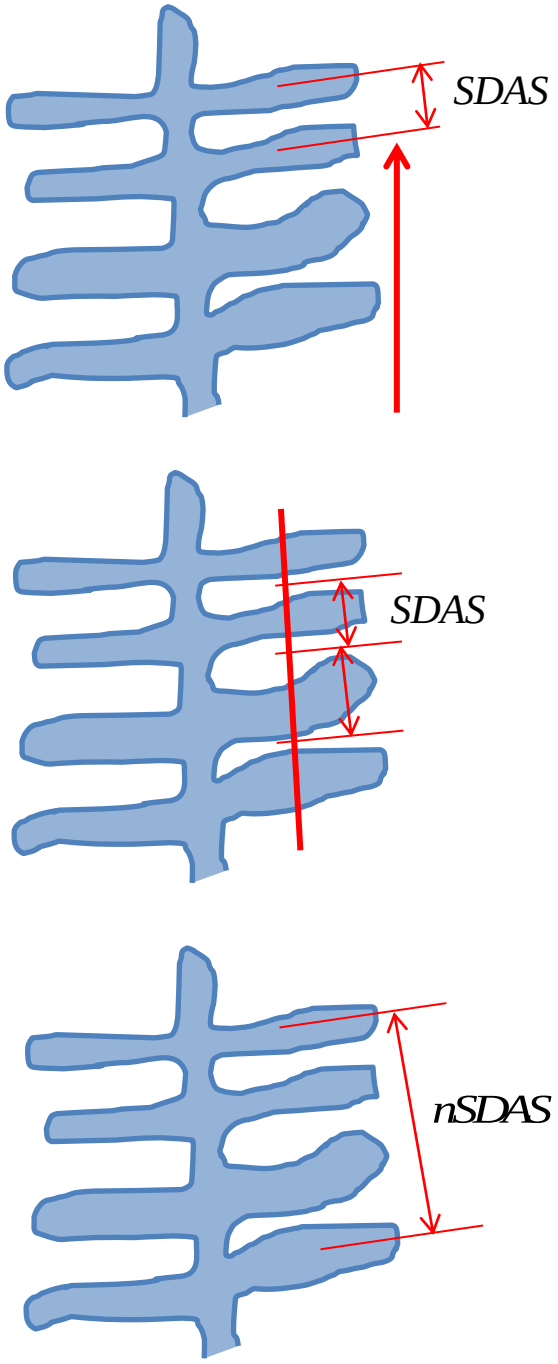

Fig. 4.2 Schematic of different SDAS measurement methods. a) manual method[6], b) Intercept method[5] and c) mean intercept method[8]

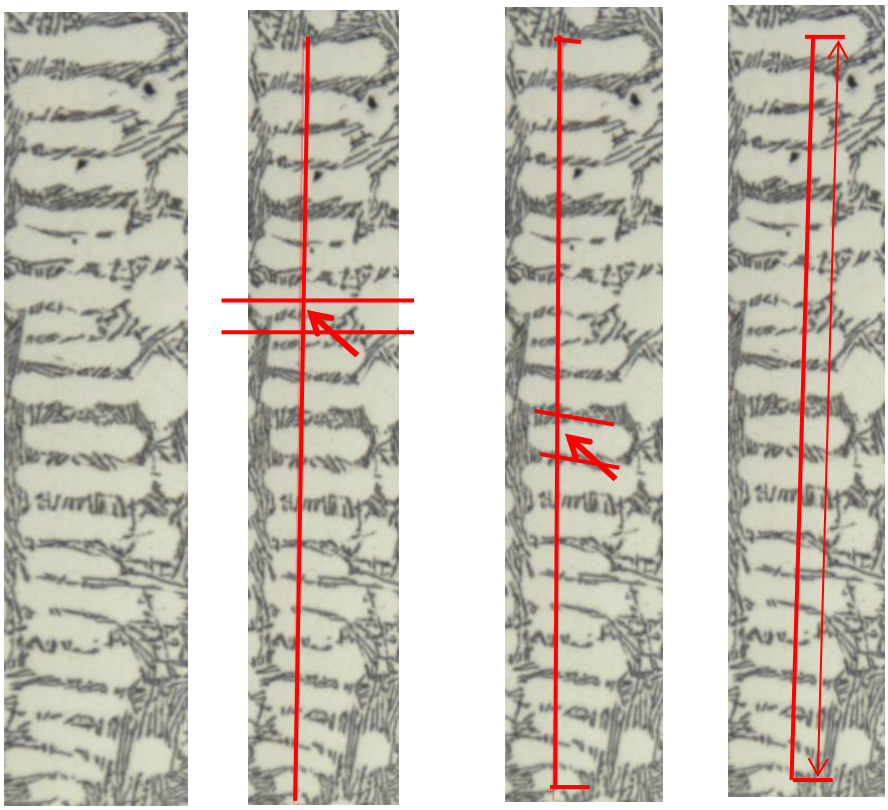

(a) (b) (c) (d)

Fig. 4.3 Example of conventional measurement for SDAS. a) original image, b) manual measurement, c) intercept method and d) mean intercept method.

Tab. 4.1 Mean SDAS results with different methods.

Methods	**SDAS(μm)**
Intercept	32.8
Mean intercept	35.2
Manual	33.7

Fig. 4.3 shows the implementation example of the conventional methods on the

practical dendritic structure shown in Fig. 4.3 (a). Fig. 4.3(b) shows the measurement of manual method. Center lines of the SDAs were estimated by human eyes. An intercept line was drawn manually to intersect with the center lines. The distance between adjacent intersection points was measured by hand and taken as SDAS. Fig. 4.3(c) shows the measurement of intercept method. Eutectic phase between adjacent SDAs will be thinned with thinning algorithm to extract center lines of the eutectic phase. These center lines will be used to approximate the SDA center lines. The program was coded in the environment of OpenCV (C++) plugged in Visual studio 2012. Fig. 4.3(d) shows the measurement of mean intercept method, the length of the intercept line covering n SDAs was measured and divided by n. The measured results were shown in Tab. 4.1. The manual measurement was conducted 10 times for one dendrite and calculated the mean result of the 10 times' measurement to improve the accuracy of manual measurement. Obviously, the intercept method yielded a relatively smaller SDAS mean value and the mean intercept method yielded a relatively larger SDAS.

4.3 SDAS measurement with mathematical morphology

The dendrite morphology in aluminum alloys is complex. In this study, we firstly conducted the SDAS measurement on the hand-drawn image. An automatic identification method for primary dendrite arm (PDA) and SDA was proposed. Subsequently, the measurement for SDAS in actual images was also presented.

4.3.1 SDA measurement in a hand-drawn dendrite

Hand-drawn dendrite is used in this section. Fig. 4.4 shows a hand-drawn dendrite. In this image, a complete dendrite structure (primary dendrite arms and secondary dendrite arms) is presented. This is an ideal case of dendrite in aluminum alloy microstructure. The automatic identification of PDA and SDA and automatic calculation of SDAS is useful for the potential application in actual dendrite structure.

In order to automatically measure the SDAS of this dendrite, the center lines of the primary and secondary dendrite arms must be identified automatically. In this section, we propose a method to identify the center lines of both primary and secondary dendrite arms in this study. It contains three steps. Firstly, skeleton of the dendrite is analyzed to identify PDA and SDA center curves. Next, fit lines of the center curves are obtained with least square method. Finally, PDA center lines are removed with Grubb's test method.

4.3.1.1 Skeleton extraction

Thinning[9] operation was used to extract skeletons for both PDA and SDA.. Fig. 4.5 shows the extracted skeleton using thinning algorithm. It can be seen that every dendrite arm has an endpoint in the skeleton and connected with a node. Therefore, the primary and secondary dendrite arms can be identified by counting pixels from endpoints to the nodes. The result of counting pixels from endpoints to nodes contains the center curves of SDAs and two PDA center curves.

Fig. 4. 4 Hand-drawn dendrite.

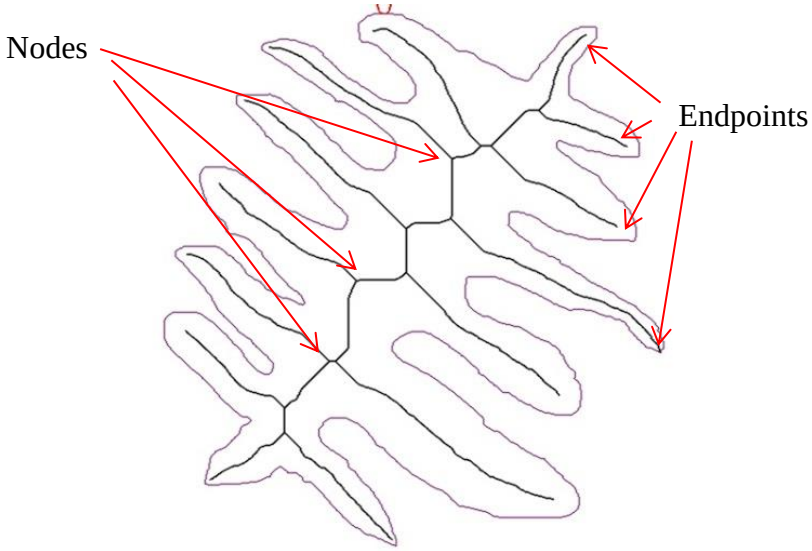

Fig. 4.5 Extracted skeleton of the manually-drawn dendrite.

4.3.1.2 Least square fitting to find center lines

The center curves of PDA and SDAs were extracted by counting pixels from endpoint to the nodes. The extracted dendrite arms were center curves of each dendrite arms. Least square method[10] was used to calculate the fit lines for the center curves. The algorithm of least square fitting is as follows.

The pixels in a center curve can be seen as a point set $P=\{p(x,y)\mid p(x,y)\in c\}$, here c is the center curve. Suppose line $l: y=a+bx$ is the fit line we want. Coefficient a and b can be calculated with:

$$a=\frac{\sum_{i=1}^{N} y_i \sum_{i=1}^{N} x_i^2-\sum_{i=1}^{N} x_i \sum_{i=1}^{N} x_i y_i}{n\sum_{i=1}^{N} x_i^2-\left(\sum_{i=1}^{N} x_i\right)^2} \tag{4.3}$$

$$b=\frac{n\sum_{i=1}^{N} x_i y_i-\sum_{i=1}^{N} x_i \sum_{i=1}^{N} y_i}{n\sum_{i=1}^{N} x_i^2-\left(\sum_{i=1}^{N} x_i\right)^2} \tag{4.4}$$

4.3.1.3 Grubb's test to identify PDA and SDA

Among the center lines calculated in the previous section, there are two PDA center lines. We must pick them out before calculating SDAS. Grubbs' test[11] was used to do this task. Generally, the slopes of PDA and SDA are different. In the ideal case, the center lines of SDAs are parallel to each other and those of PDAs are perpendicular to them. Therefore, the ideal correlation of PDA center line slope and SDA center line slope should match the following equation:

$$b_{PDA}=-\frac{1}{b_{SDA}} \tag{4.5}$$

Here, b_{PDA} and b_{SDA} are the slopes of PDA and SDA, respectively.

The calculation in the previous section yielded a series of surface slopes in sequence $\{b_1, b_2, ..., b_N\}$, N is the total number of primary and secondary dendrite arms. Grubb's test is a calculation to this sequence to determine an outlier. This outlier would be a value obviously different with the majority of the sequence. Apparently, it should be the slope of PDA. The algorithm of Grubb's test is as follows.

$$G = \frac{\max_{i=1,...,N} \left| b_i - \bar{b} \right|}{S} \tag{4.6}$$

Here, G is the Grubb's test statistic, $\bar{b}$ is the average of the sequence and S is the standard deviation of the data in sequence.

The Grubb's test was carried out twice to identify the two PDA center lines. Fig. 4.6 shows the result of PDA and SDA center line identification result. The fit lines achieved with least square method are taken as the center lines of primary and secondary dendrite arms. After the removal of PDA center lines with Grubb's test, we obtained the sequence of SDA center lines.

4.3.1.4 Measurement of SDAS

The center lines of SDAs have same start and end abscissa to those of center curves. In this study, they are actually fragments. Thus, the SDAS is actually the distance between two adjacent fragments. The average distance from one fragment to its adjacent fragment is taken as the SDAS. The final measurement result of SDAS is shown in Fig. 4.7.

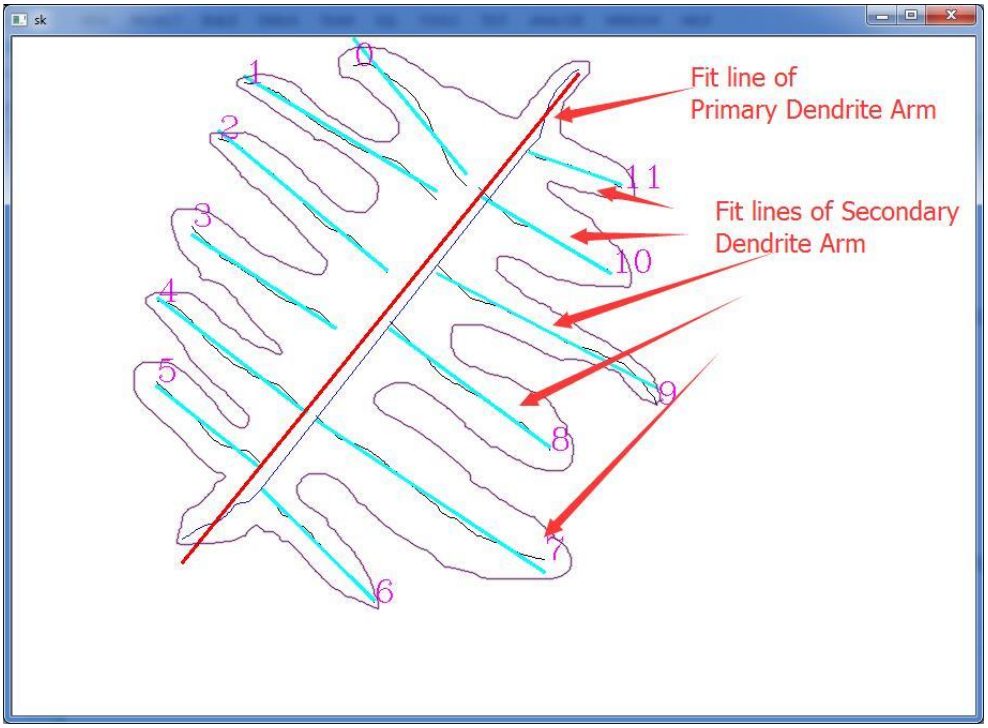

Fig. 4. 6 Identification of PDA and SDA.

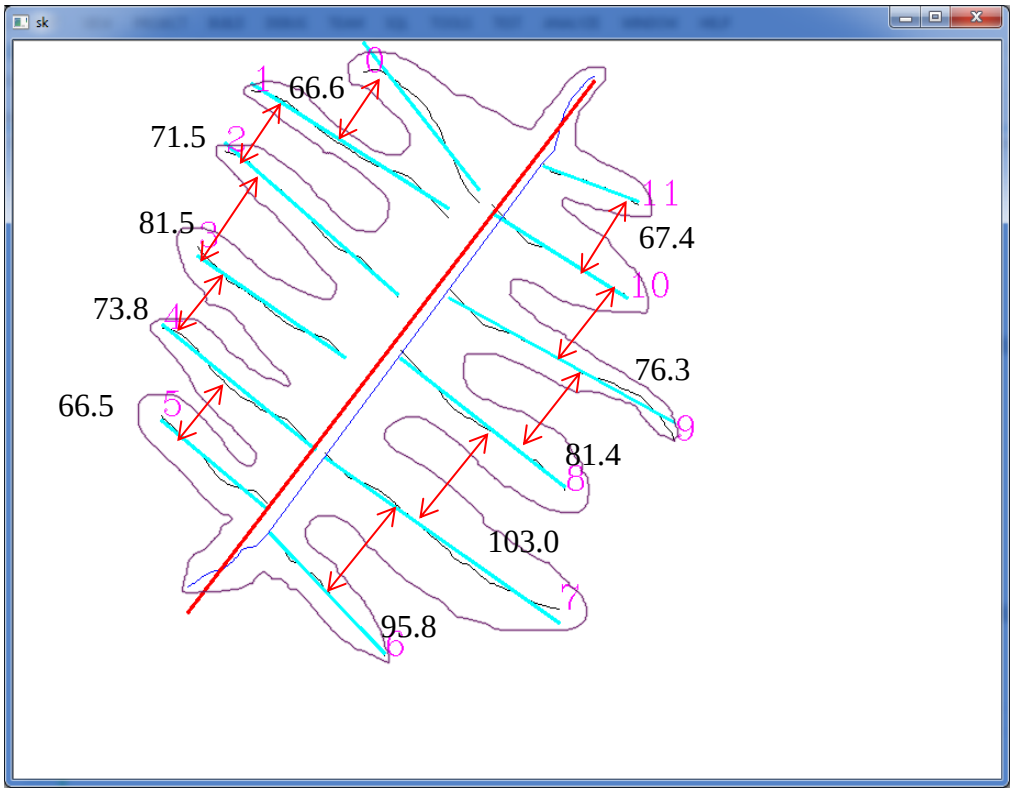

Fig. 4.7 Automatically calculated SDAS.

Although the automatic measurement from a complete dendrite structure is feasible for the hand-drawn image, the practical dendrite structure is much more complex. Therefore, a more efficient and effective method is required.

4.3.2 SDAS measurement for dendrite in actual images

Although the proposed method worked well for hand-drawn images, it has to be noted that the dendritic morphology is very complex. The automatic measurement calls for high requirement on the quality of actual images. This seriously restricted the effectiveness of dendrite arm spacing measurement.

An image segmentation method only extracting secondary dendrite arms was used to find concerned secondary dendrite arms. This method well solved the problem that some primary dendrite arms were under the polishing surface of samples or the secondary dendrite arms had already detached away from the primary dendrite arms[12].

Conventional image processing[5] method could not get the center lines of SDAs. It used the center lines of inter-dendritic phase to replace the center lines of SDAs. Thus, it could not directly and accurately measure the SDAS. Obviously, it failed to yield accurate result. In order to directly and accurately measure SDAS, center lines of the SDAs in dendrite must be extracted. Fig. 4.8 (a) shows a dendritic structure with coarsened inter-dendritic phases. An automatic segmentation using image analysis method in chapter 2 has been conducted and the result is shown in Fig. 4.8 (b). It shows that the primary α-Al grains were successfully segmented from the eutectic grains,

however, the procedure could not automatically tell which primary α-Al grain was dendrite. Moreover, the primary α-Al grains were over-segmented owing to the noises in the original image.

In this chapter, a semi-automatic extraction of secondary dendrite was used to segment the SDA from the adjacent grains. Firstly, a marker-image was prepared manually by drawing markers (red lines on Fig. 4.8 (c)) to indicate individual SDA and the background. Subsequently, the marker-image was applied to the watershed transformation and yielded an extraction result shown in Fig. 4.8 (d). Obviously, only the SDAs in one dendrite were segmented.

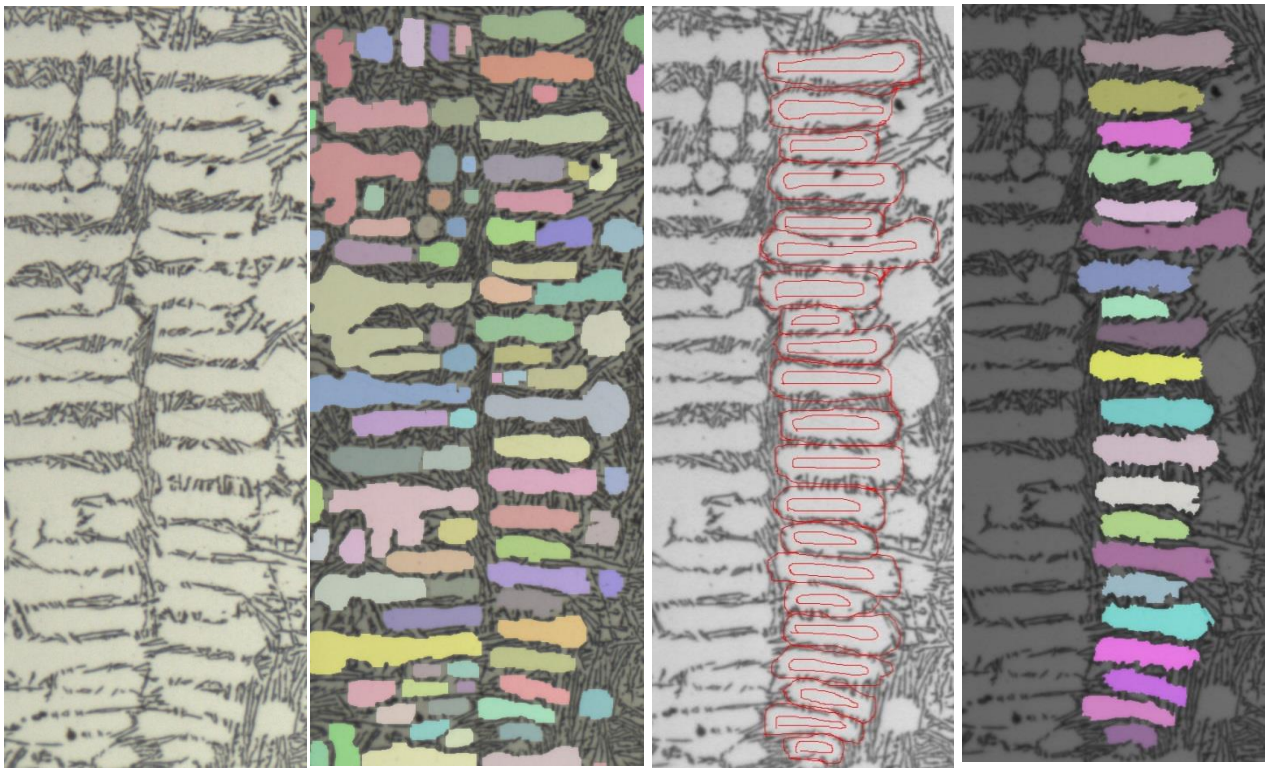

Fig. 4.8 SDA segmentation results using watershed transformation. a) original image, b) segmentation method in chapter 2, c) manual marker-image used in this chapter and d) SDA extraction result in this chapter.

4.3.2 Estimation of SDA center line

In the manual measurement, the center lines of SDA are estimated subjectively. Inspectors have to evaluate the location of SDA center lines depending on their individual experience. An objective estimation is needed. Thus, such an objective SDA center line estimating method was proposed in this section. Firstly, the skeletons of the individual SDAs were achieved with thinning algorithm, as shown in Fig. 4.9 (b). One problem of the skeleton extracted is that there are too many endpoints, which will influence the accuracy of SDAS measurement. Moving frontier method proposed in Chapter 3 was used to eliminate the excess endpoints. The result is shown in Fig. 4.9 (c). It can be seen that all the skeletons became a curve with only two endpoints.

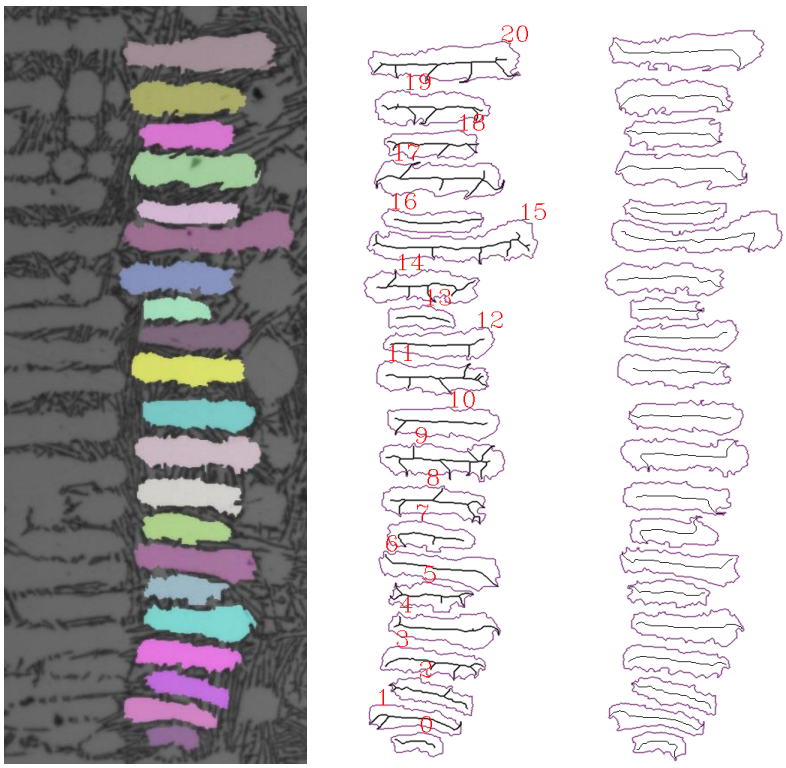

Fig. 4.9 SDA center curve extraction result. a) SDA, b) thinning result and c) center

curve result with moving frontier method.

The moving frontier method had improved the results of skeleton extraction. We got the center curves of the SDAs. Center lines of the SDAs were calculated using least square method. Blue lines in Fig. 4.10shows the line fit result with least square method. Apparently, the fit lines well reflected the location and direction of the skeleton.

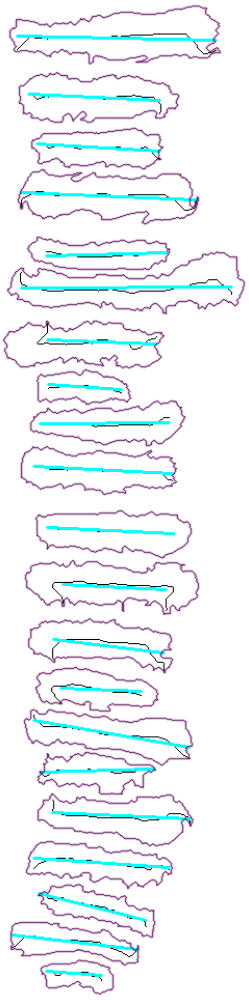

Fig. 4.10 Fit line of the skeleton with least square method.

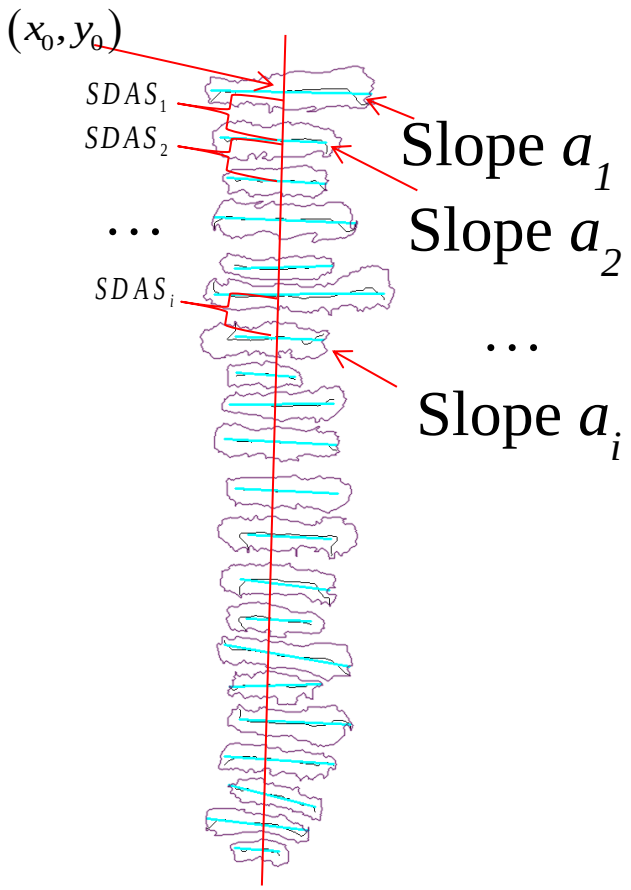

Fig. 4.11 Intercept line calculated according to the center lines in SDAs.

After the calculation of SDA center lines, a subsequent calculation of individual SDAS was performed. As shown in Fig. 4. 11 the slope of *i*th center line, a_i, was calculated. An intercept line was calculated according to the slopes of all the center lines, as depicted in Eq. 4.3 and Eq. 4.4, where $\bar{a}$ is the mean slope of center lines, N is the total center line number and $a_{intererceptt}$ is the slope of intercept line.

$$\bar{a} = \frac{\sum a_i}{N} \tag{4.7}$$

$$a_{intererceptt} = -\frac{1}{\bar{a}} \tag{4.8}$$

We suppose that the intercept line passes the point (x_0, y_0) so as to intercept all lines. In this case, it is the center point of center line 1. As can be seen in Fig. 4.11, the intercept line will intercept with all the center lines and yield a series of intercept points. We saved the points in sequence and then calculated the individual SDAS.

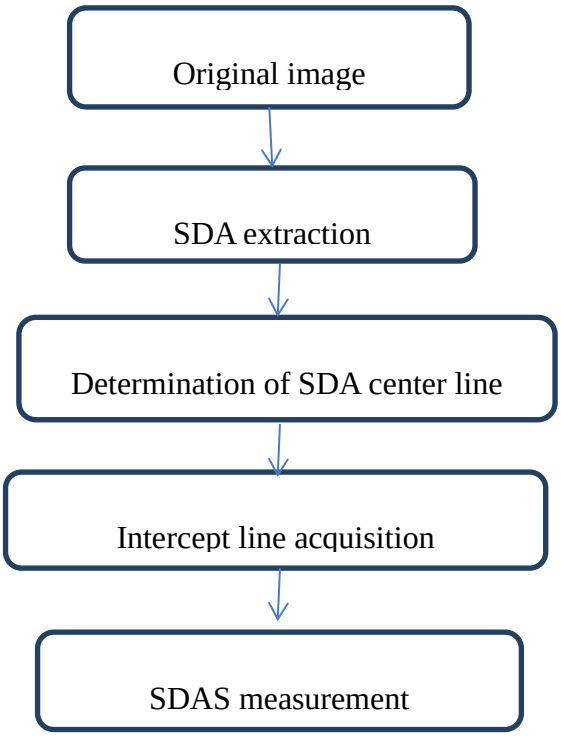

Fig. 4. 12 Image analysis procedures of SDAS measurement for dendrite in the proposed method.

4.3.3 Image analysis procedures

The programs of intercept method and the method proposed were coded with OpenCV (C++) plugged in Visual Studio 2012. Fig. 4.12 shows the flow chart of image analysis procedures in the proposed method for the SDAS measurement in Al-Si alloys

microscopic images. Firstly, the secondary dendrite arms were extracted from the original image with watershed transformation. A semi-automatic segmentation with manually drawn marker-image was used. Secondly, moving frontier method was used to extract the center curves of SDA. Thirdly, the least square method was used to get the fit lines of center curves. Finally, an intercept line was calculated depending on the average slope of center lines of SDAs and the center point of first center line. The SDAS was calculated by calculating the distance between adjacent intercept points. The DCS was the fragment length on the intercept line cut by the contours of SDA.

4.4 SDAS and DCS measurement results

4.4.1 Individual measurement of SDAS

Individual measurements for the SDAS in Fig. 4.8 (a) with intercept method, manual method and proposed method are shown in Fig. 4.13. The manual result was an average result of 10 times' measurement. The intercept method presents large difference with the manual result. This is because the intercept method used the distance between center lines of inter-dendritic phase as the SDAS while the real SDAS is the spacing between adjacent center lines of dendrite arms. In contrast, the proposed method yields a much closer result to the intercept method. A comparison of mean SDAS results with different methods is shown in Tab. 4.2. The results show that the intercept method gives an under-estimated result of SDAS and the mean intercept method produces an over-estimated result of SDAS. The proposed method produced a much closer result to the manual result in contrast to the other two methods. It can be seen from Fig. 4.13 and

Tab. 4.2 that the proposed method yielded much better result than the conventional methods.

Tab. 4.2 Mean SDAS results with different methods.

Methods	SDAS(μm)
Proposed	34.0
Manual	33.7

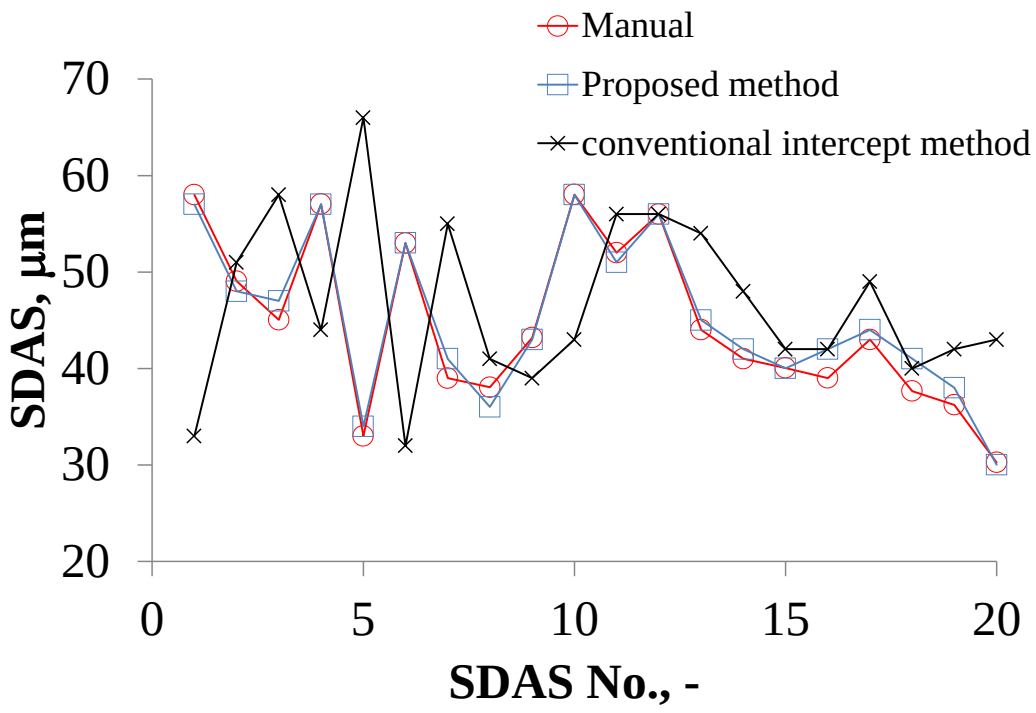

Fig. 4.13 Comparison of individual measurement results for the original image.

4.4.2 Individual measurement of DCS

Dendritic cell size has significant correlation to the aluminum alloy ductility[4], the

measurement of DCS is important to evaluate the mechanical performance of the alloys. The conventional intercept method with image processing cannot measure DCS of the dendrite. In contrast, the proposed method can also semi-automatically measure the DCS. Fig. 4.14 shows the result of DCS measurement results with manual method and proposed method. The manual result was also an average measurement of 5 times. It can be seen that the proposed method yielded a very close result to the manual method..

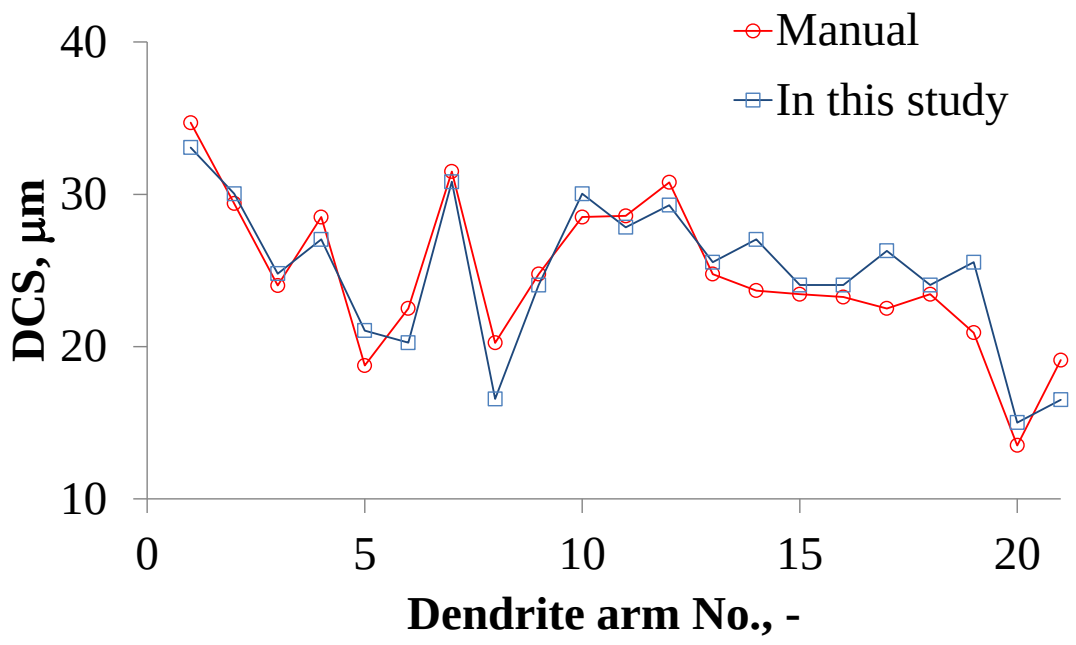

Fig. 4.14 DCS measurement result.

4.4.3 The influence of different dendritic morphology

There are many types of dendrite morphology in the micrograph of Al-Si alloy. Fig. 4.15 shows several types of the morphology. Fig. 4.15 (a) and (b) are the morphology in which the eutectic grains coarsened. In most cases like Fig. 4.10 (c) and Fig. 4.10 (d) only secondary dendrite arms can be observed. The inter-dendritic phase has not been

coarsened. Morphology shown in Fig. 4.15 (e), Fig. 4.15 (f) and Fig. 4.15 (g) is that the growing of dendritic arms is not adequate. In other words, the ripening rate is low and some dendritic arms are very short in contrast to the other arms. The last morphology investigated in this chapter is the morphology in which dendrite arm edges is not clear. This will influence the result of intercept method severely as there will be no center lines of the inter-dendritic phase when the edges are not clear.

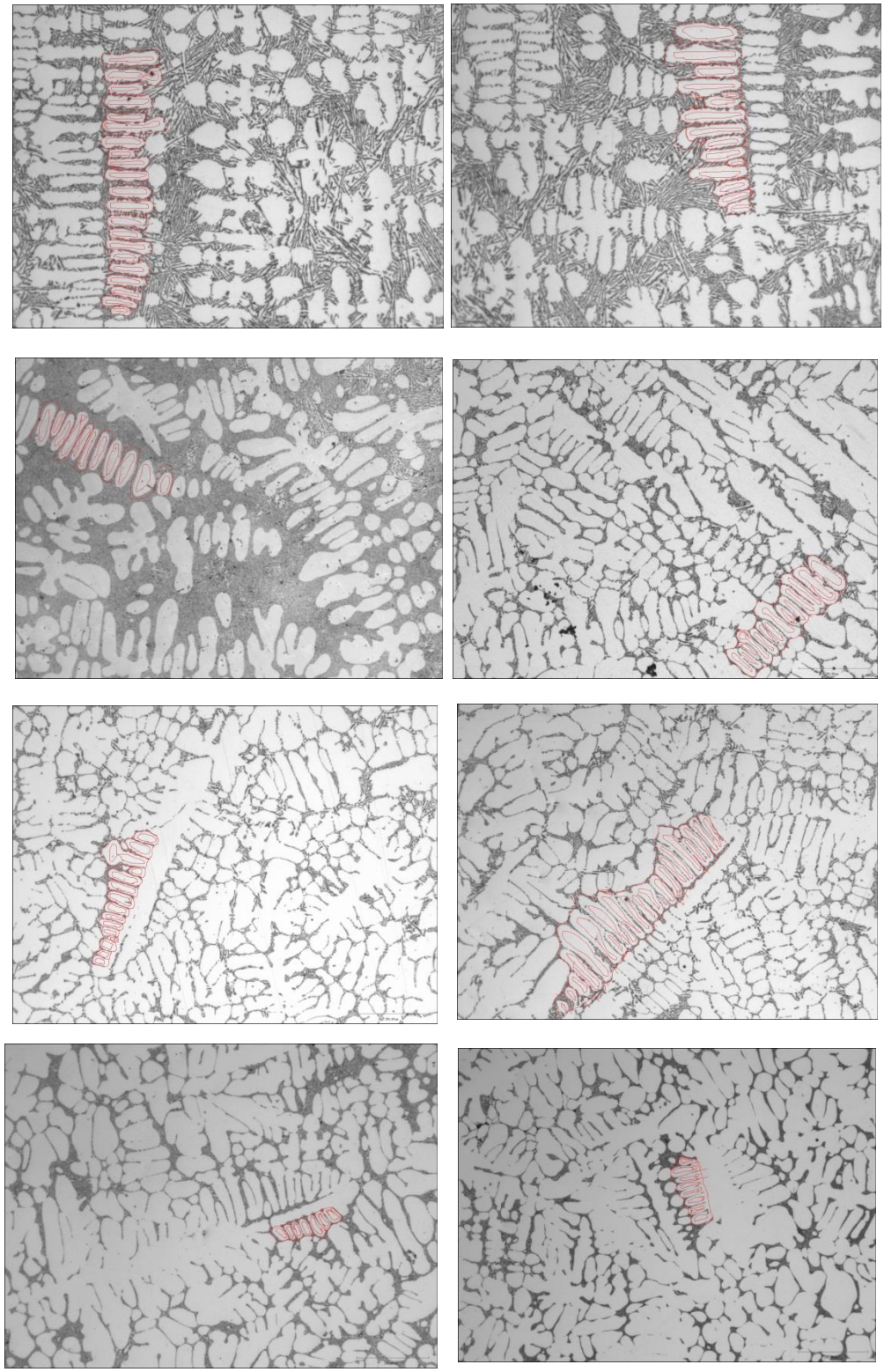

Fig. 4.15 Different dendritic morphology used to testify the effectiveness of the proposed method. a) and b) coarsened inter-dendritic phase, c) and d) SDA without

PDA, e) and f) Low ripening rate, g) and h) unclear dendrite arm edges.

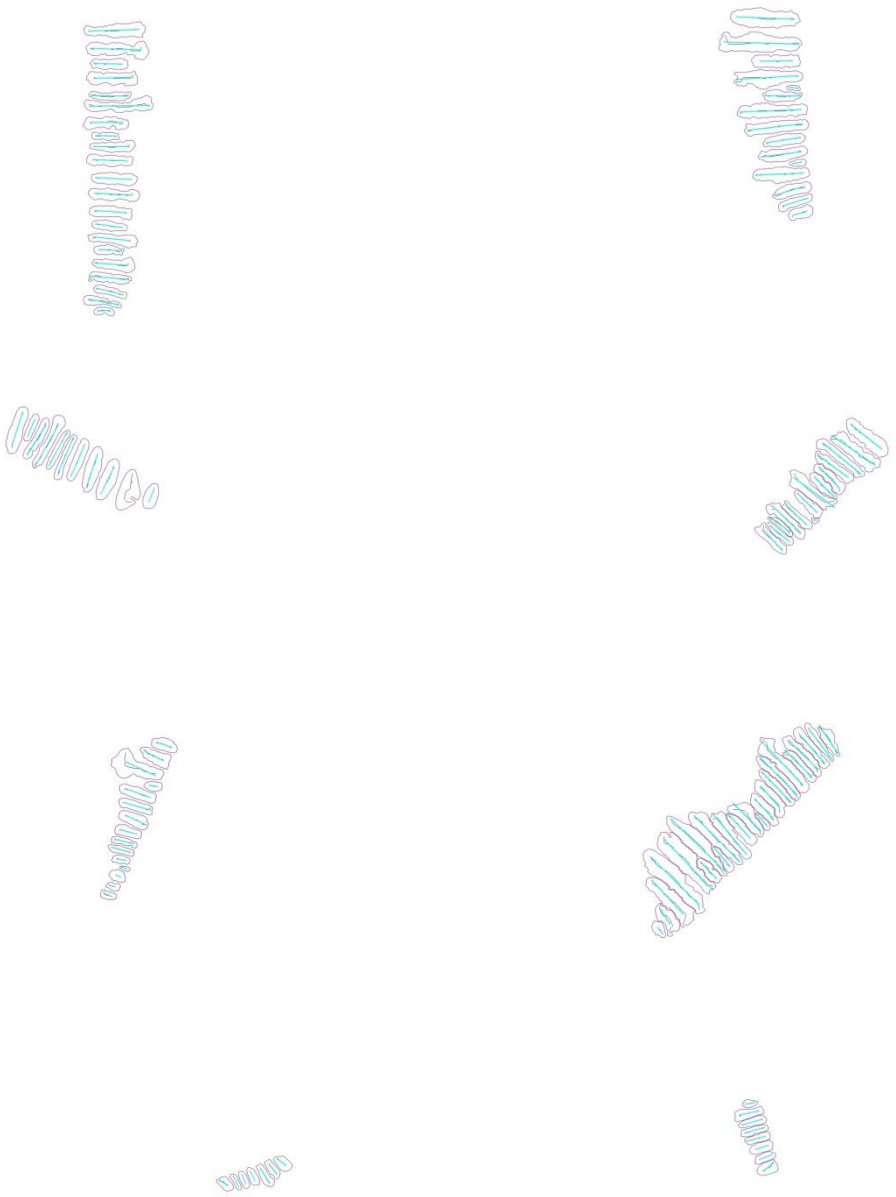

Fig. 4.16 SDA extraction result and center line extraction result. a) and b) coarsened inter-dendritic phase, c) and d) SDA without PDA, e) and f) Low ripening rate, g) and h) unclear dendrite arm edges.

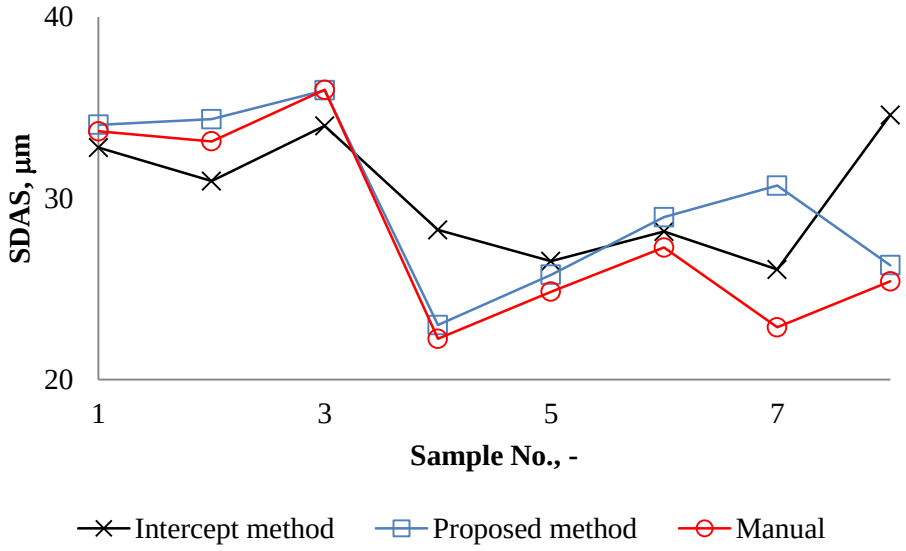

Fig. 4. 17 Mean SDAS measurement result for different dendritic morphology.

Fig. 4.16 shows the results of SDA extraction and center line estimation for different types of morphology. The mean SDAS results for the eight dendrite morphology with conventional intercept method and proposed method were measured and shown in Fig. 4.17. It can be seen that the proposed method yield more accurate result than the conventional intercept method for those dendrite morphology with coarsened inter-dendritic phase (Sample No. 1 and No. 2). For those in which inter-dendritic phase have not been coarsened, the proposed method still gives much more accurate results (Sample No. 3 and No. 4). However, when the ripening rate is low, the accuracy of the proposed method is unsteady. E.g. the proposed method yields close results to the manual result for No. 5 and No. 6 samples, but presents large error for Sample No. 7. It can be seen that most of the dendrite arms are short and "fat" and thus the center lines have been biasedly estimated. In contrast, when the dendrite arm shape is long-strip, the

measuring accuracy becomes much better. The application of the proposed method to the morphology with unclear edges (Sample No. 8) shows that the proposed method yields much better result than the conventional intercept method.

4.5 Summary

In this chapter, we proposed an image analysis method for semi-automatic measurement of secondary dendrite arm space (SDAS) and dendritic cell size (DCS) based on mathematical morphology. Firstly, a human subjective preparation of marker-image was conducted and used in watershed transformation. The segmentation result showed that the semi-automatic segmentation well achieved individual secondary dendrite arms. Secondly, the center lines of the secondary dendrite arms were estimated with moving frontier method and least square method. As the center lines were the fit lines of the dendrite arm skeletons, the program in this chapter could help to improve the objectivity of center lines.

The comparison of individual SDAS result with conventional intercept method, proposed method and manual method shows that the proposed method yielded closer result to the manual result. The mean SDAS result also proves that the proposed method could give better result.

DCS of the dendrite was also measured with proposed method in this chapter. The conventional method cannot measure the DCS. Therefore, only the results of proposed method and manual method were compared. It showed that the proposed method produced accurate DCS result.

Dendrite morphology affects the accuracy of SDAS measurement. In this chapter, we selected 8 samples containing different types of dendrite morphology. The results showed that the proposed method could give very close result to the manual result for dendrite morphology with inter-dendritic phase either coarsened or not coarsened. However, when the dendrite arm shape is round-like, the result of the proposed method appeared unsteady accuracy. When the dendrite arm edge is not clear, the proposed method still yielded good result while the conventional intercept method presented large r variation.

References

1. M. C. Flemings, *Solidification processing*, Wiley Online Library, 1974.
2. T. Kattamis and M. Flemings, *AIME MET SOC TRANS*, 1966, **236**, 1523-1532.
3. R. Spear and G. Gardner, *AFS Transactions*, 1963, **71**, 209-215.
4. C. Caceres and B. Selling, *Materials Science and Engineering: A*, 1996, **220**, 109-116.
5. M. Kalka and J. Adamiec, *Materials characterization*, 2006, **56**, 373-378.
6. A. Hadadzadeh and M. A. Wells, *Journal of Magnesium and Alloys*, 2013, **1**, 101-114.
7. P. Mu, Y. Nadot, C. Nadot-Martin, A. Chabod, I. Serrano-Munoz and C. Verdu, *International Journal of Fatigue*, 2014, **63**, 97-109.

8. M. Zeren, *Journal of Materials Processing Technology*, 2005, **169**, 292-298.

9. H. Blum, in *Biological prototypes and synthetic systems*, Springer, 1962, pp. 244-260.

10. A. Charnes, E. L. Frome and P.-L. Yu, *Journal of the American Statistical Association*, 1976, **71**, 169-171.

11. F. E. Grubbs, *The Annals of Mathematical Statistics*, 1950, 27-58.

12. P. Peng, X. Li, J. Li, Y. Su, J. Guo and H. Fu, *Scientific reports*, 2016, **6**, 27682.

Chapter 5 Conclusions

Image processing technique has been widely used in material structure analysis. However, the conventional image analysis methods find difficulties in yielding desirable structure analysis for materials. Thus, mathematical morphology algorithms have been applied in this thesis to achieve

The results achieved in this thesis are depicted as follows.

In chapter one, we reviewed the past research of material structure analysis. The merits and de-merits of applying the image processing techniques in material structure analysis has been discussed. The motivation of using mathematical morphology to improve image analysis for material structure has been explained. The objective in this thesis has also been written.

In chapter two, an image analysis method for automatic primary grain size measurement of aluminum alloys. At the first step, eutectic grains were identified with opening algorithm. Next, an image segmentation using marker-image prepared with

EDM method was implemented to separate individual primary grains. Eutectic grains were eliminated by intersect the image segmentation result with opening result. Finally, a second implementation of watershed transformation was conducted to segment small isolated primary grains dispersed in the eutectic grains. The results showed that the proposed method well reduced the over-segmentation, which was very common in the conventional method using UEP method to prepare marker-image. As a result, the proposed method presented much better coincidence with the manual result. Subsequently, influence of image quality was investigated using bad quality image. The results showed that the combining application of BTH transformation and proposed method generated the most decent result to the manual method. The application of proposed method without BTH on bad quality image still produced better result than the conventional method and the conventional method with BTH transformation. Generally, the proposed method greatly improved the measuring accuracy for primary grain size in aluminum alloys. And, the fusing operation with BTH transformation improved the robustness of the proposed method to different image quality.

In chapter three, an image analysis method for metal particle aspect ratio measurement has been proposed in this chapter. The improvement comprises of two parts. The first one is the image segmentation method for metal particles and the second one is the aspect ratio evaluating method. Conventionally image segmentation method for aspect ratio is based on watershed transformation using automatic marker-image preparation method. It either over-segmented or under-segmented the metal particles in glass matrix. Thus, we used manual method to prepare the marker-image. The results showed that the manual method produced much better result in contrast to the watershed with UEP method and the method in chapter 2. The conventional aspect ratio evaluating

method is fit ellipse method. It worked well for the straight striped metal particles, however, under-estimated those with bended strip shapes. In this chapter, a new image analysis method for aspect ratio evaluation has been proposed. Firstly, the major axis is estimated using skeletons extracted by thinning method. A further processing with proposed moving frontier method is used. Secondly, the minor axis length is estimated using the diameter of the maximum inscribed circle.

The comparison result of aspect ratio for individual metal particles shows that the proposed method produced much more accurate result than the conventional method, no matter the metal particle shape is straight strip or bended strip. The mean value for the individual metal particles in several images also proved that the proposed method produced closer result to the manual result than the conventional method.

In chapter four, we proposed an image analysis method for semi-automatic measurement of secondary dendrite arm space (SDAS) and dendritic cell size (DCS) based on mathematical morphology. Firstly, a human subjective preparation of marker-image was conducted and used in watershed transformation. The segmentation result showed that the semi-automatic segmentation well achieved individual secondary dendrite arms. Secondly, the center lines of the secondary dendrite arms were estimated with moving frontier method and least square method. As the center lines were the fit lines of the dendrite arm skeletons, the program in this chapter could help to improve the objectivity of center lines.

The comparison of individual SDAS result with conventional intercept method, proposed method and manual method shows that the proposed method yielded closer result to the manual result. The mean SDAS result also proves that the proposed method

could give better result.

DCS of the dendrite was also measured with proposed method in this chapter. The conventional method cannot measure the DCS. Therefore, only the results of proposed method and manual method were compared. It showed that the proposed method produced accurate DCS result.

Dendrite morphology affects the accuracy of SDAS measurement. In this chapter, we selected 8 samples containing different types of dendrite morphology. The results showed that the proposed method could give very close result to the manual result for dendrite morphology with inter-dendritic grains either coarsened or not coarsened. However, when the dendrite arm shape is round-like, the result of the proposed method appeared unsteady accuracy. When the dendrite arm edge is not clear, the proposed method still yielded good result while the conventional intercept method presented large r variation.

In chapter Five, conclusions of the integral thesis have been summarized.

Appendix

1. Mathematical Morphological Algorithms on Binary Image

Binary morphological operations will be performed on example binary image shown in Fig. A.1.

Fig. A.1 Original binary image.

Fig. A.2 Erosion result.

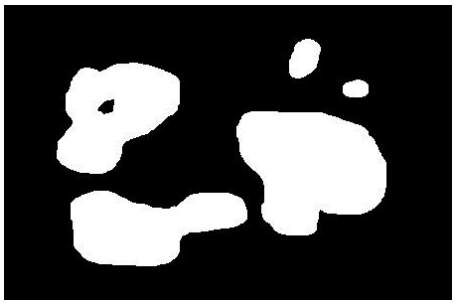

Fig. A.3 Dilation result.

1.1 Erosion

For a binary image, the erosion of a set X by a structuring element B is denoted by $\varepsilon_B(X)$ and is defined as the locus of points x such that B is included in X when its origin is placed at x. The implementation result of erosion on Fig. A1 is shown in Fig. A.2.

$$\varepsilon_B(X) = \{x \mid B_x \subseteq X\}.$$

1.2 Dilation

The dilation of a set X in binary image by a structuring element B is denoted by $\delta_B(X)$ and is defined as the locus of point x such that B hits X when its origin coincides with x. The implementation result of dilation on Fig. A1 is shown in Fig. A3.

$$\delta_B(X) = \{x \mid B_x \cap X \neq \varnothing\}.$$

1.3 Opening and Closing

The combined operation of erosion and dilation generates two more operations. Depending on the sequence of erosion and dilation, they are denoted as opening (perform dilation on the result of erosion) and closing (perform erosion on the result of dilation, respectively. As can be seen in Fig. A4, opening prunes small objects while closing fills the small holes.

$$\gamma_B(f) = \delta_B(\varepsilon_B(f)) \text{ and } \lambda_B(f) = \varepsilon_B(\delta_B(f)).$$

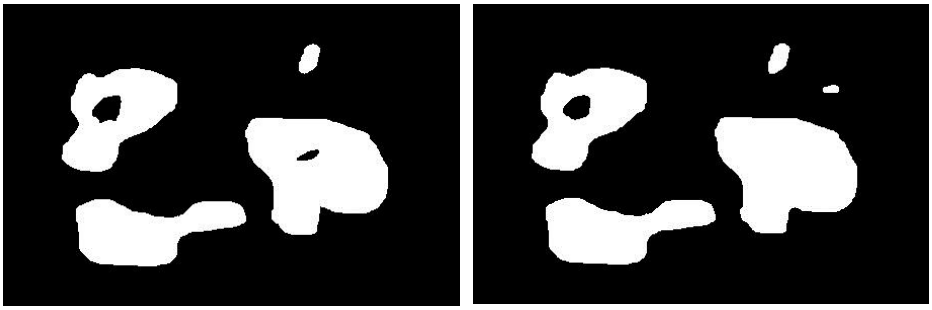

Fig. A.4. Opening and closing results. a) Opening result; and b) closing result.

1.4 Ultimate Eroding Points

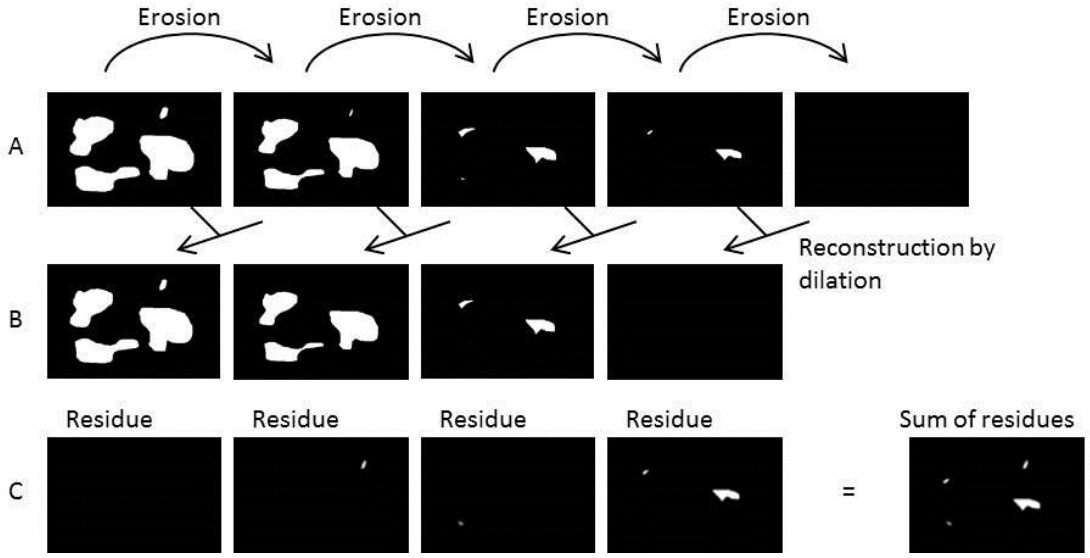

Fig. A.5 Illustration of ultimate eroding points acquisition.

Eq.1 shows the algorithm of ultimate eroding, where, $U(X)$ donates the ultimate eroding results, $\varepsilon_{\kappa_i}(X)$ is one step in the successive erosion and $\delta^{\infty}_{\kappa_i}$ indicates the reconstruction based on image $\varepsilon_{\kappa_{i+1}}(X)$ with a restriction by $\varepsilon_{\kappa_i}(X)$. Fig. A5

illustrates an example of UEP image acquisition process. In the first row A, a binary image is eroded successively by a structural element with kernel size 1 and thus we have the results A_1, A_2, etc. In the second row B, we have the successive reconstructions of A_{i+1} in A_i. B_2 is the result of A_3 in A_2. The third row C shows the results of $A_i - B_i$. Finally, the ultimate erosion is the union $\bigcup C_i$. The ultimate erosion of each component is the last step before its disappearance by successive erosions.

$$U(X) = \bigcup_{i \in \mathbb{N}} U_i(X) \quad \text{where} \quad U_i(X) = \varepsilon_{\kappa_i}(X) \setminus \delta_{\kappa_i}^{\infty}\left[\varepsilon_{\kappa_{i+1}}(X)\right]$$

1.5 Euclidean Distance Map

The calculation of Euclidean distance is as follows. Consider a set $E = \mathbb{Z}^n$ (in most of the examples, n=2), Euclidean distance between two points can be denoted as:

$$d(x,y) = \sqrt{\sum_{i=1}^{n} (y_i - x_i)^2}$$

Where, x and y indicate the related two pixels for Euclidean distance calculation.

When we mention the distance from a pixel to a pixel set, we means the distance between the pixel and the closest pixel in the set, as Eq.3 shows.

$$d(x,Y) = \min\{d(x,y) \mid y \in Y\}$$

Here, x specifies one pixel, y is a pixel in pixel set Y.

Assume set X (a strict subset of E) is the object in a binary image, $\overline{X}$ is the background. The distance map of X is the application D_x from E to $\mathbb{R}^+$ defined by:

$$\forall x \in X, D_X(x) = d\left(x, \overline{X}\right)$$

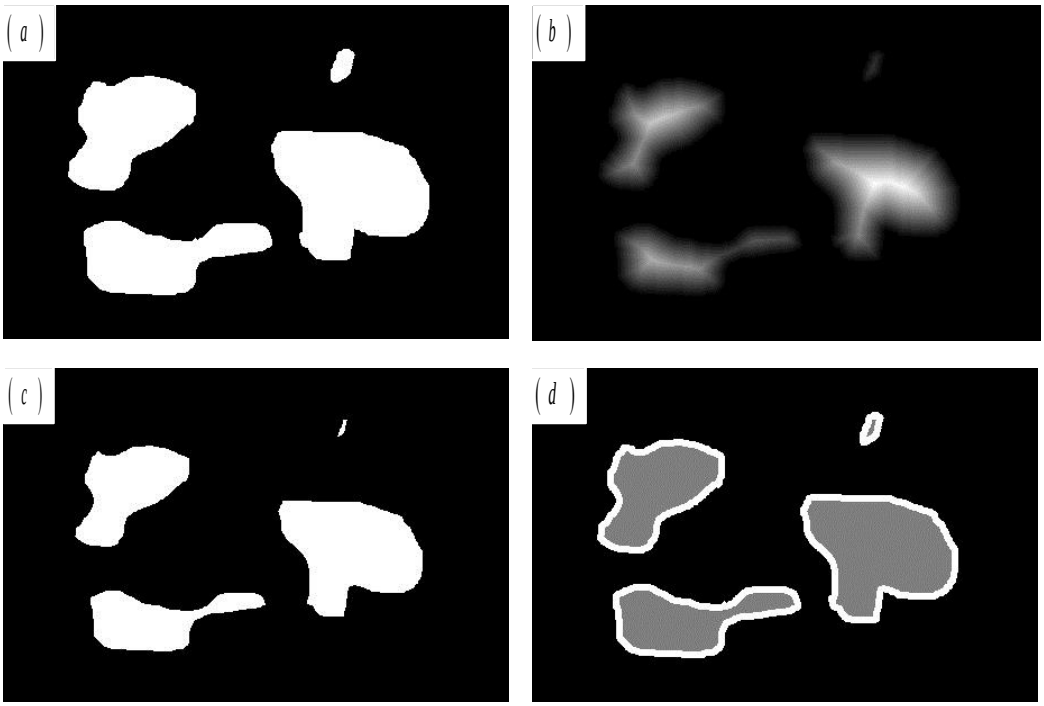

Fig. A.6. Example of Euclidean distance map and marker-preparation. a) Binary image; b) Euclidean distance map; c) binary image of b, T = 0.15; and d) marker-image, the gray areas are the objects in c.

Fig. A6 shows an example of Euclidean distance map (EDM) of a binary image. The distance had been normalized and the brightest pixel in Fig. A6 (b) has the largest distance to the background. Subsequently, the normalized EDM had been binarized with a threshold in Fig. A6 (c). In this case, it is 0.15 to preserve markers for all of the objects. The gray areas in Fig. A6 (d) indicate the markers.

2. Mathematical Morphological Algorithms on Grayscale Image

2.1 Grayscale Erosion

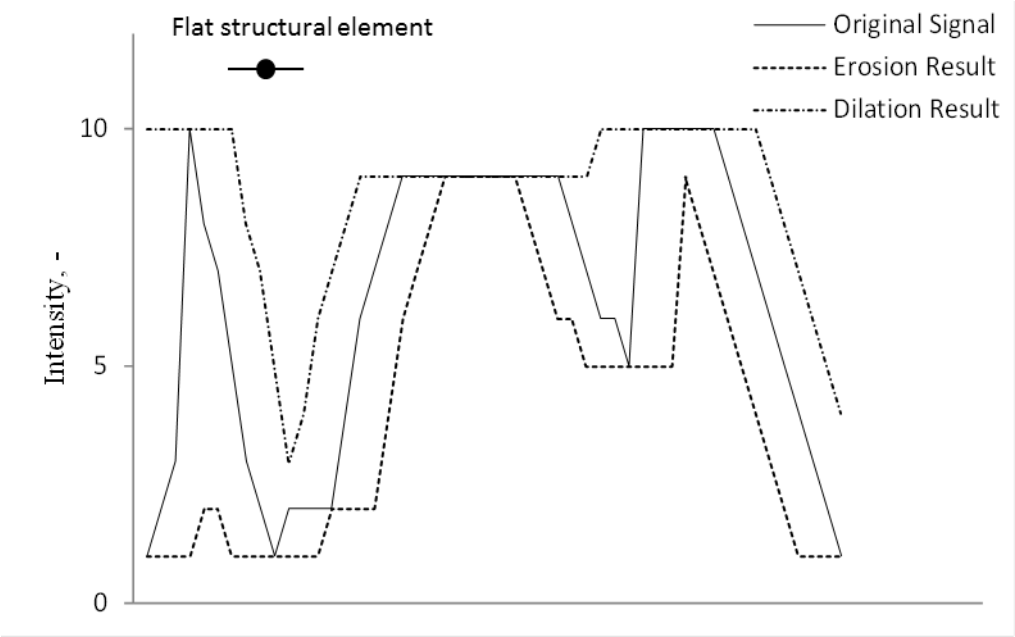

Fig. A.8. Grayscale erosion and opening on a 1 dimensional signal with a flat structural element of size 3.

Grayscale erosion with a flat disk shaped structuring element will generally darken the image. Bright regions surrounded by dark regions shrink in size, and dark regions surrounded by bright regions grow in size. As depicted in the following equation, the process of grayscale erosion is to find local infimum within the region defined by structural element. As can be seen in Fig. A7, the grayscale erosion makes the "bright" regions thinner.

$$\varepsilon_B(f) = \bigwedge_{b \in B} f_{-b} \quad .$$

2.2 Grayscale Dilation

Grayscale dilation with a flat disk shaped structuring element will brighten the image. Bright regions surrounded by dark regions grow in size and dark regions surrounded by bright regions shrink in size. As is shown in Fig. A7, the dilation result of a 1-dimensional signal with a flat structural element is the process of finding local supreme within the region defined by structural element, as is depicted in the following equation. Thus, small "dark" regions disappeared after the dilation and the signal was "brightened".

$$\delta_B(f) = \bigvee_{b \in B} f_{-b}.$$

2.3 Grayscale Opening and Closing

Similar to the opening and closing in binary image, the grayscale opening and closing operations are also the combination of grayscale erosion and grayscale dilation. As the following equation denotes, grayscale opening is the grayscale dilation on the result of grayscale erosion, while grayscale closing is inverse.

$$\gamma_B(f) = \delta_B(\varepsilon_B(f)) \text{ and } \lambda_B(f) = \varepsilon_B(\delta_B(f)).$$

2.4 Top Hat Transformation

Top hat transformation is an efficient algorithm in mathematical morphology to solve such a problem. The absolute difference between original image and grayscale opening or closing image is defined as white top hat (WTH) or black top hat (BTH) transformation, depicted in Eq.6. Here, B is the structuring element, and f indicates the original image, and $\varepsilon_B(X)$ denotes the grayscale opening and $\delta_B(X)$ specifies the

grayscale closing (See in Appendix).

$$WTH_B = f - \varepsilon_B(f)$$
$$BTH_B = \lambda_B(f) - f$$

Acknowledgement

My most sincere gratitude goes to my doctoral dissertation supervisor, Dr. Koichi Anzai, who is a dedicated explorer in material science, a kind-hearted advisor in research, a benevolent senior in life and an expert to spend an exquisite life. His earnest manner towards research will always be a prototype stimulating me to confront the potential difficulties in my future adventure in research. My gratitude also goes to Dr. Naoya Hirata, who is a young but knowledgeable explorer in material science. Despite of his decent advices and generous help, I cannot fulfil the doctoral dissertation. The pure enthusiasm towards research in material science, the compassionate concern on the research and life of students and the deep love for life will always be the radiance brightening my life and future road.

Dr. Masayuki Itamura also gave me great help during my study for the doctoral dissertation. I sincerely appreciate his decent help and wish a wonderful life after his retirement. Dr. Yoshiharu Waku gave me great help for chapter 3. He is a genius innovator in metal-ceramic composite and a kind-hearted senior in material science. I wish all the best for his family and research. Dr. Katsunari Oikawa, Dr. Akira Kawasaki and Dr. Takeshi Mihara also gave me their insightful, thoughtful and visionary advice. I appreciate it so much and give my best wishes to them. Wish everything goes well for their families and their researches.

I have to mention that my friends gave me their strong hands to help me stagger through these years. My gratitude goes to Dr. Xin Lu, Dr. Weiwei Zhou, Dr. Gaopeng Xue, Dr. Huafang Yu, Dr. Jiang Liu, Dr. Wentao Hu, Dr. Ming Li, Dr. Yiwen Zhang, Dr. Xiaopeng Feng, Dr. Xiaohao Sun, Ms. Chuchu Yang, Mr. Sihuang Zhao, Mr. Ning Xia,

Dr. Weikang Qi, Mr. Zhao Zhu, Mr. Qi Chen, Ms. Yiyi Wei, Dr. Xuantong Liu and Mr. Hanze Li. Without your dedicated and continuous encouragement and help, I could never make it. I wish the greatest expectations and happiest life for all of you. Special gratitude also goes to Ms. Miwa Otomo, who is a pretty, graceful and enthusiastic lady. I wish all the best to her happy life.

No matter what kind of difficulty I meet, there is always a gorgeous and beautiful lady standing with me, backing me and encouraging me to move forward and not to give up. I achieve power and strength from her to overcome all the difficulties and impossibilities. My deepest love goes to Ms. Peipei Liu, who is a kind, beautiful, gentle, graceful and gorgeous goddess.

Last not the least, I would like to thank my beloved father, Mr. Maoli Xu and mother, Ms. Baihua An. They are the original motivation stimulating me to stagger step by step steadily. They brought me up from a little boy and shaped me to be a man that realized what was responsibility and love. I wish God stop stealing ages from them and keep them healthy forever. I always miss you and love you, my beloved parents.